Double Integrating Sphere Characterization of PVA-Cryogels

DOUBLE INTEGRATING SPHERE CHARACTERIZATION OF PVA-CRYOGELS

By
PETER Q . FIEE

A Thesis
Submitted to the Department of Medical Physics
and the School of Graduate Studies
in Partial Fulfilment of the Requirements
for the Degree
Master of Science

McMaster University

MASTER OF SCIENCE (2013)
(Medical Physics)

McMaster University
Hamilton, Ontario

TITLE:	Double Integrating Sphere Characterization of PVA-Cryogels
AUTHOR:	Peter Q. Fiee (McMaster University)
SUPERVISOR:	Dr. Kevin R. Diamond
NUMBER OF PAGES:	vii, 82

Abstract

Proper functioning of instruments requires precise calibration and routine quality assurance. In a clinical setting, this is achieved through the use of phantoms, which mimic the physical characteristics of tissues. Polyvinyl alcohol (PVA), a non-toxic, water-soluble polymer is well-suited for use as clinical phantom material. Through successive freezing and thawing, solutions of PVA in water can be solidified into rigid *cryogels* (PVA-C). The number of freeze-thaw cycles affects the properties of the material, including its optical characteristics.

A double integrating sphere system was used in conjunction with the Inverse Adding Doubling (IAD) algorithm to characterize the optical properties of thin slab samples. The setup was evaluated using liquid phantoms. Liquid emulsion and food colouring were used to impart scattering and absorbing properties in the range characteristic of human tissue. Measured values of normalized reflectances and transmittances were entered into IAD, and a set of optical properties (μ_s', μ_a, g) retrieved. The reduced scattering coefficient was found to increase linearly with increasing lipid concentration, while a consistent overestimation of the absorption coefficient was observed.

Measurements of PVA cryogels revealed a linear increase in the reduced scattering coefficient with an increasing number of freeze-thaw cycles up to five cycles. Scattering was also observed to increase with concentration up to PVA concentrations of 15%, and to spontaneously increase during the lifetime of the slab samples. These findings suggest it is possible to tune the optical scattering of PVA-C via different purely physical mechanisms.

Acknowledgements

My sincerest gratitude goes to Dr. Kevin Diamond, without whose guidance and support this work would not have been possible. I would also like to thank Dr. Mike Patterson and Dr. Joe Hayward for their patience, as well as their invaluable insight and feedback while serving on my committee.

I am equally grateful towards Dr. Gordon Campbell, who gladly shared his standard operating procedures, manufacturing techniques, as well as numerous prefabricated gel samples. I would also like to thank our very own Juravinski Cancer Centre machine shop demigods Budd Thomas and Randy Passow for their work in crafting essential supplementary components for our instrumental setup to the highest standards. To Derek Capone, who introduced me to the inner workings, and upgraded the software of the Mark II system, thanks buddy.

Et parentibus et omnibus fautoribus amicisque mecum iter agentibus, toto corde gratias ago. Benignitate operiamini in aeternum.

Contents

List of Figures

List of Tables

Introduction

Advances in Biophotonics, wherein optical techniques are used for non-invasive studies, diagnostics and treatment, have spurred a growing demand for realistic models and materials that faithfully mimic the mechanical and optical properties of biological tissue. These materials, called phantoms, typically contain absorbing and scattering agents suspended in a medium to replicate the optical properties of tissues. It is desirable that phantoms be free of toxic material that may cause harm to people charged with their production and deployment.

The optical and mechanical properties of Polyvinyl alcohol cryogels (PVA-C), which can be manipulated to match those of human tissues, make this compound an alluring phantom candidate. PVA is a non-toxic, water soluble polymer that can be rigidified by cross-linking the polymer chains, either via high-dose irradiation or through the use of chemical cross-linking agents. The same result can also be achieved physically through successive freezing and thawing of the hydrogel, resulting in not only a stronger, rubbery cryogel, but one that is also considerably more turbid. The goal herein is to quantify the optical properties of polyvinyl alcohol cryogels for different production conditions such as the polymer concentration and number of freeze-thaw cycles. The ability of PVA-C to reproduce optical scattering characteristics typical of human tissues is guaged, and potential future deployment discussed.

For this study, a "double integrating sphere" system that measures diffusely reflected and transmitted light from a thin intervening sample was used in conjunction with the Inverse Adding-Doubling algorithm to retrieve relevant optical properties from sets of said measurements.

The next few subsections include a brief discussion of tissue-mimicking phantoms, their current uses as well as production methods. Polyvinyl alcohol, its properties along with its current biomedical uses is also discussed. Finally, optical properties and background information on the integrating sphere theory and light interactions in tissue will be expounded.

1.1 Tissue-Mimicking Phantoms

Phantoms are inanimate objects designed to mimic the physical properties of various tissues, including but not limited to proton relaxation times, radiative stopping power,

electron density, optical properties (Counter 2010; Devi et al. 2005). This discussion is limited to the latter.

First used in the 1980s for transillumination studies (Linford et al. 1986), they are now used routinely for the evaluation of new medical technologies, the optimization of signal to noise in existing systems, and the calibration of existing imaging and treatment machines. Recent advances in the applications of light in medicine – cosmetic laser surgery, near infrared tomography, photodynamic therapy dosimetry, luminescence imaging, fluorescence molecular imaging, optical coherence tomography – have further fuelled the demand for optical tissue phantoms (Counter 2010; Pogue and Patterson 2006).

Phantoms imitate tissue optical properties via the incorporation of absorption and scattering agents suspended in bulk material. Different imaging technologies require phantoms to satisfy usually dissimilar criteria. The properties of an ideal phantom, therefore depend on its intended purpose. It must, however satisfy the following (Counter 2010):

1. Absorption and scattering properties/spectra can be varied to match different tissues of interest
2. Biological molecules of interest can be incorporated (biocompatibility)
3. Phantoms are stable over time and environmental conditions
4. Index of refraction matches that of tissue
5. Ability to incorporate regions with different optical properties (tumour phantom)
6. Mechanical properties similar to tissue
7. Ease of manufacturing - low toxicity
8. Inexpensive to produce
9. Easily transported to different sites

1.1.1 Absorbing and Scattering Agents

Absorbing and scattering agents are usually added to phantoms with their quantities adjusted in such a way as to mimic various tissues. Depending on the type of phantom matrix material, an assorted mix of absorbers, biological and chemical, may be used. Erythrocytes, whole blood, and haemoglobin are typically used when the goal is to mimic real tissue. These additives, however, result in phantoms with a very short shelf life. Black ink, another popular absorber, provides a flat absorption spectrum across most of the visible and near-infrared wavelengths. Initially assumed to be a perfect black body absorber, studies (Madsen et al. 1992; Royston et al. 1996) have shown inks – essentially carbon particulates suspended in emulsion – contribute some scattering component. Care must also be taken when using inks since inter-batch variability can be high. Molecular absorber dyes, which have insignificant scattering,

have also been used to yield wavelength-specific absorption peaks (Madsen et al. 1992; Pogue and Patterson 2006).

To simulate scattering in optical phantoms, three main types of particles are usually employed: lipid emulsions, polymer microspheres, and white metal oxide, at volume fractions no greater than 5%. Lipid based scatterers are inexpensive and have the added benefit of being similar to the bilipid membranes of cells and organelles, which are thought to cause scattering in tissue (Mourant et al. 1998; Pogue and Patterson 2006). Early scatterers, which were made from milk or emulsified oil suspensions have largely been superseded by commercial grade calibrated lipid solutions. Intralipid (Kabivitrum Inc., Sweden) is the most commonly used. These solutions are readily available in hospitals, and have a high intra-batch uniformity. The solutions can typically be used for a few days, after which they spoil.

Polymer microspheres, with their well controlled size and index of refraction, make excellent phantom additives. They have been shown to exhibit scattering properties that match those predicted from Mie theory, thus providing a level of validation that does not exist in any other system. As such, these types of phantoms are best for validation of absolute optical properties. They are, however, relatively expensive.

Metal oxides, usually Titanium dioxide (TiO_2), the pigment in white paint, and Aluminium- or Barium oxide powders, used to coat the highly reflective interior of integrating spheres, are also good scatterers. TiO_2 powder is commercially available in several forms and purities. The main disadvantage of metal oxide powders is that they settle, forming a precipitate in aqueous phantoms, and must be agitated continuously to maintain phantom homogeneity. This is less of problem in solid phantoms (Counter 2010; Pogue and Patterson 2006).

1.1.2 Bulk Matrix Materials

The choice of bulk matrix material for the phantom has the largest impact on how the phantom can be used. The compatibility of various scattering and absorbing agents is largely determined by the matrix environment as seen in table 1.1.

Aqueous suspensions are compatible with any of the three main scatterers: lipid, microspheres, or TiO_2 powder in suspension. Their low absorption throughout most of the visible and near-infrared wavelengths is mainly due to water, and absorbers can be easily added to impart absorption characteristics specific to various tissues.

Hydrogel-based phantoms such as gelatine and agarose are polymers that encapsulate water and form a solid but flexible matrix. In addition to being non-toxic, both allow the inclusion of organic molecules, and have enjoyed a long period of use as optical phantoms. These phantoms, though longer-lived than their aqueous counterparts, are not permanent and will suffer desiccation or mould growth. The latter effect can be mitigated through the use of anti-microbial agents.

Resin-type phantoms are the longest lived, and as such most suited for calibration, routine validation, and intersystem comparisons. Construction requires mixing a resin

Phantom matrix material	Permanent	Solid/ liquid/ flexible	Biologically compatible	Organic chemical compatible	Inclusions possible?	Adjustable absorption	Adjustable scattering	Index of refraction	Recommended use
Aqueous suspension	N	L	Y	Y	Y	Y	Y	1.34	Initial use and multiple phantom contrast studies
Gelatin/agar matrix	N	F	Y	Y	Y	Y	Y	1.35	Detailed heterogeneity phantom studies bioabsorbers and fluorophores
Polyacrylamide gel	N	F	Y	Y	Y	Y	Y	1.35	Thermal therapy studies
Polyester or epoxy resin	Y	S	N	N	Y	Y	Y	1.54	Calibration and routine validation Intersystem comparisons
Polyurethane resin	Y	S	N	N	Y	Y	Y	1.50	Calibration and routine validation Intersystem comparisons Inclusion of dyes
RTV silicone	Y	F	N	N	Y	Y	Y	1.4	Complex geometries with permanent flexible phantoms

Table 1.1: Suspension Matrix Material(Pogue and Patterson 2006)

and a hardener to create a clear solid that will harden within hours of pouring into a mould. The mixing of resin and hardener is exothermic, accompanied by a release of gas. It is critical to degas the phantom during the initial curing process to avoid large numbers of air bubbles. Resin-type phantoms are not compatible with biological additives(Counter 2010; Pogue and Patterson 2006).

1.2 Polyvinyl Alcohol

First produced in 1924 by Herrmann and Haehnel, Polyvinyl Alcohol (PVA) is a water soluble polymer whose properties have made it greatly desirable for use in pharmaceutical and biomedical applications. PVA is commercially available in powder form with varying degrees of purity and molecular weights.

1.2.1 Structure and Properties

The monomer, vinyl alcohol, does not exist in a stable form, but rather rearranges to its tautomer, acetaldehyde. PVA is therefore produced by the polymerization of vinyl acetate to poly(vinyl acetate) (PVAc), followed by hydrolysis of PVAc to PVA (Hassan and Peppas 2000). The hydrolysis of poly(vinyl acetate) to poly(vinyl alcohol) results in products with different acetyl groups depending on production conditions, and never goes to completion resulting in a product that is a copolymer of PVA and PVAc (Hallensleben 2000; Surry et al. 2004) (See fig. 1.1). The degree of hydrolysis has an overall effect on the chemical properties, solubility, and crystallizability of the

resultant of PVA. Commercial grades of PVA are available with degrees of hydrolysis exceeding 98% (Hassan and Peppas 2000).

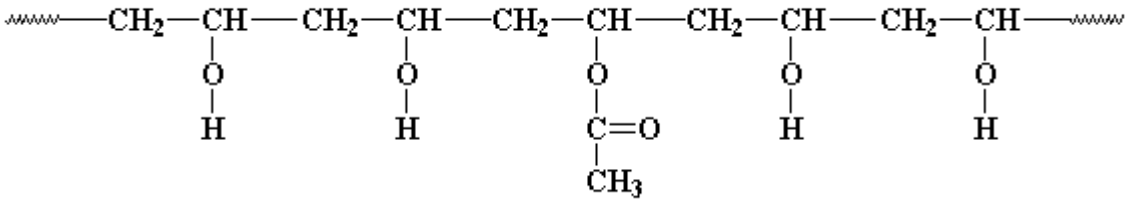

Figure 1.1: Poly(vinyl alcohol-*co*-vinyl acetate) (Counter 2010)

Aqueous solutions of PVA at room temperature have been observed to gel gradually, showing increased elasticity due to the formation of a network in which PVA crystallites act as junction points (Yokoyama et al. 1986). PVA can be rigidified further through chemical or physical crosslinking to form a gel that is stable at room temperature and retains its original shape (Stauffer and Peppas 1992). Structures such as these, which contain water but are not soluble in it, are termed hydrogels (Hyon et al. 1989). They are polymeric 3D networks that absorb large amounts of water (or biological fluids) and swell up to equilibrium. These networks, however, remain insoluble due to the presence of crosslinks (Darwis et al. 2002).

Crosslinking can be induced via the use of difunctional cross linking agents such as glutaraldehyde, acetaldehyde, formaldehyde, and many other monoaldehydes in the presence of sulphuric acid, acetic acid, or methanol, forming acetal bridges between the pendant groups of the PVA chains. The downside to using chemicals is that residual amounts linger in the gel even after extensive extraction processes, which renders the gel unfit for biomedical applications.

Another crosslinking method involves the use of electron beam or γ-radiation, in which case chemical residues are averted. The minimum gelation dose depends on the degree of polymerization and the concentration of polymer in solution. One problem with this technique is the unavoidable formation of bubbles into the gel as a result of gas formation during irradiation (Bray and Merrill 1973).

1.2.2 Physical Crosslinking

A third mechanism involves crosslinking due to crystallite formation achieved via subjecting PVA to repeated freeze-thaw cycling (-20°C and 20°C). Because of the low temperatures involved, these hydrogels are termed *cryogels*. This method is purely physical and does not involve any toxic chemical crosslinking agents or radiation. Resulting gels have higher mechanical strength than those crosslinked by chemical or irradiative techniques. Gel properties depend on the molecular weight of raw polymer, its concentration in aqueous solution, the temperature and rate of freezing, and the

number of freeze-thaw cycles it has been subjected to. The gels exhibit low toxicity, contain no impurities, and have a water content (80–90%) comparable to that of tissue. The process is thermoreversible with PVA-C having been shown to melt at 70–80°C and quickly dissolve in hot water (Stauffer and Peppas 1991, 1992).

Stauffer and Peppas (1991) discuss three models to explain the solidification of PVA-C: hydrogen bonding, polymer crystallite formation, liquid-liquid separation. Hydrogen bonding is thought to be the directional interaction that causes physical cross links (tie points) to form the gel. The polymer crystallization hypothesis attributes gelation to the organization of network chains into crystallites that are hydrogen bonded at many points along the length of the polymer chain (fig. 1.2). The liquid-liquid separation explains gelation as a phase separation into polymer rich and polymer poor regions by spinodal decomposition, i.e. the rapid unmixing of a mixture from one thermodynamic phase to form two coexisting phases. Research (Yokoyama et al. 1986) suggests that the three processes are not independent of each other, but play an interdependent role in the formation of the gel. The same study by Yokoyama used X-ray diffraction, scanning electron microscopy, optical microscopy, and tension measurements to characterize the structure of PVA-C. The structure was ultimately described as one consisting of three phases: a water phase of low PVA concentration, an amorphous phase, and a crystalline phase that restricts some of the motion of the amorphous PVA-chains.The x-ray diffraction studies showed an increase in crystallite formation with increased number of freeze-thaw cycles. Pores in the gels were also observed, with their size found to increase with the number of freeze-thaw cycles as well. This was caused by the growth of ice crystals during freezing, which upon thawing leave pores in the gel. Each freezing cycle, therefore, results in a refinement process for ice crystals. The PVA is rejected from the ice crystals as an impurity, and with each cycle, the polymer-rich and polymer-poor regions increase in purity, resulting in a increase in pore size (Stauffer and Peppas 1991).

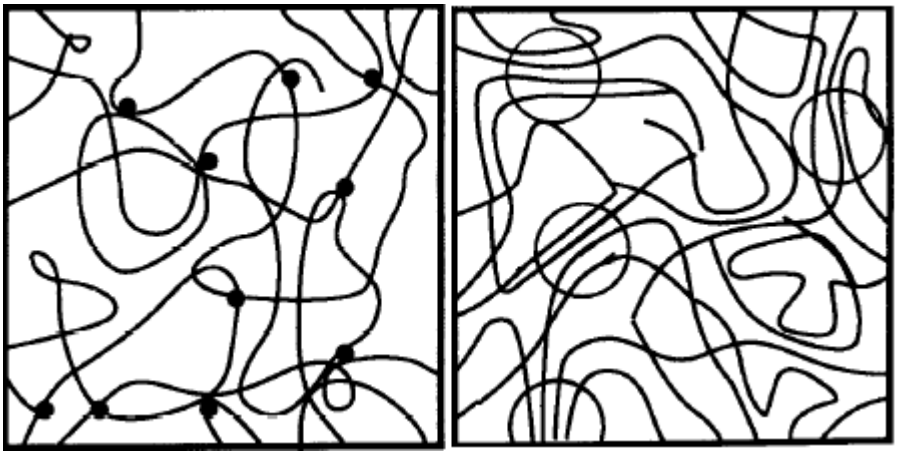

Figure 1.2: Left: PVA gel reinforcement due to hydrogen bonding. Right: PVA gel reinforcement due to microcrystallites (Stauffer and Peppas 1991)

1.2.3 Biomedical and Pharmaceutical Applications

PVA hydrogels have certain advantages that make them good biomaterials. They are non-toxic, non-carcinogenic, and have excellent bioadhesive properties. Their rubbery, elastic properties, and their ability to swell in water (or biological fluid) does well to simulate tissue. Because of these properties, they are readily accepted into the body. The gels have been used for contact lenses, the lining for artificial hearts, and drug delivery applications. They have also been shown to be biologically inert, exhibiting no long-term adverse effects – initial inflammation disappeared after two weeks – from gel samples implanted subcutaneously or intramuscularly into rabbits (Hassan and Peppas 2000). Another advantage PVA-C gel phantoms have over gels based on gelatin, agarose and polyacrylamide is their superior mechanical properties. PVA-C are rubbery with a high modulus of elasticity, while conventional gels tend to be fragile and rupture during handling, especially for larger-sized phantoms (Kharine et al. 2003).

Recent studies (Surry et al. 2004) have shown PVA-C to be a useful phantom material with well described Ultrasound and Magnetic Resonance characteristics. The gels were able to reproduce MRI relaxation times for human tissue. Depending on preparation, the velocity of sound in PVA-C was found to be well within the typical range for tissue.

1.2.4 Optical Properties of PVA

Research into the optical behaviour of PVA-C is still in its infancy. Attempts to characterize the nature of crystallites led to studies into transmission properties of PVA-C. Early turbidimetric studies using transmission measurements showed that the

particles that make up the gel behave as small spheres that increase in size with each freeze-thaw cycle. The amount of light transmitted was a function of freezing time, PVA concentration and thawing time, with scattering intensity increasing gradually for rapidly cooled samples, mainly due to the formation of new scattering sites and changes in the refractive index (Stauffer and Peppas 1991, 1992).

In a seminal study (Hyon et al. 1989), transparent gels were prepared by dissolving PVA in a mixed solvent consisting of water and dimethyl sulfoxide (DMSO) at 20/80 weight ratios. The solution was then held at -20°C for 10 hours to form a solid gel. Subsequently the DMSO was exchanged in the gel to give hydrated gels of higher tensile strength, water content, and light transmittance than the gels prepared from aqueous PVA solution. Scanning Electron Microscopy measurements (fig 1.3) showed aqueous gels to have many irregular pores with sizes larger than $3\mu m$. On the other hand, the surface of the transparent gels prepared from the water/DMSO mixture showed very small regular pores with sizes below $1\mu m$, distributed densely and homogeneously. This fine pore distribution accounts for their high transparency. DMSO was deemed to depress the freezing point of the solution, allowing PVA crystallization to proceed without phase separation, thus resulting in smaller pores. This work prompted later investigations into PVA as a material for soft contact lenses (Kita et al. 1990).

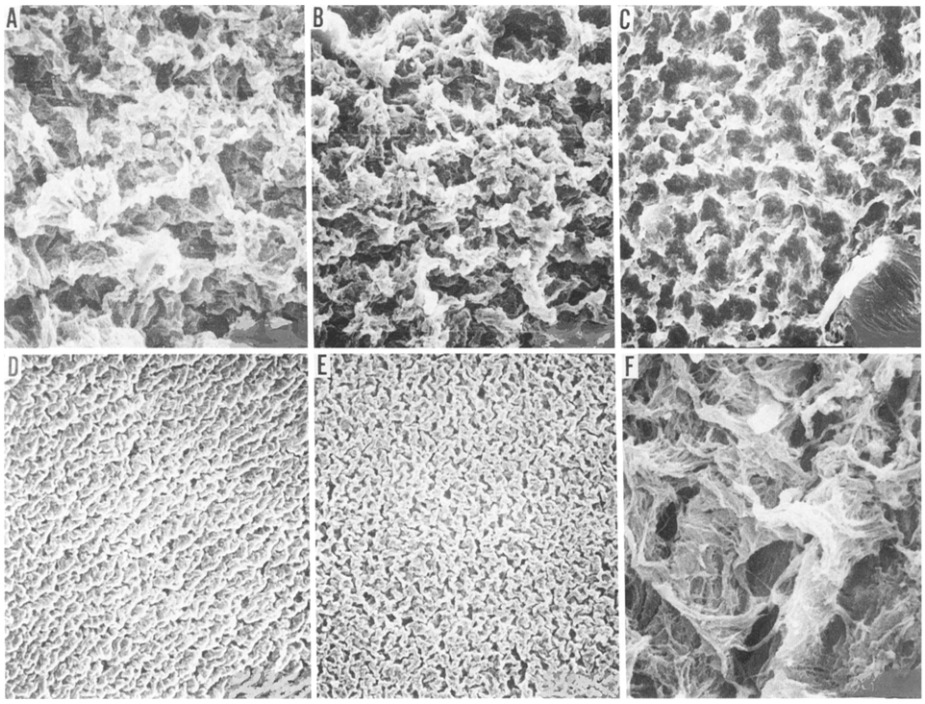

Figure 1.3: Scanning electron micrographs of PVA hydrogels obtained from water and DMSO-mixed solutions of PVA. The ratios of water:DMSO are **A** 100:0; **B** 80:20; **C** 60:40; **D** 40:60; **E** 80:20; **F** 0:100. (Kita et al. 1990)

More recently, a PVA-C breast phantom was created for photoacoustic mammogra-

phy studies (Kharine et al. 2003). The authors subjected a 20% w/w PVA formulation – cycled at -20°C for 12 hours and allowed to thaw at room temperature for another 12 hours – to a series of collimated transmission, goniometric, and refractometer tests. The scattering coefficient was found to increase with the number of freeze-thaw cycles to yield for six to seven cycles, a value that approximated that expected of breast tissue. Beyond seven cycles changes in the scattering coefficient were only slight, and the authors deemed any subsequent cycling non-justifiable. Goniometric tests yielded a scattering anisotropy coefficient of 0.91 ± 0.1 at 633nm, while the index of refraction was measured at 1.360 ± 0.002 at 589nm for the seven cycle sample.

The same group also employed Hyon's techniques to produce clear gels that could subsequently be doped with scattering agents such as polymer microspheres. The main advantage to this method is the high degree of control over the scattering properties. On the other hand, the high cost of polymer microspheres makes this approach prohibitive for large phantoms mimicking whole organs such as the *mamma*.

In another study (Devi et al. 2005), gel phantoms whose mechanical, optical and acoustic properties matched those of human breast tissue were prepared by adjusting the number of freeze-thaw cycles and the degree of hydrolysis of the starting PVA stock. The scattering anisotropy (g) was found by fitting experimentally obtained goniometric measurements to the Heyney-Greenstein phase function, which is valid in the limit of single scattering. Angular resolved transmission measurements were fitted with Monte Carlo predictions to determine reduced scattering and index of refraction. Results are summarized in table 1.2.

Number of Freeze-thaw cycles	Scattering coefficient ($\mu_s mm^{-1}$)	Anisotropy Fractor (g) $\sigma = \pm 0.0050$	Reduced Scattering Coefficient ($\mu_s mm^{-1}$)	Refractive Index (n) $\sigma = \pm 0.001$
2	2.53 ± 0.013	0.9000	0.253 ± 0.014	1.36
3	3.66 ± 0.101	0.9000	0.366 ± 0.029	1.36
4	4.89 ± 0.111	0.9000	0.488 ± 0.036	1.36
5	5.08 ± 0.131	0.9100	0.457 ± 0.038	1.36
6	6.00 ± 0.087	0.9259	0.445 ± 0.037	1.36

Table 1.2: Optical properties of phantoms fabricated using 99+% hydrolysis PVA stock for different freeze-thaw cycles (Devi et al. 2005)

Devi's group also investigated the effect of hydrolysis (table 1.3) on the optical properties of PVA-C, thus demonstrating for the first time the claim that PVA-C properties also depended strongly on the degree of raw polymer hydrolysis.

On average, it took the samples 98%-hydrolyzed twice the number of freeze-thaw cycles to match the optical properties of the higher hydrolyzed stock.

Number of Freeze-thaw cycles	Scattering coefficient ($\mu_s mm^{-1}$)	Anisotropy Fractor (g) $\sigma = \pm 0.0050$	Reduced Scattering Coefficient ($\mu_s mm^{-1}$)	Refractive Index (n) $\sigma = \pm 0.001$
2	1.441 ± 0.120	0.8900	0.159 ± 0.018	1.34
3	2.457 ± 0.054	0.8900	0.280 ± 0.023	1.34
4	2.533 ± 0.012	0.8900	0.279 ± 0.009	1.34
5	2.778 ± 0.115	0.8900	0.306 ± 0.005	1.34
6	3.670 ± 0.079	0.8900	0.404 ± 0.020	1.34
7	4.500 ± 0.076	0.8900	0.495 ± 0.022	1.34

Table 1.3: Optical properties of phantoms fabricated using 98% hydrolysis PVA stock for different freeze-thaw cycles (Devi et al. 2005)

1.3 Light Interaction with Tissue

Interaction of light with any material is dependent upon the properties of the incident light and the optical properties of the material. For tissues, these optical properties are usually described in terms of the absorption coefficient μ_a, the scattering coefficient μ_s, the scattering phase function $p(\theta)$, and the refractive index of the tissue (Jacques 2013; Welch and Van Gemert 2011).

1.3.1 Refractive Index

Biological tissues are optically inhomogenous media whose average refractive index is higher than that of air, thus accounting for the partial reflection of radiation at the tissue/air interface (Tuchin 1997). Reflection and transmission probabilities at this interface are functions of the refractive indices of the media and the angle of incidence (θ_i):

$$R_s(\theta_i) = \left[\frac{n_1 \cos\theta_i - n_2\sqrt{1 - \left(\frac{n_1}{n_2}\sin\theta_i\right)^2}}{n_1 \cos\theta_i + n_2\sqrt{1 - \left(\frac{n_1}{n_2}\sin\theta_i\right)^2}}\right]^2 \tag{1.3.1}$$

$$R_p(\theta_i) = \left[\frac{n_1\sqrt{1 - \left(\frac{n_1}{n_2}\sin\theta_i\right)^2} - n_2 \cos\theta_i}{n_1\sqrt{1 - \left(\frac{n_1}{n_2}\sin\theta_i\right)^2} + n_2 \cos\theta_i}\right]^2 \tag{1.3.2}$$

Equations 1.3.1 and 1.3.2 are the Fresnels equations for the reflection of s- and p-polarized light. If the incident light is unpolarized, the reflection coefficient is:

$$R(\theta_i) = \frac{(R_s(\theta_i) + R_p(\theta_i))}{2} \tag{1.3.3}$$

As light passes from one index of refraction to another, the direction of propagation changes. This process is termed refraction. The relationship between the angle of incidence (θ_i) and the angle of transmission (θ_t) is governed by Snell's Law:

$$n_1 \sin \theta_i = n_2 \sin \theta_t \tag{1.3.4}$$

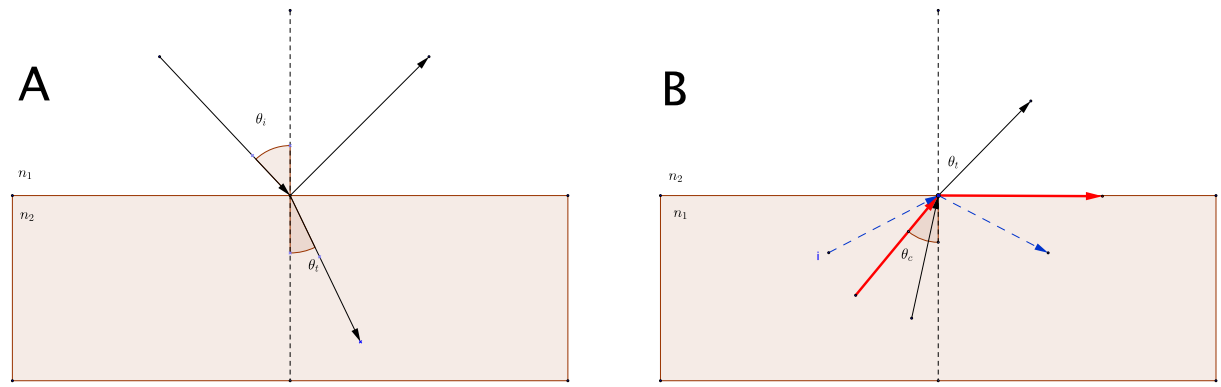

Figure 1.4: Light incident on an interface between two media of differing index of refraction: **A** Lower to higher n, and **B** Higher to lower n

Incident light from a medium of low refractive index (e.g. air) to one of higher refractive index (e.g. tissue) bends towards the normal (figure 1.4a). If light is propagating from a medium of higher refractive index to one of lower refractive index (figure 1.4b), for angles shallower than the critical angle θ_c, then all of the light reflects back into the medium of higher refractive index. This issue is important to remember when collecting light from a tissue, as light cannot pass out of the tissue into the air and then to a detector if it strikes the tissue-air interface at an angle shallower than the critical angle (Welch and Van Gemert 2011).

Due to its heterogenous composition, the index of refraction within tissue is not a constant - the index of refraction in the cell membrane is different from that in the extracellular fluid. Thus, the reported refractive index is usually a volume-weighted average of the constituents. Since water is the main constituent in body fluids and soft tissues, its index ($n = 1.33$) is the minimum value observed in biological samples. For whole tissues, the refractive index falls within the range 1.36 to 1.40. Melanin particles, found in human skin, are at the high end of the refractive index scale with $n = 1.6$ (ibid.).

1.3.2 Absorption and Scatttering

Light that penetrates the air-tissue interface is either absorbed or scattered. In the former, the absorbing molecule transitions from its ground state to an excited state.

It can then decay back to the ground state by emitting a photon of different energy as in the case of fluorescence or via radiationless decay, in which the absorbed energy is converted into heat through inter-molecular vibrations or rotations (Welch and Van Gemert 2011; Zee 1992). In purely absorbing homogenous media, the loss of intensity due to absorption is given by the Beer Lambert law:

$$I = I_0 e^{-\mu_a x} \tag{1.3.5}$$

where μ_a, the absorption coefficient, is the probability per unit path length that a photon will be absorbed. The inverse of the absorption coefficient is the *absorption length*, the distance light travels before being attenuated by a factor of 1/e. The absorption coefficient depends on tissue chromophore composition, concentration c_i, which will vary with position (r) and time t:

$$\mu_a(\lambda, r, t) = \sum_i \rho_i(\lambda) c_i(r, t) \tag{1.3.6}$$

where ρ_i is the absorption cross section of each chromophore. Major chromophores in tissue include water, haemoglobin, lipids, and melanin (Glennie 2009; Zee 1992).

Scattering is the process in which light interacting with a material changes direction. It is termed elastic if the scattered light has the same wavelength as the incident light. Optical scattering in tissue is due to cells and organelles, which act as particles with different refractive indices from that of the surrounding medium. The percentage of scattered light and its angular distribution also depends upon the ratio of the particle size to wavelength (Firbank 1994; Jacques 2013), and the ability of a particle to scatter light is expressed in terms of an effective surface area called the *total scattering cross-section,* σ_s. The scattering coefficient, μ_s, for a mixture of particles of different concentration ρ_i and scattering cross-sections σ_{si} is given by

$$\mu_s = \sum_i \rho_i \sigma_{si} \tag{1.3.7}$$

and is defined as the probability per unit path length that a photon will undergo scattering. The sum of the absorption and scattering coefficients is the total attenuation coefficient μ_t. The inverse of the latter term is called the mean free path, the distance light travels before being attenuated by a factor of 1/e.

The product of the total attenuation coefficient and a sample's physical thickness, d, is known as the optical depth

$$\tau = \mu_t d. \tag{1.3.8}$$

This dimensionless quantity expresses the number of interactions a photon will undergo before being absorbed or transmitted. The transmission of a collimated bream through a tissue with a thickness of one optical depth is 37%, ergo, light incident on a sample with $\tau = 3$ will undergo on average three interactions before being transmitted (Welch and Van Gemert 2011).

The single scatter albedo is the ratio of the scattering coefficient to the total attenuation coefficient

$$\alpha = \frac{\mu_s}{\mu_t} \tag{1.3.9}$$

1.3.3 Scattering Phase Function

The phase function $p(\hat{\mathbf{s}}, \hat{\mathbf{s}}')$ describes the angular distribution for a single scatter event for light traveling from direction $\hat{\mathbf{s}}'$ to $\hat{\mathbf{s}}$. For tractability the scattering phase function is often assumed to be a function of only the angle θ between the two direction vectors, thus $p(\hat{\mathbf{s}}, \hat{\mathbf{s}}') = p(\hat{\mathbf{s}} \cdot \hat{\mathbf{s}}') = p(cos\theta) = p(\nu)$. The function $p(\hat{\mathbf{s}}, \hat{\mathbf{s}}')$ is usually treated as a probability distribution, and normalized so that the integral over all directions is unity:

$$g = \int_{4\pi} p(\hat{\mathbf{s}}, \hat{\mathbf{s}}') d\omega = 1 \tag{1.3.10}$$

where $d\omega$ is the differential solid angle in the direction $\hat{\mathbf{s}}$. The simplest phase function is the isotropic phase function

$$p(\hat{\mathbf{s}} \cdot \hat{\mathbf{s}}') = \frac{1}{4\pi} \tag{1.3.11}$$

If the phase function is not isotropic, the average cosine of the phase function, g, is used to describe the anisotropy. Mathematically, g is defined as the expectation value of the cosine of the scattering angle θ

$$g = \frac{\int_{4\pi} p(\hat{\mathbf{s}}, \hat{\mathbf{s}}')(\hat{\mathbf{s}} \cdot \hat{\mathbf{s}}') d\omega}{\int_{4\pi} p(\hat{\mathbf{s}}, \hat{\mathbf{s}}') d\omega} = \int_{4\pi} p(\hat{\mathbf{s}} \cdot \hat{\mathbf{s}}')(\hat{\mathbf{s}} \cdot \hat{\mathbf{s}}') d\omega \tag{1.3.12}$$

This parameter is a measure of how much light is scattered in the forward direction. $g = 1$ when all light is forward scattered, while isotropic scattering results when $g = 0$. A negative anisotropy coefficient indicates that backscatter is favoured. For many tissues $g \approx 0.6 - 0.9$, and can be as large as 0.995 for blood (Tuchin 1997).

The choice of a single scattering phase function is a compromise between realism and mathematical tractability(Prahl 1988). The most used scattering phase function is the Henyey-Greenstein phase function

$$P_{HG}(\nu) = \frac{1}{4\pi} \frac{1 - g^2}{(1 + g^2 - 2g\nu)^{3/2}} \tag{1.3.13}$$

which has been shown to provide a reasonable estimate of the forward scattering nature of tissue. Although it may not exactly represent the true phase function of biological tissue, it has been shown experimentally to be a good approximation. Because it is parameterized in terms of g, and is invertible for use in Monte Carlo simulations, it is quite practical (Counter 2010; Welch and Van Gemert 2011).

1.3.4 Reduced Scattering Coefficient

In the wavelength range 0.6 - 1.5 µm, where scattering prevails over absorption, photons are able to penetrate deeper within a medium without being absorbed (Tuchin 1997). Within this region, where scattering dominates, and is usually highly forward peaked, the measurement of the total attenuation coefficient is effectively a measurement of the scattering coefficient. It may be assumed that the fluence due to the such highly forward peaked scattering can be equated to to the fluence due to a different set of optical interactions in which the scattering is isotropic. In such cases, the reduced scattering coefficient is used (Farrell et al. 1992). The reduced scattering coefficient

$$\mu_s' = (1-g)\mu_s \tag{1.3.14}$$

can be thought of as the inverse distance between *effectively isotropic* scattering events: 100 individual, highly forward scattering events may have occurred, but are lumped together into a single, effective scattering event in which the photon loses all memory of its initial direction (Weissleder et al. 2010). The number of scattering events required to produce this isotropic distribution is given by the factor $(1-g)^{-1}$. For example, a forward scattering medium with $g = 0.99$ will undergo 100 scattering events, while a medium with $g = 0.5$ will experience only 2 scattering events to disperse light isotropically. The reduced scattering coefficient over a wavelength range may be described by the following power law:

$$\mu_s'(\lambda) = \mu_s'(\lambda_o)(\frac{\lambda}{\lambda_o})^{-b} \tag{1.3.15}$$

where λ_o is the reduced scattering coefficient at a reference wavelength, and b is related to the average scatterer size. Equation 1.3.15 shows the reduced scattering coefficient to decrease with increasing wavelength.

1.4 Integrating Sphere Theory

Integrating spheres have a long history in optical analysis (Goebel 1967; Prahl 2011). The integrating sphere is a hollow spherical cavity with its interior covered with a highly reflective, diffusing material to create a Lambertian surface that reflects incident light isotropically. Thus light entering the sphere is stripped of any angular characteristics after multiple reflections, and is distributed evenly over the inner surface of the sphere. A typical sphere usually has two or more openings (ports) for light input and detection.

1.4.1 Radiation Exchange Inside a Sphere

Because of its spherical geometry and Lambertian properties, a sphere will distribute light uniformly to every point on the sphere wall after each reflection. Consider radiation reflecting from one area of the sphere wall to another in figure 1.5

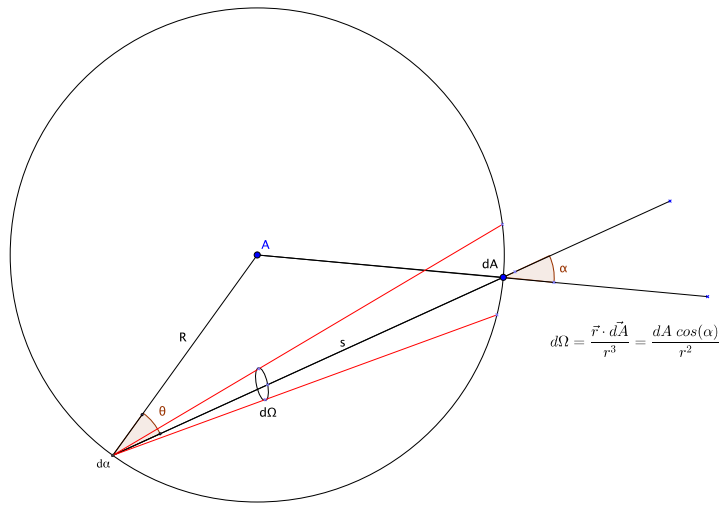

Figure 1.5: Geometric relations for calculating irradiance on dA from dα

Using the terminology applied by Goebel (1967), if J is the intensity (flux-per-unit solid angle) of the reflected flux from an element da, the resulting irradiance H on any element dA of the sphere wall is $H \equiv J \cos\alpha / s^2$, where J is the intensity in the given direction. Since $\theta = \alpha$, and $s = 2R\cos\theta$ for a sphere, $H = J\cos\theta / 4R^2 \cos^2\theta$, where R is the radius of the sphere. If the reflecting element da has a perfectly diffuse surface, $J = J_0 \cos\theta$, where J_0 is the intensity in the perpendicular direction. The irradiance on any element of the sphere wall is

$$H = J_0 \cos^2\theta / 4R^2 \cos^2\theta = J_0 / 4R^2 \tag{1.4.1}$$

Thus the irradiance is constant, and the total flux reflected by the perfectly diffusing element da is simply $P = 4\pi R^2 H = \pi J_0$. The fraction f of the total reflected flux that is incident on an area a of the sphere wall is equal to that area a divided by $4\pi R^2$, thus

$$f = a / 4\pi R^2 \tag{1.4.2}$$

The fraction of the flux received by a is the fractional surface area it consumes within the sphere.

1.4.2 Sphere Radiance Equation

The radiance (units: $\mathrm{W \cdot m^{-2} \cdot sr^{-1}}$)for a diffusely reflecting surface with input power P_i is

$$L = \frac{P_i \rho}{\pi A} \tag{1.4.3}$$

where ρ the sphere wall reflectivity, and A is the surface area of the sphere.

For an integrating sphere, the radiance equation must take into account the empty, non-reflecting areas occupied by source and detector port openings. Accounting for these, the total power incident on the sphere wall after one reflection is

$$P = P_i\rho(1-f) \tag{1.4.4}$$

where f is fraction of the sphere wall occupied by the ports. The power after the second reflection becomes

$$P = P_i\rho^2(1-f)^2 \tag{1.4.5}$$

And after n reflections:

$$P_i\rho(1-f)\{1+\rho(1-f)+...+\rho^{n-1}(1-f)^{n-1}\} \tag{1.4.6}$$

The power is

$$P = P_i\rho^n(1-f)^n \tag{1.4.7}$$

Since $\rho(1-f) < 1$, equation 1.4.7 can be reduced using an infinite power series into

$$P = P_i\frac{\rho(1-f)}{1-\rho(1-f)} \tag{1.4.8}$$

From equation 1.4.8, it is evident that the total power incident on the sphere surface is greater than the input power due to multiple reflections inside the cavity. The sphere radiance can be expressed as

$$\begin{aligned} L_s =& \frac{P_i}{\pi A(1-f)} \cdot \frac{\rho(1-f)}{1-\rho(1-f)} \\ =& \frac{P_i}{\pi A} \cdot \frac{\rho}{1-\rho(1-f)} \end{aligned} \tag{1.4.9}$$

The latter term is known as the sphere multiplier, and is intimately tied to the overall performance of the sphere. A low multiplier indicates that a large amount of light is lost via absorption or through a port opening (Glennie 2009).

1.4.3 Sphere Design

Equation 1.4.9 sheds some light on the general performance of an integrating sphere.For example, the radiance is inversely proportional to the sphere diameter as well as the port fraction (see equation 1.4.9 above). Of greater importance is the effect of the multiplier.

$$M = \frac{\rho}{1-\rho(1-f)} \tag{1.4.10}$$

As the name suggests, this term accounts for the multiple reflections within the sphere. The form presented in equation 1.4.10 applies to the specific case where the

flux is incident on the sphere wall, the reflectance is uniform, and the reflectance of all port areas is zero. Since as ρ approaches 1, M goes to infinity, it goes without saying that choosing a higher reflective coating will yield a larger multiplier. Care must be taken though, for the greater the reflectivity of the coating, the more sensitive the sphere will be to small changes in the reflectivity of its wall. The relative increase in radiance will also be greater than the relative increase in reflectance by a factor equal to the new sphere multiplier.

$$\frac{\Delta L_s}{L_s} \approx \frac{\Delta \rho}{\rho_0} \cdot M_{new} \tag{1.4.11}$$

For example, of the two diffuse reflectance coatings used by Labsphere, Spectralon® offers a 2-15% increase in reflectance over Spectraflect® . For an identical sphere design, the increase in radiance ranges from 40-240%, with the largest gains in the NIR region above 1400nm (Labsphere 1999).

Another important consequence of the multiplier is the non-linearity that the sphere will exhibit. A diffuse reflectance measurement made on a 50% reflecting sample will register more than twice the value measured for a 25% reflecting sample. The sample changes how many times light bounces inside the sphere (increasing the sphere multiplier). More reflective samples yield more bounces, and photons have a higher chance of being detected (Counter 2010).

The larger the proportion of the sphere wall occupied by ports, the greater the amount of light lost. When the port fraction exceeds 5%, one begins to lose the advantage offered by the high reflective coatings, and sphere performance degrades. A rule of thumb when choosing an integrating sphere is to have the port fraction lower than 5% (Glennie 2009; Labsphere 1999). From equation 1.4.9, it is evident that radiance decreases with increasing sphere diameter. Real integrating spheres are designed by initially considering the diameter required for the port openings. Smaller spheres may produce higher radiance, but since the integrating sphere is usually employed for its ability to spatially integrate input flux, a larger sphere diameter and smaller port fraction will improve the sphere's ability to remove angular character from light (Labsphere 1999).

For most integrating sphere applications, it is important that the detector is shielded from incident light. This is achieved by using baffles, which block incident light that has not undergone at least two reflections from the sphere surface. They are considered an extension of the sphere wall, and even though their contribution to the sphere area can be factored into the radiance equation, their fractional contribution to the sphere is small, and they usually do not alter the radiance (ibid.).

1.5 Thesis Proposal

Advances in imaging and diagnostics have given rise to a growing need for tissue simulating phantoms. Of the novel phantom materials, Polyvinyl alcohol cryogels have

been said to be the most promising due to their excellent mechanical and biomedical properties (Pogue and Patterson 2006). The mechanical properties of PVA-C have been well characterized, but comprehensive research into its optical properties is still deficient.

Recent work by Counter (2010) examined the feasibility of deploying an integrating sphere system as a mainstay for thin slab optical phantom measurements at the Juravinski Cancer Centre (JCC). Currently, optical property measurements require large volume phantoms to simulate semi-infinite geometries. These phantoms can be costly and inefficient to produce especially for phantoms with low scattering. The double integrating sphere system affords the operator the means to quantify optical properties at a smaller scale with thin, flat slabs sandwiched between two integrating spheres. The system can be combined with either custom-made Monte Carlo methods or any of the well established algorithms designed to retrieve optical properties from integrating sphere measurements. Despite limitations such as not being able to use two integrating spheres for simultaneous reflectance/transmittance measurements, and having no proper control over the freezing and thawing rates, this study showed promise for the establishment of the double integrating system as part of the research tools at the JCC.

The goals of this study are to evaluate the ability of an integrating sphere system to recover optical properties of PVA cryogels, and to examine how to fine tune PVA-C formulations to mimic the optical properties (absorption, scattering and anisotropy) of various soft tissues. Attempts will be made to produce and quantify thin slab PVA-C phantoms with scattering coefficients spanning a wide range employing only physical methods (e.g. freeze-thaw cycling) while avoiding extrinsic scatterers. The results obtained from this investigation will hopefully be beneficial to future generations of researchers looking to study the optical properties of this very promising phantom material.

Theory and Apparatus Setup

Measurement of light absorption and scattering in tissue, for the purpose of quantifying the optical properties previously introduced in Section 1.3, has given rise to numerous techniques that can broadly be classed into two: direct vs indirect. Direct measurements are those in which a particular coefficient is measured in optically thin samples in a way that does not require a model of light propagation. Indirect methods require the application of specific models of light propagation to deduce optical properties from measurements of bulk tissue properties. The optical properties are placed in a light propagation model, and values for the measured parameters fitted to the optical properties (Welch and Van Gemert 2011). Such methods may be divided into three broad categories: (i) external, in which light detectors are situated outside the tissue volume, (ii) internal, in which detectors are placed within tissue, and (iii) perturbation methods, in which external or internal measurements are made after the addition to tissue of some substance with known optical properties (Wilson et al. 1987). The *Double Integrating Sphere* setup, a photometric method from the first category, is investigated within.

2.1 Double Integrating Sphere Theory

The double integrating sphere setup (fig. 2.1) allows for the simultaneous measurement of diffuse reflectance (R_d), and transmittance (T_d), of a sample sandwiched between the sample ports of two integrating spheres.

The measurement of the total reflectance, the total transmittance and the thickness of the sample permits the determination of the absorbing and scattering properties of tissue under the assumption of some model of radiative transfer (Pickering et al. 1992). For this approach to work, a tacit assumption is made that a unique relationship exists between the measured values of reflectance and transmittance (diffuse and collimated), and the set of optical parameters (μ_a, μ_s, and g). If only R_d and T_d are measured, it is not possible to determine all three optical parameters. However, under conditions where the Similarity Principle holds, it is possible to estimate the absorption and reduced scattering coefficient: it is assumed that the reflection and transmission for a slab of tissue with optical properties μ_a, μ_s and $g \neq 0$ are the same as those for the same slab with optical properties μ_a, μ_s' and $g = 0$. This assumption only holds for

slab samples of finite thickness, and quickly breaks down as slab thickness approaches effective penetration depth (de Vries et al. 1999; Welch and Van Gemert 2011).

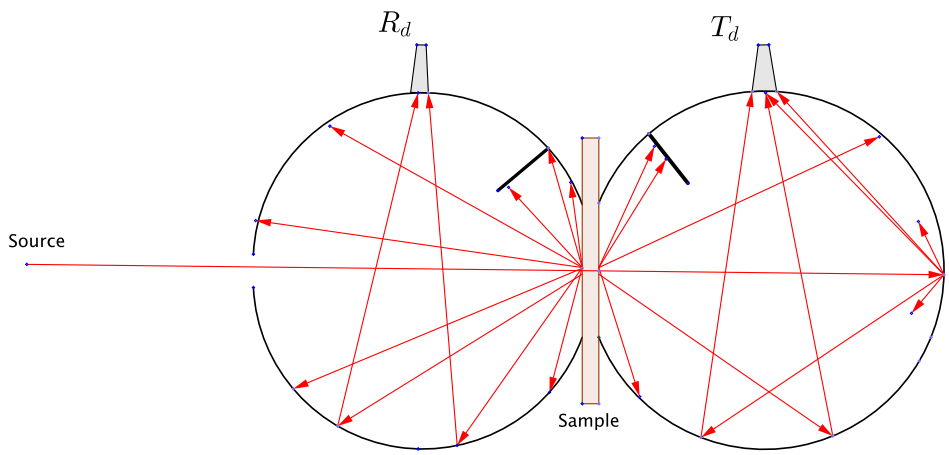

Figure 2.1: Diffuse Reflectance and Transmittance measured using a Double Integrating Sphere setup.

In the specific case depicted in figure 2.1, light that enters the reflection sphere incident on the sample gets reflected initially from the sample and transmitted through the sample to add to the signal in the transmission sphere. Furthermore, light that was initially transmitted will be re-transmitted back into the reflectance sphere, again increasing the signal. This exchange continues until all of the light is either absorbed by the sample, the sphere walls or the detector, or is lost through the gaps between the sample and the spheres, and the open ports(Counter 2010; Pickering et al. 1993). While the two spheres may be of different dimensions, it is imperative that they have identical sample ports.

This study employs a double sphere setup similar to that described by Pickering (1992), which itself was an extension of single sphere theory to two spheres and taking into account sphere crosstalk: the multiple exchange of light between the two spheres.

2.1.1 Sphere Response

Since the signal given by a detector within an integrating sphere depends on the total power incident upon said detector and on the detector's response to that power, Pickering derived a set of detector response equations. The following is a brief outline of the set of equations for the configuration in which collimated light is incident on the sample. It is assumed that the detector collects light with the same efficiency over all angles of incidence, i.e. detector output is directly proportional to the light power incident upon the detector window.

The full derivation of the response equations for single spheres is given elsewhere (Pickering et al. 1992). In brief, the sphere wall is treated as a Lambertian surface - i.e.

Nomenclature	Definition
P	Power of the light entering the sphere
P_d	Power collected by the detector
m	Reflection coefficient of the sphere wall
r	Reflection coefficient of the detector
R_d	Diffuse reflection factor of the sample with diffuse incident light
R_c	Collimated reflection factor of the sample with collimated incident light
R_{cd}	Diffuse reflection factor of the sample with collimated incident light
T_d	Diffuse transmission factor of the sample with diffuse incident light
T_c	Collimated transmission factor of the sample with collimated incident light
T_{cd}	Diffuse transmission factor of the sample with collimated incident light
R	Radius of the Sphere
$A = 4\pi R^2$	Total sphere area
δ	Area of the detector
αA	Area of the sphere wall
$\alpha = 1 - (\delta/A + s/A + h/A)$	Area of sphere wall relative to the total sphere area
s	Area of sample port
h	Area of all other ports/holes

Table 2.1: Nomenclature introduced by (Pickering et al. 1992). NB. When dealing with a second sphere, its properties are labeled with a prime (e.g. m', A')

one which reflects light with equal intensity in all diretions - therefore the power of the reflected light will be uniformly distributed over the sphere wall. For each reflection, a fraction of light is lost through the ports and absorption by the sphere wall, and the detector collects an ever-decreasing amount of light proportional to its surface area relative to the sphere area. For the first reflection, the detector collects

$$P_{d,1} = \frac{\delta}{A} m P_1 \tag{2.1.1}$$

The total power collected by the detector is the sum from 1 to ∞ of the collected power for each reflection.

$$P_d = \frac{\delta}{A} P_1 \cdot \sum_{n=1}^{\infty} F^{n-1} \tag{2.1.2}$$

where F is the fraction of the total incident light that is diffusely reflected by all components of the sphere. Because $F < 1$,

$$P_d = \frac{\delta}{A}\frac{m}{1-F} = \frac{\delta}{A}\frac{m}{1-[m\alpha + R_d(s/A) + r(\delta/A)]}P \tag{2.1.3}$$

For a double integrating sphere setup with light incident on the sample, the same approach applies. For the reflectance sphere the total detected power becomes

$$P_d = \frac{\delta}{A}\frac{R_{cd} + mR_c + T'(T_{cd} + m'T_c)}{V(1-TT')}P \tag{2.1.4}$$

where

$$V = 1 - \left(m\alpha + R_d\frac{s}{A} + r\frac{\delta}{A}\right) \tag{2.1.5}$$

and

$$T = \frac{s}{A}\frac{T_d}{V} \tag{2.1.6}$$

The power detected in the transmittance sphere is

$$P'_d = \frac{\delta'}{A'}\frac{T_{cd} + mT_c + T(R_{cd} + mR_c)}{V'(1-TT')}P \tag{2.1.7}$$

Equations 2.1.4 and 2.1.7 can be understood by considering them as the product of three terms (Counter 2010): a source term, a sphere loss term, and an exchange term. In the double-sphere case, there are three sources of light in the reflectance sphere: (i) the collimated light that is diffusely reflected by the sample, $R_{cd}P$; (ii) the diffuse light reflected from the sphere wall, mR_cP; (iii) the light due to a proportion of the collimated light first incident upon and transmitted through the sample into the transmittance sphere, then re-transmitted into the reflectance sphere:

$$\frac{s}{A'}\frac{T_d(T_{cd} + m'T_c)}{V'}P = T'(T_{cd} + m'T_c)P \tag{2.1.8}$$

Within the reflectance sphere these three sources will undergo multiple reflections, with a portion of the light being lost through the holes, and absorbed by the sphere wall as well as the sample itself. The presence of the transmittance sphere means that some of the light incident upon and transmitted through the sample will be transmitted back into the reflectance sphere. The factor $1/(1-TT')$ accounts for the increase in the detected power that is due to this multiple exchange of light between the spheres. For radiation exchange within the transmittance sphere, similar logic applies.

2.1.2 Influence of a Baffle

To prevent the detection of light not multiply scattered and of specularly reflected light from the sample, a baffle is often placed between the sample port and the detector. The baffle is a small obstruction made of the same diffuse material as the sphere wall.

Light reflected from the sample in the direction of the detector, minus the fraction lost through absorption, will be reflected back by the baffle and into the sphere. That being the case, for the sake of simplicity the term $r\delta/A$ (see eq. 2.1.5), which accounts for the reflection of light from the detector, is dropped. This is justifiable because the the contribution to the detected power due to the light reflected off the detector is negligible compared to the light reflected by the wall or sample. Thus accounting for the influence of a baffle, equation 2.1.4 becomes

$$P_d = \frac{\delta}{A}\frac{mR_c[1 - R_d(s/A)] + R_{cd}m\alpha + T'(T_{cd} + m'T_c)m\alpha}{\{1 - [m\alpha + R_{cd}]\}(1 - TT')}P \tag{2.1.9}$$

As before, an analogous relationship exists for the transmittance sphere.

2.1.3 Influence of a non-isotropic detector

An alternative to a baffle is a non-isotropic detector, specifically a detector that sees only a small area on the opposite sphere wall.

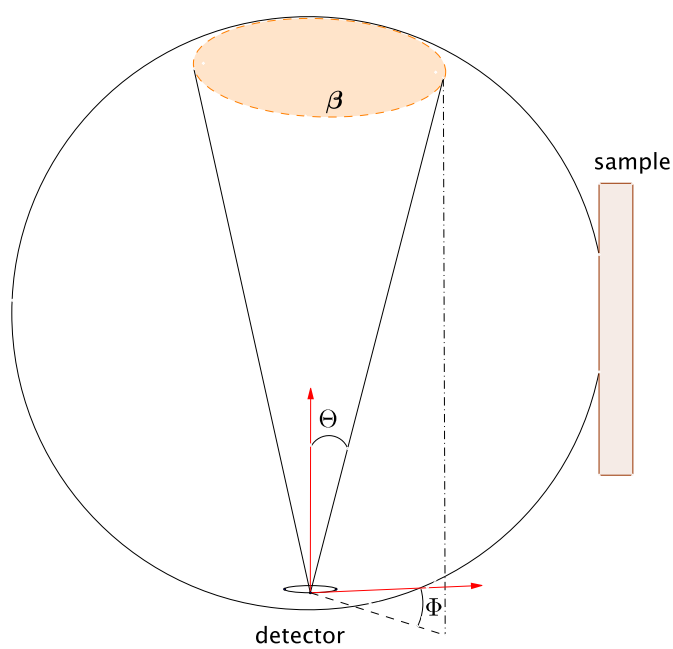

Figure 2.2: Nonisotropic detector sees only the light reflected from β. Detector efficiency may vary as to the direction(θ, ϕ) of the incoming light from β

The detector shown in Figure 2.2 collects light from surface β with angular efficiency $E(\theta, \phi)$. The fraction of light collected is given by

$$f = \beta \int_{\pi/2}\int_{2\pi} E(\theta, \phi)\sin\theta d\theta d\phi \tag{2.1.10}$$

The overall effect of using a non-isotropic detector is that detected power ratios (P_d/P) must be scaled by a linear factor $fm\alpha$, which can be obtained using single sphere theory and single sphere measurements of known reflectance standards (Counter 2010).

The equations for the power measured with the double integrating spheres are required for the simultaneous measurement of the reflection and transmission properties of a sample. With these properties a suitable model of radiative transfer within the sample may be applied to deduce the absorption and scattering characteristics of the sample (Pickering et al. 1992)

2.2 Modelling Light Transport in Tissue

There are various of approaches to modelling light propagation in absorbing and scattering media, each with merits and flaws. In assessing a particular method's merits, the following should be taken into consideration (Zee 1992):

1. Tissue is a highly scattering medium. A model should adequately deal with the effects of multiple scattering
2. For most tissues over the wavelength range (500-1000nm), the scattering coefficient is generally greater than the absorption coefficient
3. Scattering of light in biological tissue is highly anisotropic and forward-peaked
4. On a macroscopic scale, tissues are not homogenous. A model should be able to take into account multiple layers or sections within the tissue, each with different absorption and scattering coefficients
5. A model must be able to deal with complex geometries typical of in-vivo measurements
6. Computation time required to achieve results should not be excessive

While it is possible to describe light transport in a regime where multiple scattering dominates using Maxwell's electromagnetic theory, the resulting solutions are highly complex and mostly impractical (Hollis 2002). To circumvent these shortcomings, Radiative Transport - a heuristic approached that ignores the wave nature of light and considers the transport of individual photons as they are absorbed or scattered - is usually preferred. The time-independent radiative transport equation is

$$\boldsymbol{s} \cdot \boldsymbol{\nabla} \boldsymbol{L}(\boldsymbol{r}, \boldsymbol{s}) = -(\mu_a + \mu_s)\boldsymbol{L}(\boldsymbol{r}, \boldsymbol{s}) + \mu_s \int_{4\pi} p(\boldsymbol{s}, \boldsymbol{s}')\boldsymbol{L}(\boldsymbol{r}, \boldsymbol{s}')d\omega' \tag{2.2.1}$$

Equation 2.2.1 relates the gradient of the radiance $\boldsymbol{L}$ at position $\boldsymbol{r}$ in direction $\boldsymbol{s}$ to losses owing to absorption and scattering, and to gains owing to light scattered

from all other directions $\boldsymbol{s'}$ into direction $\boldsymbol{s}$. Other parameters include μ_a and μ_s, the absorption and scattering coefficients, and p, the scattering phase function, discussed in 1.3. Although polarization can be included in transport theory, it is usually neglected to not only simplify the mathematics, but also because after multiple scatterings any initial polarization information is lost (Welch and Van Gemert 2011; Zee 1992).

Since no closed-form solutions to the radiative transfer equation for tissues exist currently, it is necessary to resort to various approximations and/or numerical solutions (Zee 1992). One such approach, and of particular interest to this study, is the Adding-Doubling method.

2.3 Adding Doubling

The adding-doubling method is a numerical solution of the radiative transport equation (Prahl et al. 1993). The "doubling" method was originally developed by van de Hulst to describe the reflecting and transmitting properties of slab geometries. The method assumes knowledge of the reflection and transmission properties for a single thin homogenous layer. The reflection and transmission of a slab twice as thick are found by juxtaposing two identical slabs and summing the contributions from each slab. For an arbitrarily thick slab, reflection and transmission are repeatedly doubled until the desired thickness is reached. The "adding" method extends the doubling method to dissimilar slabs, thereby allowing the simulation of media with different layers and/or internal reflection at boundaries (Prahl 1995). To make calculations tractable, the following assumptions are made:

- The distribution of light is independent of time
- The sample has homogenous optical properties
- The sample geometry is made of layers of finite thickness extending infinitely in the direction parallel to the surface
- The surface is illuminated uniformly by a collimated or diffuse source
- Reflection at boundaries is governed by Fresnel's laws
- Radiance is azimuthally independent, its behaviour governed only by the angle it makes with the normal
- There are no internal sources within the sample

These assumptions, while restricting the type and shape of the tissue sample, do not contradict known propagation behaviour of light, thus a model based on them will retain relevance to many tissue optics problems.

2.3.1 Reflection and Transmission Functions

Indirect optical property measurement techniques often make use of coefficients of diffuse reflectance R_d and transmittance T_d (Welch and Van Gemert 2011). These coefficients can be obtained by integration of reflection and transmission functions over all angles of incidence and departure. The functions can be thought of as operators

that take incident light intensity $I_{in}(\theta)$ and transform it into reflected and transmitted intensities $I_r(\theta)$ and $I_t(\theta)$ respectively. The goal then is to obtain reflection and transmission functions for slabs of varying albedo, anisotropy and optical depth. Adding-doubling is particularly suited for slab geometry, and has advantages over other methods in that only integrations of angle are required, there is no discrimination for isotropic and anisotropic scattering samples, with results obtained for all angles of incidence. On the downside, difficulties emerge when calculating internal fluences (though in practice these are often not needed). The method is further restricted to layered geometries with uniform irradiation. It is also necessary that each layer has homogenous optical properties (Prahl 1995).

Following the notation of van de Hulst, the reflection function $R(\nu', \nu)$ is defined as the radiance reflected by the slab in the direction ν for a cone of light incident from the direction ν' (figure 2.3). Here $\nu = cos\theta$, the cosine of the angle of incidence with respect to the normal. $R(\nu', \nu)$ is normalized to an incident flux such that it has finite non-zero values when $\nu = 0$ or $\nu' = 0$. $R(\nu', \nu)$ is also the ratio of the reflection function for the sample to the reflection function of an ideal white Lambertian surface. The transmission function $T(\nu', \nu)$ is defined similarly.

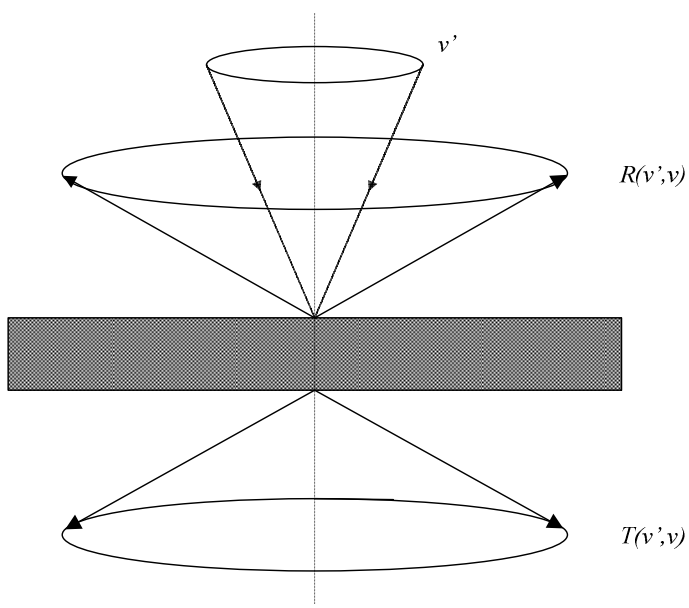

Figure 2.3: Light incident on a slab at an angle ν' is reflected and transmitted at an angle ν. (Counter 2010)

With reflection function $R(\nu', \nu)$ known, the reflected intensity distribution $I_{ref}(\nu)$ is found by integrating the incident intensity function $I_{in}(\nu')$ over all incoming directions $(0 \leq \nu' \leq 1)$

$$I_{ref}(\nu) = \int_0^1 I_{in}(\nu') R(\nu', \nu) 2\nu' d\nu' \tag{2.3.1}$$

where $I_{ref}(\nu)$ and $I_{in}(\nu')$ have units of power per unit solid angle. The transmission intensity distribution is also found likewise with knowledge of the transmission function $T(\nu', \nu)$.

As mentioned earlier, to obtain the reflection and transmission coefficients of an arbitrarily thick sample, the reflection and transmission functions are integrated over the entire range of angles of incidence and angles of departure. Thus, the total reflection coefficient for collimated light incident normal to the surface is defined as

$$\begin{aligned} R_c &= \int_0^1 \int_0^1 R(\nu', \nu) \frac{\delta(1-\nu')}{2\nu'} 2\nu' d\nu' 2\nu d\nu \\ &= \int_0^1 R(1, \nu) 2\nu d\nu \end{aligned} \tag{2.3.2}$$

The transmission coefficient T_c is defined in a similar manner, and resolves to

$$T_c = \int_0^1 T(1, \nu) 2\nu d\nu \tag{2.3.3}$$

With light incident diffusely, the coefficients for total reflection R_d and total transmission T_d are

$$R_d = \int_0^1 \int_0^1 R(\nu', \nu) 2\nu' d\nu' 2\nu d\nu \tag{2.3.4}$$

and

$$T_d = \int_0^1 \int_0^1 T(\nu', \nu) 2\nu' d\nu' 2\nu d\nu \tag{2.3.5}$$

The above integrals can be solved numerically, provided $R(\nu', \nu)$ and $T(\nu', \nu)$ functions are known. It is therefore, imperative to find these functions for an arbitrarily thick, layered sample (ibid.).

2.3.2 Matrix Approximation and Quadrature

Quadrature refers to numerically approximating the value of a *definite* integral by evaluating the integrand over a finite set of points. Simply speaking, the integral of a continuous function $f(x)$ over the interval (a, b) with a weighting function $g(x)$ can be approximated over M quadrature points as follows

$$\int_a^b f(x) g(x) dx \approx \sum_{i=1}^{M} f(x_i) w_i \tag{2.3.6}$$

Since Adding-Doubling relies on integrating combinations of reflection and transmission functions, this numerical integration method is crucial. As an example, the total reflection for normal collimated irradiance R_c can be approximated as

$$\int_0^1 R(1,\nu)2\nu d\nu \approx \sum_{i=1}^{M} 2\nu_i w_i \mathbf{R}_{iM} \tag{2.3.7}$$

where $\mathbf{R}_{iM}$ is the matrix representation of the reflection function. This approximation when extended to two arbitrary functions becomes

$$\int_0^1 A(\nu,\nu')B(\nu',\nu'')2\nu' d\nu' \approx \sum_{j=1}^{M} \mathbf{A}_{ij} 2\nu_j w_j \mathbf{B}_{jk} \equiv \mathbf{AB} \tag{2.3.8}$$

demonstrating the relationship between integration and matrix multiplication (Prahl 1995)

For a homogenous slab with isotropic scattering (g=0), a fixed albedo (α=0.9), optical thickness (τ=1), and matched boundaries, the reflection of an infinitely wide beam of normally incident light will vary with the exit angle. The reflection curve (figure 2.4) can be approximated reasonably fast and accurately using only four quadrature points as shown. It follows that using a greater number of points will result in a better approximation of the reflection function at the expense of computation time.

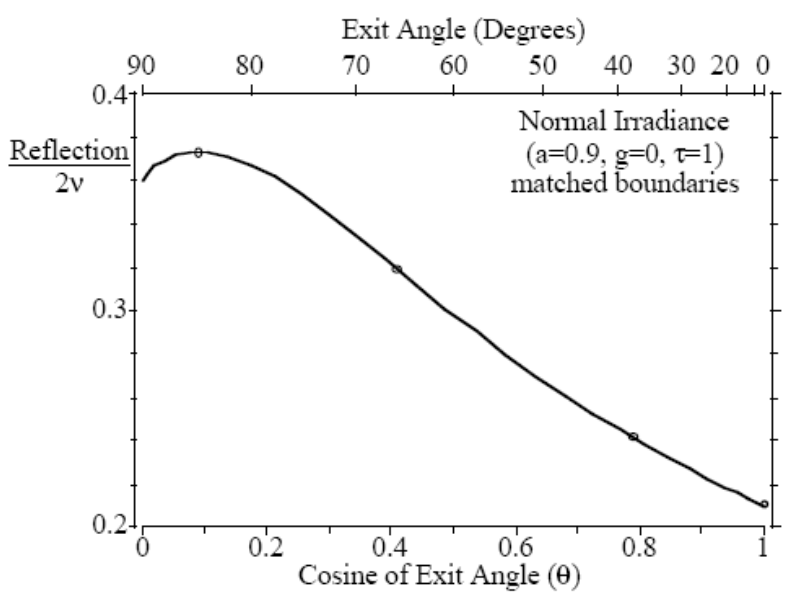

Figure 2.4: Reflection from a normally irradiated slab. The four circles represent quadrature points (Prahl 1995)

The corresponding reflection values for the four angles (85°, 66°, 33°, and 0°,) used for approximation in Figure 2.4 are

$$\begin{bmatrix} R(\nu_4,\nu_1) \\ R(\nu_4,\nu_2) \\ R(\nu_4,\nu_3) \\ R(\nu_4,\nu_4) \end{bmatrix} = \begin{bmatrix} 0.37 \\ 0.32 \\ 0.24 \\ 0.21 \end{bmatrix} \tag{2.3.9}$$

Three similar vectors for reflection exist for the other three angles of incidence ν_1, ν_2, ν_3. These can be combined into a single reflection matrix for a slab,

$$\begin{bmatrix} R(\nu_1,\nu_1) & R(\nu_2,\nu_1) & R(\nu_3,\nu_1) & R(\nu_4,\nu_1) \\ R(\nu_1,\nu_2) & R(\nu_2,\nu_2) & R(\nu_3,\nu_2) & R(\nu_4,\nu_2) \\ R(\nu_1,\nu_3) & R(\nu_2,\nu_3) & R(\nu_3,\nu_3) & R(\nu_4,\nu_3) \\ R(\nu_1,\nu_4) & R(\nu_2,\nu_4) & R(\nu_3,\nu_4) & R(\nu_4,\nu_4) \end{bmatrix} = \begin{bmatrix} 1.66 & 0.72 & 0.45 & 0.37 \\ 0.72 & 0.52 & 0.37 & 0.32 \\ 0.45 & 0.37 & 0.28 & 0.24 \\ 0.37 & 0.32 & 0.24 & 0.21 \end{bmatrix} \tag{2.3.10}$$

The result is a symmetric square matrix $R(\nu_i,\nu_j) = R(\nu_j,\nu_i)$ whose individual elements can be greater than unity because each element is divided by twice its quadrature angle.

2.3.3 Matrix Relations for Adding Layers

For the derivation of the adding-doubling equations, it is necessary to consider light entering and leaving a slab as shown in figure 2.5. The slab is infinite in the xy-plane, and bound at $\mathbf{0}$ and $\mathbf{1}$ in the z-plane. The four vectors shown describe the azimuthally independent radiance at the boundaries. The vector $\mathbf{L_0^+}$ represents the radiance incident on $\mathbf{0}$ in the downward(+)direction, and $\mathbf{L_1^-}$ is the radiance incident on $\mathbf{1}$ in the upward(-)direction. Similarly, $\mathbf{L_0^-}$ and $\mathbf{L_1^+}$ denote the radiance exiting the slab from $\mathbf{0}$ and $\mathbf{1}$ respectively.

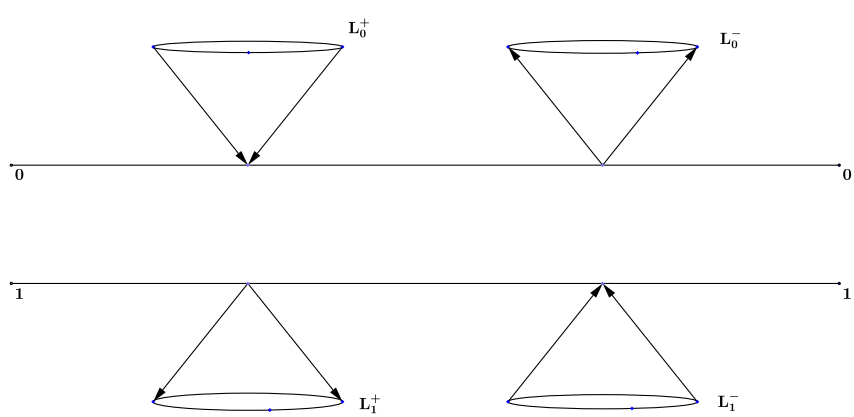

Figure 2.5: Radiance entering and exiting a slab bound by $\mathbf{0}$ and $\mathbf{1}$. The minus sign indicates light travelling upwards

The exit radiances $\mathbf{L_0^-}$ and $\mathbf{L_1^+}$ depend linearly on $\mathbf{L_1^-}$ and $\mathbf{L_0^+}$, and on the contribution from sources within the layer. A detailed description of these dependencies is given by Plass et al. (1973).

If $\mathbf{R}^{nm}$ and $\mathbf{T}^{nm}$ represent the reflection and transmission operators, respectively, for light incident on side n and moving towards side m of a homogenous slab, since light has no preferred direction then, $\mathbf{R}^{nm} = \mathbf{R}^{mn}$ and $\mathbf{T}^{nm} = \mathbf{T}^{mn}$.

The downward radiance at boundary **1** is the sum of the transmitted radiance incident on boundary **0** and the radiance reflected from side **1**,

$$\mathbf{L_1^+} = \mathbf{T_{01}L_0^+} + \mathbf{R_{10}L_1^-} \tag{2.3.11}$$

Similarly, the upward radiance at **0** is the transmitted radiance from **1** plus the reflected radiance at **0**,

$$\mathbf{L_0^-} = \mathbf{R_{01}L_0^+} + \mathbf{T_{10}L_1^-} \tag{2.3.12}$$

For another layer bound at **1** and **2**, an equivalent relationship applies

$$\begin{aligned} \mathbf{L_2^+} &= \mathbf{T_{12}L_1^+} + \mathbf{R_{21}L_2^-} \\ \mathbf{L_1^-} &= \mathbf{R_{12}L_1^+} + \mathbf{T_{21}L_2^-} \end{aligned} \tag{2.3.13}$$

The two layers (**01** and **12**) can be juxtaposed to form an aggregate layer bound at **02**, whose radiance vectors can be expressed as

$$\begin{aligned} \mathbf{L_2^+} &= \mathbf{T_{02}L_0^+} + \mathbf{R_{20}L_2^-} \\ \mathbf{L_0^-} &= \mathbf{R_{02}L_0^+} + \mathbf{T_{20}L_2^-} \end{aligned} \tag{2.3.14}$$

With the reflection and transmission operators for individual layers presumably known, the reflection and transmission operators for the combined layer ($\mathbf{R_{02}}$ and $\mathbf{T_{02}}$) can be found. Prahl (1995) gives an extensive walkthrough of the entire calculation, which results in the following operators

$$\mathbf{T_{02}} = \mathbf{T_{20}} = \mathbf{T_{10}}(\mathbf{E} - \mathbf{R_{12}R10})^{-\mathbf{1}}\mathbf{T_{21}} \tag{2.3.15}$$

$$\mathbf{R_{02}} = \mathbf{R_{20}} = \mathbf{R_{01}} + \mathbf{T_{10}}(\mathbf{E} - \mathbf{R_{12}R_{10}})^{-\mathbf{1}}\mathbf{R_{12}T_{01}} \tag{2.3.16}$$

where $\mathbf{E}$ is the identity matrix for matrix multiplication

$$\mathbf{E}_{i,j} = \frac{1}{2v_i w_j}\delta_{i,j} \tag{2.3.17}$$

The equations 2.3.15 and 2.3.16 define the transmission and reflection operators for a combined layer in terms of the transmission and reflection operators for individual layers. Most importantly, the reflection and transmission of an arbitrarily thick sample can be found by using these equations repeatedly (Counter 2010; Prahl 1995).

2.4 Inverse Adding Doubling

The Inverse Adding-Doubling algorithm conveniently combines Adding-Doubling and Double Integrating Sphere theory to estimate optical properties from measured reflectance and transmittance. In brief, Reflectance and Transmittance for a sample are predicted for a given albedo, optical thickness and scattering anisotropy using the forward adding-doubling method. These predictions are then compared to actual measurements, and the derived optical parameters adjusted to obtain more accurate predictions. This is repeated until the predicted and measured values match within a specified tolerance. These final optical parameters may then be used to calculate absorption and reduced scattering coefficients for the sample (Gebhart et al. 2006).

The iteration process implicitly assumes that a unique solution to the inverse problem exists, i.e. a unique combination of the albedo, optical thickness, and the scattering anisotropy is determined by a set of reflection (R_T) and transmission (T_T, T_c) measurements.

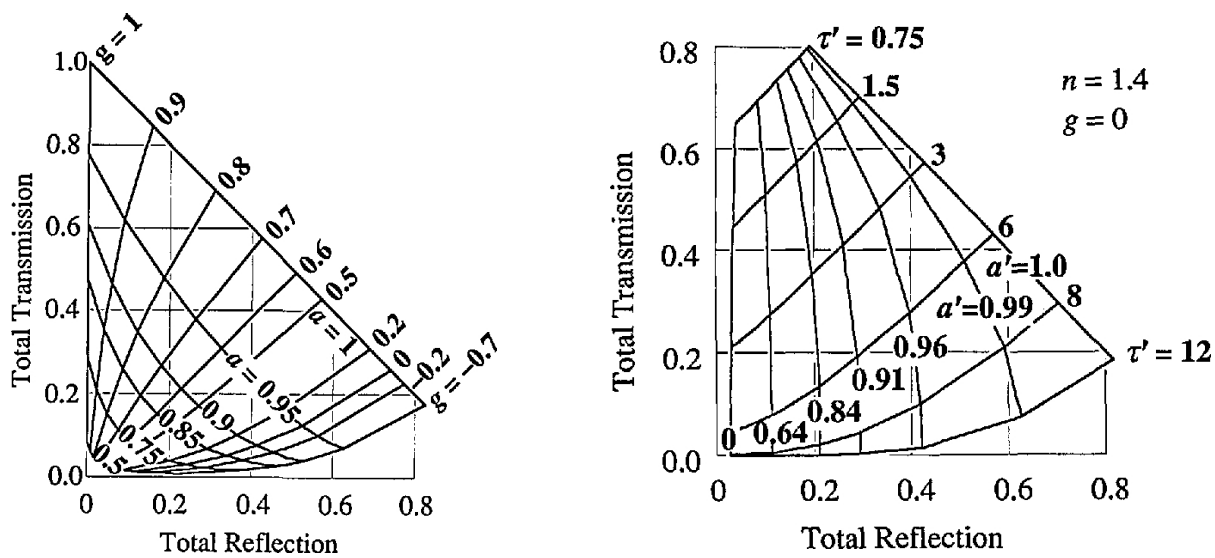

(a) Total reflection and total transmission of an index-matched slab (n= 1) as a function of the albedo α and anisotropy g for a fixed unscattered transmission value of 10%. Each point on the (α, g) grid corresponds to a unique (R_T, T_T) pair.

(b) Total reflection and total transmission of a slab as a function of the reduced albedo α' and reduced optical thickness τ'. Isotropic scattering is assumed as well as an index of refraction mismatch (n = 1.4). Each point on the (α', τ') grid corresponds to a unique (R_T, T_T) pair.

Figure 2.6: Dependence of Total Reflectance and Transmission on anisotropy and albedo (Prahl et al. 1993)

This uniqueness is demonstrated for two cases: (i) fixed unscattered transmission, in which all three measurements are known, and (ii) fixed scattering anisotropy, wherein the unscattered transmission is unknown and a fixed value for the scattering anisotropy must be assumed. Figure 2.6a shows the dependence of the total reflectance and transmission on the anisotropy and albedo. The intersection of the measured

total reflectance and transmission gridlines determines a unique albedo and anisotropy. Similarly, figure 2.6b shows the dependence of reflectance and transmission on on the reduced albedo and reduced optical thickness. Thus, a nonzero reflection and transmission measurement yields a unique value for the reduced scattering and absorption coefficient.

Given the set of three measurements (R_T, T_T, T_c), it is further assumed that the unscattered reflection from each sample surface is equal to the Fresnel reflection for the unpolarized light that is normally incident on the sample. From the unscattered transmittance, T_c, the optical thickness τ can be obtained by solving

$$T_c = \frac{(1 - r_{s1})(1 - r_{s2}) \exp(-\tau)}{1 - r_{s1} r_{s2} \exp(-2\tau)} \tag{2.4.1}$$

where r_{s1} and r_{s2} are the primary reflections for light that is normally incident on the front and back surfaces of a slab sample. In the case of a sample sandwiched between glass slides, the specular reflection coefficients typically include multiple internal reflections in the slide. Once the optical thickness is known, the albedo and scattering anisotropy are varied until calculated reflectance and transmission values match the measured values. In the case of thick samples where measurements of unscattered transmittance cannot be made, only two optical parameters can be determined. Thus, a value for the scattering anisotropy is assumed, and the albedo and optical thickness calculated based on this assumed value. If the sample is too thick for transmission measurements, the optical thickness is assumed to be infinite, and once again a fixed value for the scattering anisotropy is assumed in order to calculate the reduced albedo (Prahl et al. 1993).

The Inverse Adding Doubling algorithm has a number of distinct advantages that have cemented its widespread adoption for determining optical properties, and which make it the preferred method for this study. It is computationally fast and is accurate for various combinations of optical properties. Crucially, it is valid over practically all albedos (Gebhart et al. 2006; Zhu et al. 2007) and takes into account all of the interactions of a sample sandwiched between glass slides. In the case of a double integrating sphere setup, in which the detected signal is not linearly proportional to the sample reflection or transmission, a sample with 25% reflectance will not measure exactly one-half the value of a 50% sample. IAD incorporates methods to correct such integrating sphere effects (Prahl 2011).

Despite these advantages, some limitations exist. The biggest limitation is the way IAD handles lost light. An improper handling of the light lost through glass slides and ports in the spheres results in an overestimation of the absorption coefficient and and erroneous dependence of the obtained optical properties on the physical sample thickness (de Vries et al. 1999; Zhu et al. 2007). The latest incarnation of IAD uses a Monte Carlo routine to estimate the amount of light lost for a set of optical properties. The lost light is incorporated back into the next inverse adding-doubling estimate of the optical properties. The process is repeated until the optical properties stabilize

(Prahl 2011).

2.5 Inverse Monte Carlo

Monte Carlo simulations offer a flexible, yet rigorous approach to photon transport. The method describes local rules of photon propagation that are expressed, in the simplest case, as probability distributions that describe the step size of photon movement between sites of photon-tissue interaction, and the angles of deflection in a photon's trajectory when a scattering event occurs (Wang et al. 1995).

First developed by Metropolis and Ulam to simulate physical processes using a stochastic model, the use of the Monte Carlo method to simulate the transport of light in tissue was initially described by Adam and Wilson (Metropolis 1987; Prahl et al. 1989; Wilson and Adam 1983). The recording of photon histories as they are scattered and absorbed in a medium allows for the forward calculation of the diffuse reflectance expected when a material with a given set of optical properties is illuminated under specific conditions. Because the method is statistical in nature, calculations rely on a large number of photons to be reasonably accurate. Tracing individual photons histories within media is time consuming, as a photon may scatter multiple times before being absorbed and lost within the medium. To mitigate this problem, simulations make use of photon packets where several photons are launched en masse. As the packet moves along, an absorption interaction no longer implies the loss of an entire photon but rather an adjustment of the packet weight, indicating that some fraction of the packet has been lost to a given interaction (Moscu 2009; Wang and Jacques 1993). Another popular way of reducing computational costs while maintaining reasonable degrees of accuracy is through the use of hybrid techniques, which complement the Monte Carlo method with other techniques (Chatigny et al. 1999; Flock et al. 1988; Wang and Jacques 1993)

Since existing Monte Carlo techniques usually perform a forward calculation of reflectance and transmittance from given sets of optical properties, to obtain optical properties from experimental measurements, an inversion is made. There exist a number of Monte Carlo-based inversion algorithms. Some use look-up tables of reflectance and transmittance at different optical properties to compare with experimental data, interpolating from the resulting tables or using a polynomial fit of the data, while others may use iterative procedures. Some are even more specialized, including integrating sphere corrections or using hybrid approaches (Cruzado et al. 2013; Welch and Van Gemert 2011).

One such specialized inverse hybrid approach examined herein was developed by Yaroslavsky et al. (1996). This technique combines Monte Carlo with the small-angle approximation of the radiative transfer theory to derive optical properties of turbid media from integrating-sphere measurements. In essence, the Monte Carlo method is used to calculate the total transmittance and diffuse reflectance of a sample, while the small-angle approximation of the radiative transfer theory is used to calculate the

collimated transmittance for a given detector geometry. The technique accounts for two major sources of error in spectrophotometric measurements: (1) light lost at the edges of a sample, which often leads to an overestimation of the absorption coefficient, and (2) the contribution of multiply scattered light into the measured collimated signal, which leads to an underestimation of the optical depth.

2.5.1 Implementation

Yaroslavsky et al. (1996) have made their algorithm freely available as a Microsoft Windows executable called Magic Light. The program was used with parameters intended to mimic the setup described in section 2.6. Optical properties recovered using Magic Light were compared to those obtained using Prahl's implementation of IAD.

2.6 Apparatus

The sphere system used for this study consists of two identical integrating spheres set up in a geometry similar to that shown in figure 2.7. The light entering the sphere is relayed via fibre optic wires to a CCD detector connected to a PC.

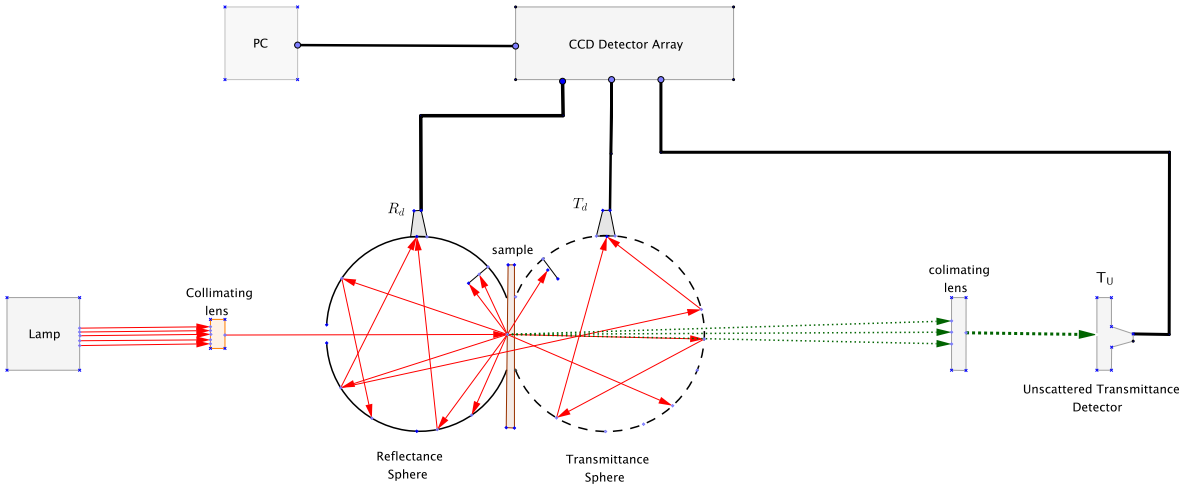

Figure 2.7: Schematic of experimental setup. Light from a white light source incident on a sphere is captured at the sphere detector ports, and the signal relayed via fibre optic wire to a CCD. The transmission sphere can be slid out of the way to in order to measured the unscattered collimated transmittance.

Two general purpose integrating spheres were purchased from Labsphere Inc. (North Sutton, NH). The reflectance sphere (4P-GPS-033-SL) is a 3.3" diameter sphere sphere with four ports: a 1.5" sample port, and three 1" ports. The port located opposite the sample port served as the entrance port for incident light. The port

perpendicular to the sample port - called the 'North-pole port' - was closed-off with a port plug (PP-100-SL) made of the same material as the sphere wall. The detector port, situated orthogonally to the sample port, was coupled to an SMA-Adapter (SMA-100-SF/SL). The Reflectance sphere ports covered around 7.5% of the sphere wall. For transmittance measurements a three-port, 3.3" diameter sphere (3P-GPS-033-SL) was used. As before, the unused North-pole port was plugged, while the detector port was coupled to an identical SMA-Adapter. The port fraction for the transmission sphere was 5.2%. Both spheres had a highly reflective Spectralon® coating on the inner wall surface.

The spheres were mounted on an adjustable rail system that allowed for varying of the distance between the two sample ports depending on the sample size. For calibration measurements that require no sample to be present, the two sample ports can be kept flush with each other, ensuring minimal light loss from the ports. A third detector for measuring unscattered transmittance (T_U) was placed 50cm away from the transmittance sphere. Because the transmittance sphere has no exit port, for protocols involving T_U, this sphere can be moved laterally out of the way of the incident beam.

The SMA-Adapters on the detector ports, and the independent unscattered transmittance detector were attached to optical fibres that relayed the signal from the spheres to a CCD detector connected to a PC. Reflectance and Transmittance measurements were performed simultaneously, and the unscattered transmittance measurement, when needed, performed separately.

The data collected from the PC was, after some collation, fed into IAD for analysis.

2.6.1 Sphere Wall Reflectance

While manufacturer-provided sphere wall reflectance values can be used in good faith, it is often prudent to perform a sphere wall calibrations specific to experimental conditions. According to Prahl (2011), only two measurements are needed: a diffuse reflectance measurement - i.e. with light first incident on the sphere wall - made in the presence of a standard (R^d_{std}), and a diffuse reflectance measurement made with an open sample port (R^d_0). The sphere wall reflectance (m) can be calculated by inverting the equation:

$$\frac{1}{m} = a_w + a_d r_d (1 - a_e) + a_s r_{std} (1 - a_e) \frac{R^d_{std}}{R^d_{std} - R^d_0} \tag{2.6.1}$$

where a_w, a_d, a_s and a_e are the relative areas of the sphere wall, detector, sample and entrance ports respectively; r_d and r_{std} are the reflectances of the detector window and the reflectance standard respectively. The two diffuse measurements (R^d_{std}) and (R^d_0) will only differ by the amount of light leaking from the sphere when the sample port is open. Consequently the difference will be small and any errors in the measurements will be magnified when the division is performed. Thus it is desirable to use highly

reflective standards so that the difference between these measurements is as great as possible (Counter 2010; Prahl 2011).

2.6.2 Measuring Reflectance and Transmittance

IAD estimates the optical properties characterizing a sample by using the measured total reflectance M_R, the measured total transmittance M_T, and (if applicable) the measured unscattered transmittance M_U. As mentioned earlier in section 2.4, a set of optical properties is guessed and values for M_R and M_T are calculated and compared with the measured values. If they match then the optical properties have been found, otherwise a new set of optical properties is guessed and the process is repeated.

A set of five measurements outlined in figure 2.8 was made in order to obtain reflectance and transmittance. In accordance with Prahl (2011), $R_2(r_s^{direct}, r_s, t_s^{direct}, t_s)$ refers to the reflection measured in the first sphere and $T_2(r_s^{direct}, r_s, t_s^{direct}, t_s)$ the transmission measured in the second sphere in the presence of an intervening sample. $R_2(r_{std}, r_{std}, 0, 0)$ is the reflection measurement made in the first sphere in the presence of a high reflectance standard. $T_2(0, 0, 1, 1)$ is the measurement made in the transmittance sphere in the absence of the sample. $R_2(0, 0, 0, 0)$ is a background measurement done only on the first sphere in the absence of both a sample and cross-talk from the transmittance sphere, and finally $T_2(0, 0, 0, 0)$ is a dark measurement in which no light from the source enters the spheres.

From these, the total normalized reflectance is given by:

$$M_R = r_{std} \cdot \frac{R_2(r_s^{direct}, r_s, t_s^{direct}, t_s) - R_2(0, 0, 0, 0)}{R_2(r_{std}, r_{std}, 0, 0) - R_2(0, 0, 0, 0)} \tag{2.6.2}$$

and transmittance by

$$M_T = \frac{T_2(r_s^{direct}, r_s, t_s^{direct}, t_s) - T_2(0, 0, 0, 0)}{T_2(0, 0, 1, 1) - T_2(0, 0, 0, 0)} \tag{2.6.3}$$

A different set of measurements was made for the total unscattered transmittance (fig. 2.9). In this case, the transmittance sphere is shifted out of the way (see schematic fig 2.7 while the sample is left in place. Two measurements U_s and U_0 are then made, and the sample is removed for the final measurement U_{100}. Here U_s is the amount of unscattered light that has gone through a sample, U_0 is the background measurement made with the beam blocked, and U_{100} is the unscattered transmission measurement when no sample is present. The amount of light that gets through the sample without being scattered or absorbed is called the measured unscattered transmittance.

$$M_U = \frac{U_s - U_0}{U_{100} - U_0} \tag{2.6.4}$$

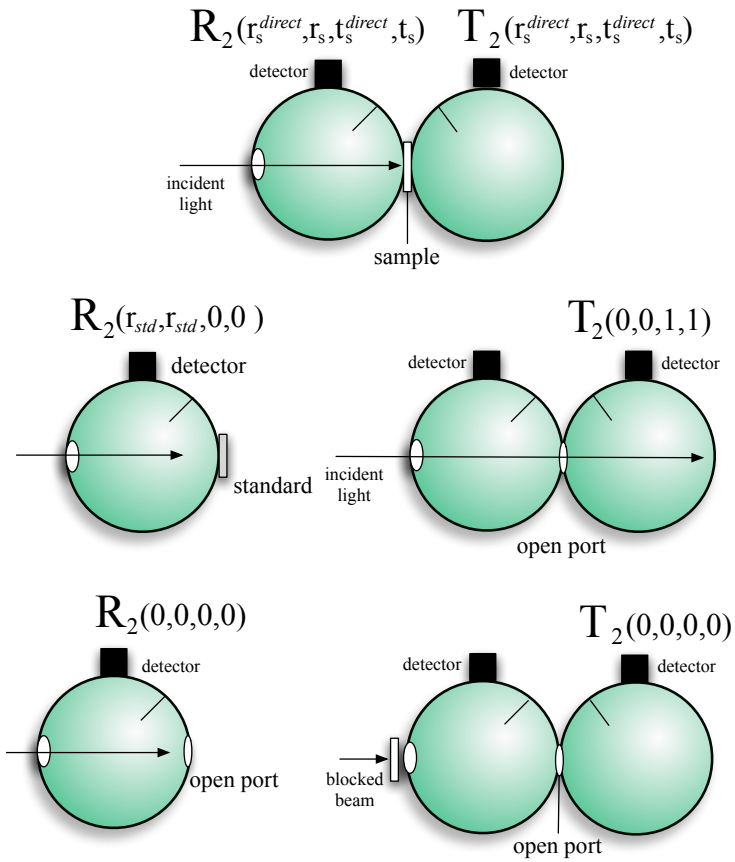

Figure 2.8: The five Measurements needed for M_R and M_T when two integrating spheres are used simultaneously. The subscript 2 indicates a double integrating sphere setup (Prahl 2011)

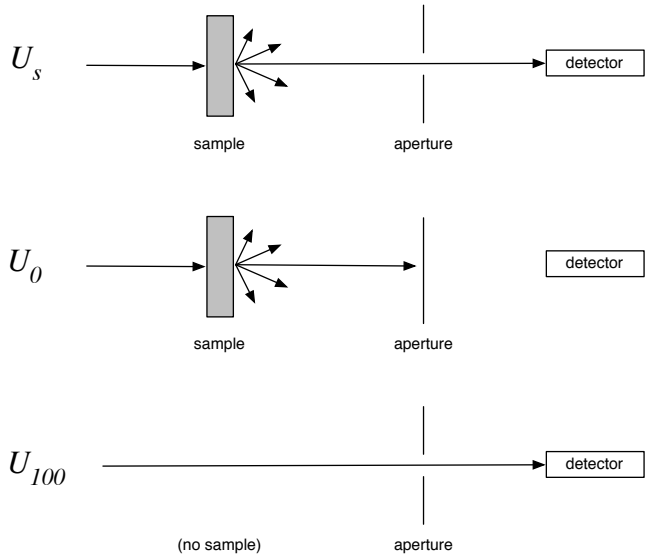

Figure 2.9: The three Measurements needed for M_U (Prahl 2011)

2.7 Known-property Measurements

Phantoms with known optical properties are usually used for the validation and calibration of optical measurement systems. To validate the integrating sphere system, lipid emulsion phantoms were prepared as scattering samples. Food colouring and black ink were added in differing ratios as absorbers. These sets of phantoms were also measured independently using a spatially resolved reflectance spectroscopy system (Hyde et al. 2001; Moscu 2009).

2.7.1 Intralipid Phantoms

Intralipid™ is a fat emulsion administered clinically as an intravenous nutrient. Because it is readily available, turbid and has no strong absorption bands in the visible region of the electromagnetic spectrum, it is often used as a tissue simulating phantom medium in light dosimetry experiments (Flock et al. 1992) .

The scattering of Intralipid-10% can be described using a simple power law (Pogue and Patterson 2006; Van Staveren et al. 1991). The study by Van Staveren et al. (1991) used measurements of optical transmission combined with Mie theory to yield scattering and anisotropy spectra for Intralipid:

$$\mu_s(\lambda) = 16\lambda^{-2.4} \tag{2.7.1}$$

$$g(\lambda) = 1.1 - 0.58\lambda \tag{2.7.2}$$

where λ is in micrometers, and μ_s is in mm^{-1}. Following the logic of equation 1.3.14, the reduced scattering coefficient becomes

$$\mu_s'(\lambda) = 9.3\lambda^{-1.4} - 1.6\lambda^{-2.4} \tag{2.7.3}$$

The reduced scattering coefficient of Intralipid is wavelength dependent and increases proportionally with concentration such that $\mu_s' \propto [conc.] \times (\lambda^{-1.4} + \lambda^{-2.4})$ (Moscu 2009; Van Staveren et al. 1991).

2.8 PVA Cryogel Production

Standard Operating Protocols for PVA-C manufacture developed by Dr. Campbell were adapted in their entirety for in-house production of PVA-cryogels. In addition, batches of PVA-cryogels manufactured at the National Research Council of Canada (NRC-IMI, London ON) were examined, and their optical properties compared to those made in-house.

2.8.1 Sample Composition

PVA-C slabs received from the NRC were prepared from hydrogrel concentrations varying from 5% to 20% w.t. Commercial grade PVA (Sigma-Aldrich) with 99+% hydrolysis and average molecular weight 146,000-186,000 was used for all samples. Samples were prepared as separate sets sorted according to preparation atmosphere as well as solvent (water vs DMSO). Samples were prepared under the following conditions:

- Samples prepared in water at ambient atmospheric conditions
- Samples prepared in water under a nitrogen-purged (hypoxic) environment
- Samples prepared in different mixtures DMSO-water at ambient atmospheric conditions

All NRC-IMI samples were produced at one, three or six freeze-thaw cycles. Due to equipment constraints at the Juravinski Cancer Centre, all samples were prepared in water under ambient atmospheric conditions.

2.8.2 Freeze-Thaw Cycling

In-house cryogels were cast in plate moulds consisting of aluminium top and bottom plates secured with screws. Moulds consisted of two pieces of 8.5mm thick aluminium secured with screws around the perimeter. A 15 cm x 15 cm square depression was milled out of the bottom plate to a depth of 2mm. Each mould is designed to hold approximately 15mL of liquid.

Following NRC-IMI protocol, the moulds containing hydrogels were placed in a programmable Model 107 Benchtop Temperature chamber (TestEquity LLC, Moorpak, CA). The temperature was ramped from 20°C to -20°C over 6 hours, and held at that temperature for 1 hour before being ramped back up to 20°C over another 6 hours, and held at that temperature until retrieval. This process constitutes one freeze-thaw cycle. Because the Model 107 chamber allows for the programming of multiple freeze-thaw cycles, running multiple freeze-thaw cycles akin to those of the NRC-IMI samples was trivial.

System Calibration and Characterization

The integrating sphere setup was calibrated, and a series of tests were performed to gauge the ability of the system to reliably recover optical properties of known materials. First, the reflectivity of the sphere walls was measured using the same white light source used in the rest of the study; the values obtained were used as input parameters in IAD. Sets of optical property recovery measurements were performed on differing concentrations of Intralipid™phantoms, with and without absorber. Integrating sphere measurements for lipid phantoms were then compared to those obtained from an in-house Spatially Resolved Reflectance system.

3.1 Sphere Wall Calibration

The Sphere wall reflectance is one of the most crucial input parameters in integrating sphere theory and the IAD algorithm. Although Lasphere Inc. claims the spheres used herein have a Spectralon® coating with diffuse reflectance >98% over 400nm to 1500nm, it is always advisable to conduct a sphere wall measurement.

Measurements with a white light source yielded reflectance spectra for the coating on the sphere walls of the reflection and transmission spheres (Figure 3.1b). Using the method described in 2.6.1, the average sphere wall reflectance was measured at 90.25% and 89.16% for the reflection and transmission spheres respectively over the wavelength range 550 - 950nm, a gross underestimation of manufacturer-reported reflectances (figure 3.1a). The wall reflectance values result in average sphere multiplier (see section 1.4.3) values of 5.46 and 5.76 for the reflection and transmission spheres respectively.

It is unclear why figure 3.1b exhibits a hump at around 750nm. This oddity was observed for both spheres, implying it might be intrinsically tied either to the sphere design or the lighting system. Curiously, the reflectance signals of the two spheres cross at said point, instead of continuing in parallel. Given the odd shape of the sphere wall reflectance curves (cf. figure 3.1a), as well as the noisy extremities, and to avoid any skewing of data, average sphere wall reflectance values were not used. Since IAD allows the pairing of reflectance and transmittance measurements at any wavelength to the sphere wall reflectance specific to that point, this approach was used instead.

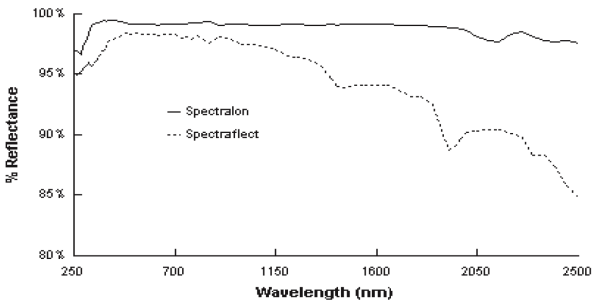

(a) Reflectance of Spectralon as function of wavelength (Labsphere 1999)

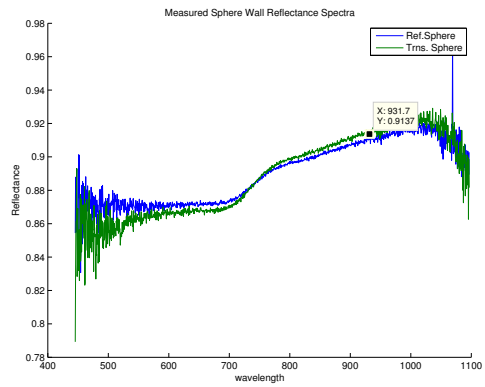

(b) Sphere wall reflectances for Spectralon-coated integrated spheres used in setup

Figure 3.1: Sphere wall reflectance as a function of wavelength for the reflection and transmission spheres. The diagram on the left shows the spectrum of spectralon as reported by the manufacturer

Pairing reflectance and transmittance values with sphere wall reflectances results in a modest but noticeable change in the graph of the reduced scattering coefficient (fig.3.2). Using average sphere wall reflectance appears to overestimate the reduced scattering coefficient for wavelength values lower than 750nm. Above 750nm the opposite is observed. It is possible that the anchoring of the scattering profile at 750nm is due to the white light source used in the setup. The beam has maximum intensity at 750nm (fig.3.3), and quickly tapers off at either side of that wavelength. At the extremities, the intensity is reduced to less than 10%, resulting in the noisy spectrum edges observed in figure 3.1b.

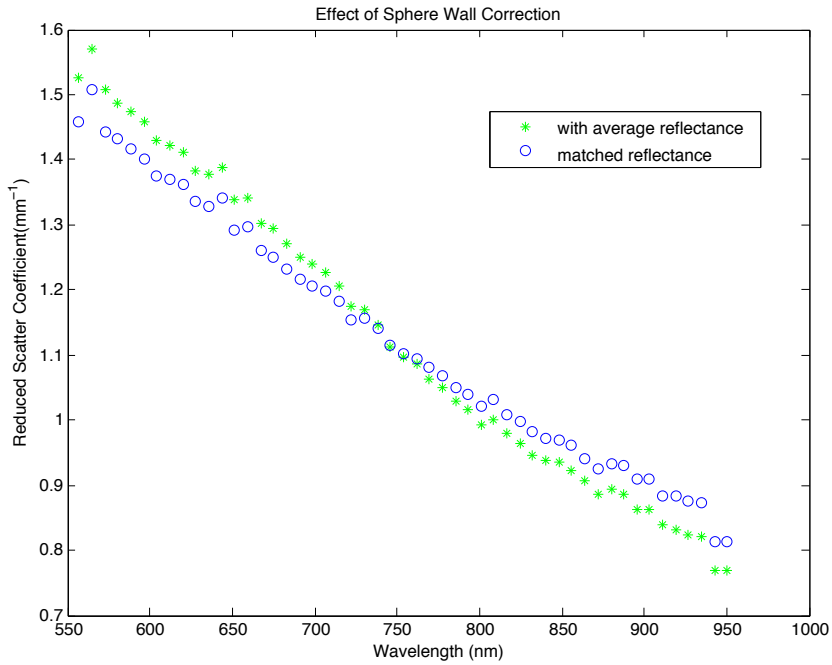

Figure 3.2: Influence of Sphere Wall Reflectance on the Reduced Scattering Coefficient. Using the average reflectance values overestimates the reduced scattering coefficient at lower wavelengths.

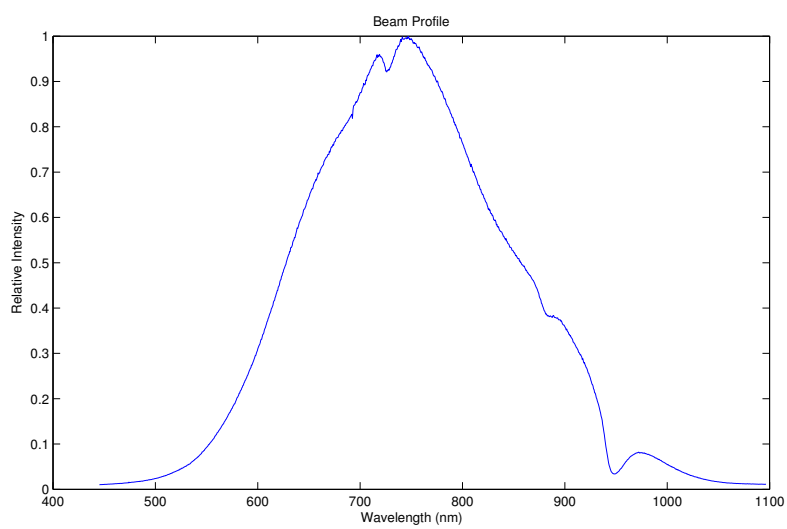

Figure 3.3: White light source beam profile measured on the 99% reflectance standard using the integrating sphere system

3.2 Optical Property Recovery

IAD's ability to recover optical properties from sets of theoretical and experimental Reflectance and Transmittance measurements was examined. A grid of optical properties (μ_s', μ_a) was generated, from which the corresponding single scatter albedo and optical thickness were computed for a 1.9 mm sample for input into the forward Adding-Doubling algorithm. The obtained reflectance and transmission coefficients were used as input parameters in IAD. For comparison, the same data were analyzed with the Magic Light inverse Monte Carlo program (henceforth IMC) introduced in section 2.5.1.

3.2.1 Integrating Sphere Corrections

Previous studies have found the effects of integrating spheres to be quite significant, giving differences of up to 20% between recovery parameters (Cruzado et al. 2013; Morales Cruzado et al. 2011, poster). Both IAD and IMC incorporate correction algorithms to account for the effects of integrating spheres. They also provide the user with the option to disable the corrections, which presents an opportunity to examine their impact. The effect of integrating sphere corrections was investigated by feeding Reflectance and Transmittance values generated by Adding-Doubling into IAD, and running the program with parameters that accounted for zero, one, or two integrating spheres. The first case (zero spheres) assumes the reflectance and transmittance measurements were made in such a way that they were devoid of integrating sphere errors. The second case assumes a single sphere has been used to measure both reflectance and transmittance, or that a second sphere is present in a way that does not affect the results of the sphere making the measurements.

		zero		one		two	
$\mu_{s'}$	μ_a	$\mu_{s'}$	μ_a	$\mu_{s'}$	μ_a	$\mu_{s'}$	μ_a
0.2	0.01	0.2016	0.01006	0.2929	0.01102	0.108	0.0432
	0.05	0.2014	0.05027	0.2754	0.0461	0.085	0.106
2.0	0.01	1.994	0.01008	2.854	0.0098	2.738	0.0188
	0.05	1.994	0.05025	2.744	0.0430	2.632	0.0516
4.0	0.01	3.984	0.01007	5.560	0.0094	5.527	0.0165
	0.05	3.984	0.0503	5.395	0.0498	5.303	0.0496
8.0	0.01	8.814	0.00805	10.90	0.0091	10.8	0.0150
	0.05	7.961	0.05024	10.64	0.04887	10.39	0.0489

Table 3.1: Effects of Integrating Sphere Corrections on optical properties. The first two columns show the optical properties used to generate Reflectance and Transmittance parameters in AD. The rest of the columns show optical properties retrieved by IAD after applying corrections with zero, one, and two spheres. All measurements in mm^{-1}.

Table 3.1 is a brief summary of the effects of integrating sphere corrections at

select points. The optical properties returned by IAD without integrating sphere corrections seemed to agree well with the set fed into AD, save for scattering and absorption coefficients returned for the highest level of scattering at low absorption ($\mu_s' = 8\ \mathrm{mm}^{-1}, \mu_a = 0.01\ \mathrm{mm}^{-1}$).

For single and double-sphere corrected data, the scattering and absorption coefficients were exaggerated when compared to the no-sphere case. Magic Light gives no single-sphere correction option, but IMC data (omitted), showed a similar overestimation of optical properties in the double-sphere case. Just like IAD, the algorithm overestimates the values for low absorption ($\mu_a \leq 0.01\,\mathrm{mm}^{-1}$) and scattering ($\mu_s' \leq 0.3\,\mathrm{mm}^{-1}$) coefficients.

3.2.2 Pure Scattering Phantoms

Varying concentrations of both purely scattering Intralipid™ and absorbing (Intralipid™ and food coloring) phantoms were prepared from a 20%-Intralipid stock solution diluted in distilled water. The liquid phantoms were held in a 1.9mm deep quartz container machined at the JCC, and held between the sample ports of the integrating spheres. Reflectance and transmittance measurements were made with the integrating sphere system, and a set of optical properties (μ_s', μ_a, g) recovered in IAD and IMC. A separate set of measurements was taken using the spatially resolved reflectance system. Liquid phantoms were held in a 10cm x 10cm x150cm black container to simulate a semi-infinite medium, and reflectance measurements taken with a probe connected to a detector array. The design and function of the SRS probe is discussed in great detail by Moscu (2009).

Reduced Scattering Coefficients

Figure 3.4 shows the spectrum of the reduced scattering coefficient of Intralipid-1% versus wavelength obtained from IAD and IMC. The recovered values were compared to literature data reported by various groups (Van Staveren et al. 1991) and (Michels et al. 2008) .

Both IAD and IMC while showing a linear increase in scattering with concentration, underestimated the reduced scattering coefficient reported in the literature for all concentrations of Intralipid. As the concentration of intralipid - and hence scattering - was increased, an increasing divergence between literature and experimental data was observed (fig. 3.5). In addition to deviating from the literature, IAD and IMC gradually diverge themselves as the scattering increases. The effect is most pronounced at wavelengths lower than 700nm (see fig 3.6), with a maximum discrepancy of 18% at 612nm for 5% Intralipid. For lipid concentrations above 5%, both algorithms deviate substantially from van Staveren's literature data, and begin to show a marked divergence between themselves.

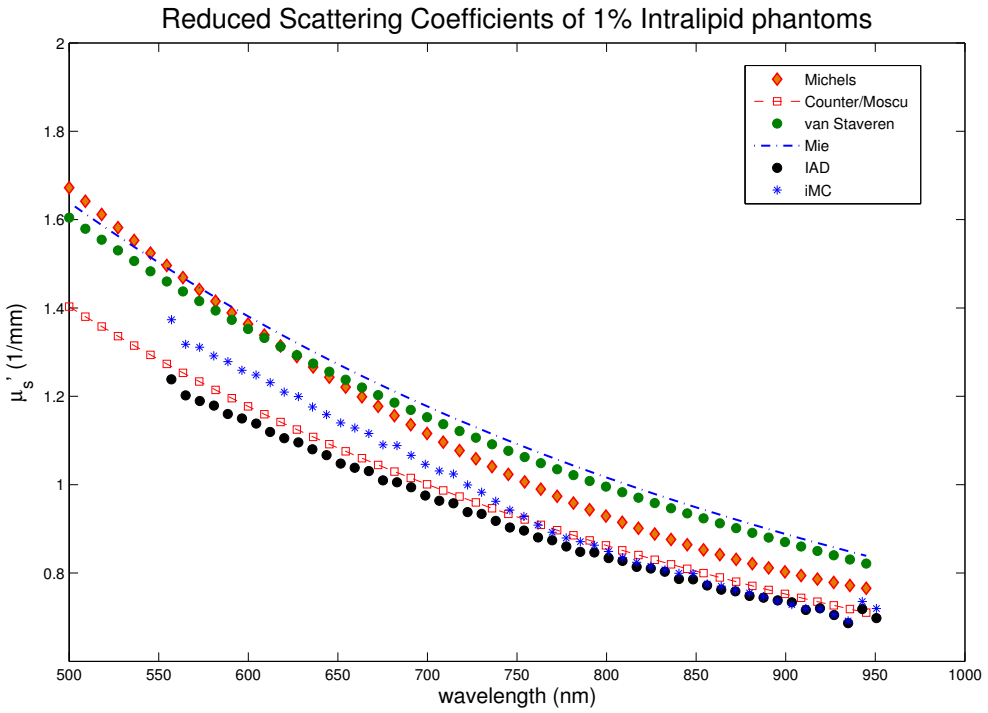

Figure 3.4: Reduced Scattering Coefficient of Intralipid-1% recovered by IAD and IMC compared to literature values. Errors bars omitted.

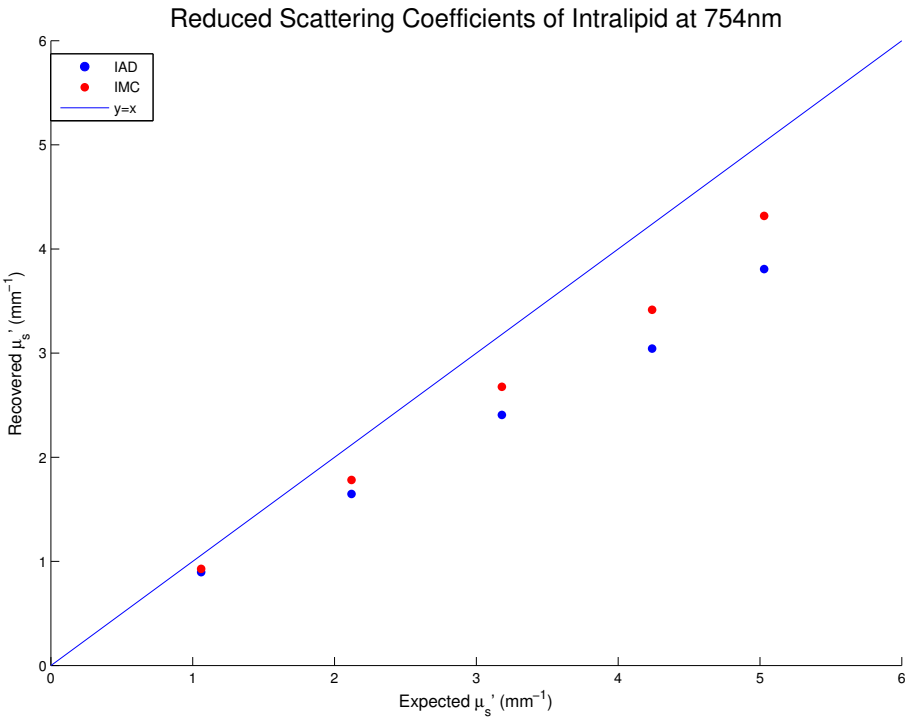

Figure 3.5: Reduced Scattering Coefficients recovered with IAD and IMC plotted against van Staveren literature values. The solid line represents equality between expected and recovered scattering coefficients.

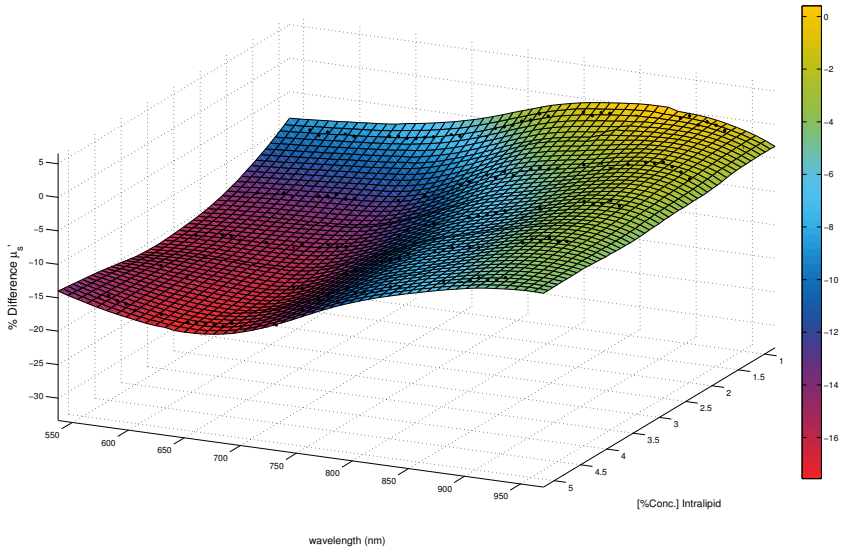

Figure 3.6: Percentage Difference in the reduced scattering coefficient recovered by IAD and IMC. IAD underestimates IMC for all concentrations of Intralipid at all wavelengths.

Anisotropy Factor

Anisotropy factors were recovered for all concentrations of Intralipid. While both Michels et al. (2008) and Van Staveren et al. (1991) reported anisotropy factors that could be fit to linear functions, integrating sphere recovered anisotropies did not follow such linear trends (fig. 3.7). Unlike the reduced scattering coefficients (fig. 3.4), the anisotropy values for the two methods almost perfectly overlapped over all wavelengths, with disagreement observed at the the lowest wavelengths where IAD and IMC data begin to fall off. The trend was observed for all concentrations and is perhaps due to some detector inefficiency at such wavelengths. The anisotropy factor was observed to decrease with increasing intralipid concentration (fig. 3.8) for all wavelengths for both IAD and IMC. This is contrary to the findings of Royston et al. (1996), in which the anisotropy factor was observed to be fairly constant at different lipid concentrations. Another anomaly was observed, in which both IAD and IMC retrieved negative anisotropy factors at high lipid concentrations. It could be that as the optical depth increases with increasing scattering due to concentration, the algorithms simply start to fall apart.

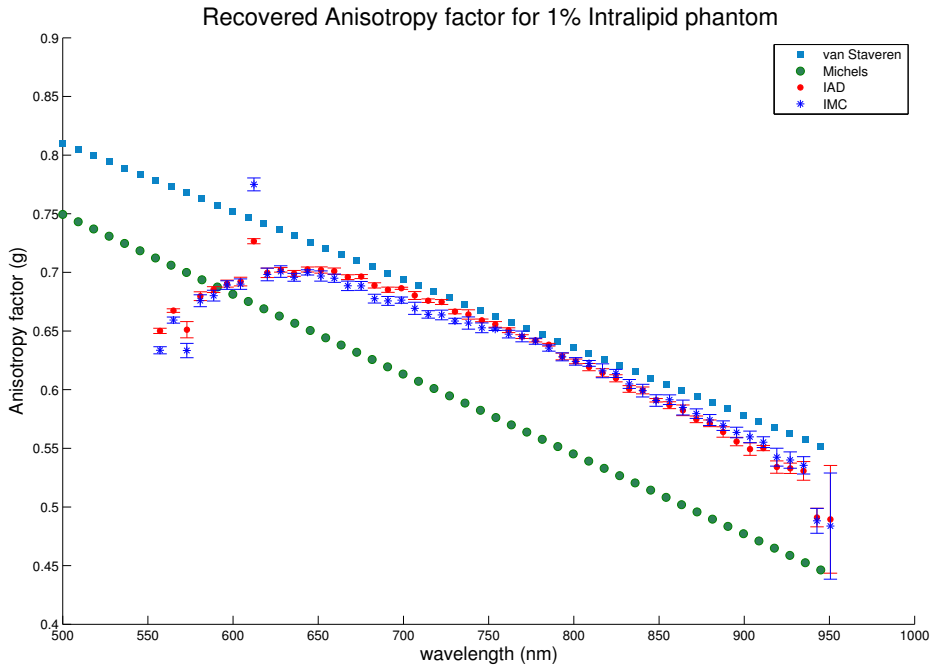

Figure 3.7: Anisotropy factor recovered for a Intralipid-1% sample. Overlaid are anisotropy factors reported by Michels et al. (2008) and van Staveren et al. (1992).

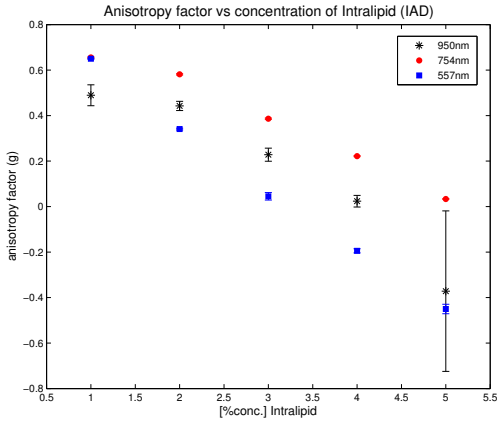

(a) Scattering Anisotropy factor recovered in IAD

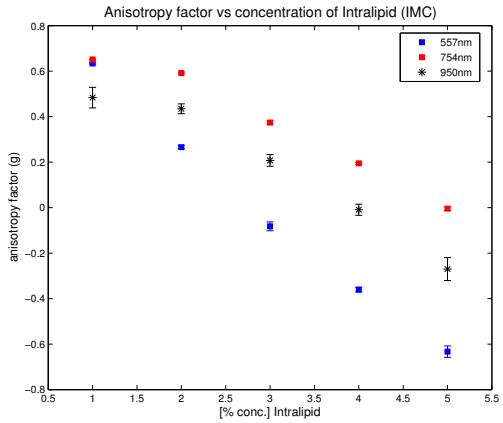

(b) Scattering Anisotropy factor recovered in IMC

Figure 3.8: Dependence of the Anisotropy factor on Intralipid concentration. Data shown for IAD and IMC at 557, 750 and 950nm.

Comparison with a Spatially Resolved Reflectance System

Optical properties of scattering samples were verified using a Spatially Resolved Reflectance System (SRS), in which the dependence of the measured reflectance on the distance from the source is used to determine optical properties. The data were fitted with a monte carlo based non-linear regression model. The SRS used herein is a mainstay 'gold standard' employed for a long time at the Juravinski Cancer Centre. A full description of this particular system is described elsewhere (Moscu 2009).

Varying concentrations of bulk volume phantoms of purely scattering intralipid designed to simulate semi-infinite media were measured with the SRS. Aliquots drawn from these bulk samples were analyzed with the Integrating sphere system.

Figure 3.9 shows the spectrum of the reduced scattering coefficient for a sample of Intralipid-1%. As observed earlier with literature data, integrating sphere measurements underestimate the reduced scattering coefficient of Intralipid. This behaviour is observed for all concentrations of Intralipid at all wavelengths, as seen in figure 3.10, which shows the reduced scattering coefficients of different concentrations of Intralipid retrieved at 750nm.

From figure 3.10, it can be seen that the the discrepancy between SRS and Integrating Sphere measurements widens as the relative error also increases with increasing lipid concentration. The effect is most pronounced for IAD. Figure 3.11 shows the degree of these discrepancies between the two systems as a function of the wavelength as well as lipid concentration. Above 750nm, the discrepancy remains mostly modest, with sharp increases at around 950nm. A more pronounced increase is observed at wavelengths lower than 750nm, with the greatest difference showing at

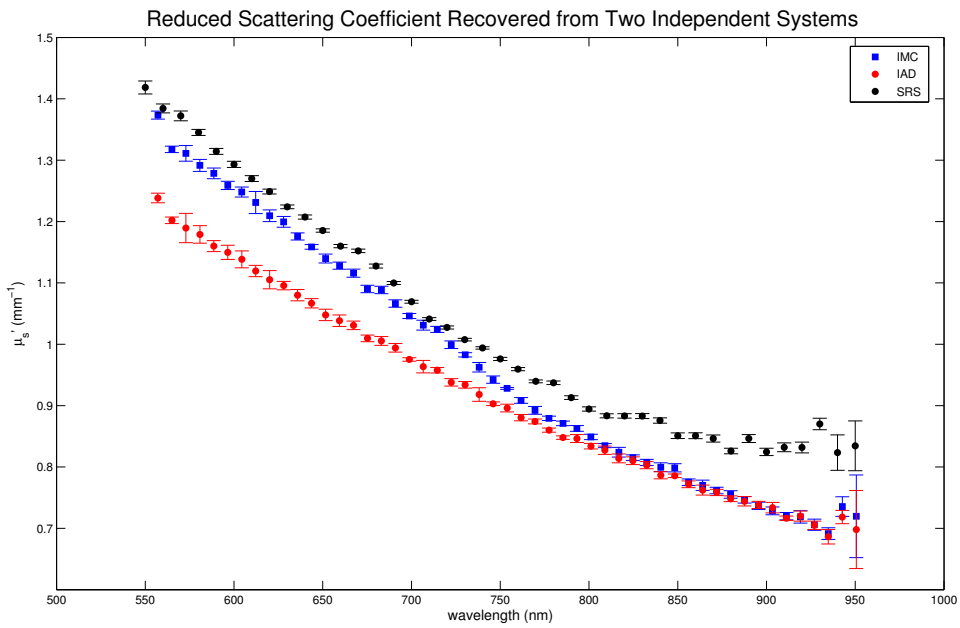

Figure 3.9: Reduced Scattering Coefficient spectra of Intralipid-1% samples recovered with SRS and Integrating Spheres (IAD/IMC) measurements

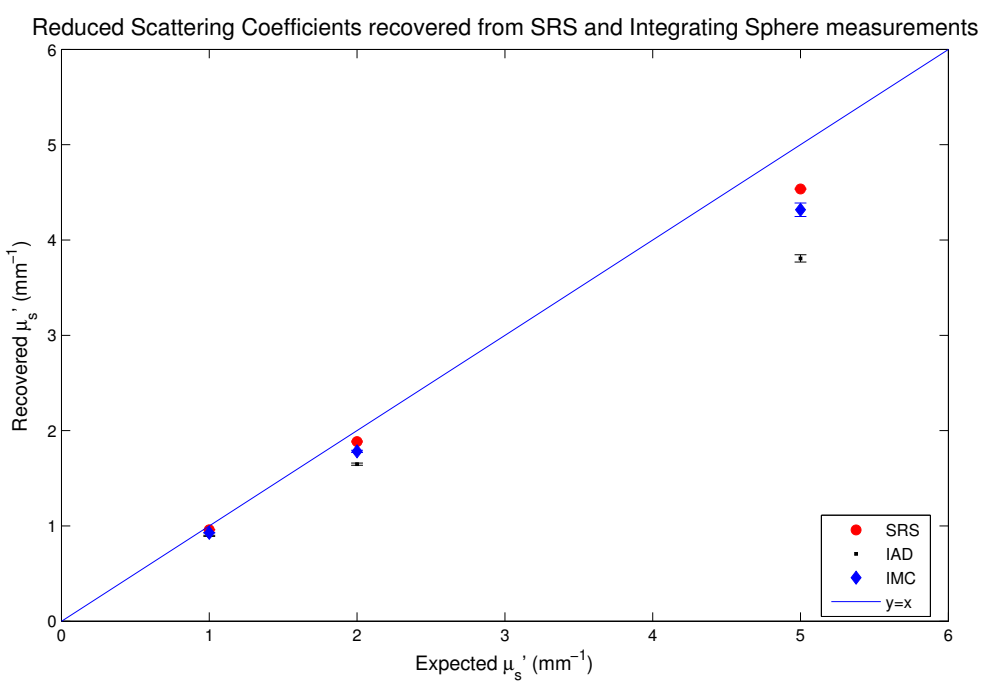

Figure 3.10: Reduced Scattering coefficients for different lipid concentrations recovered at 750nm. SRS and sphere measurements diverge as the concentration increases

the lowest wavelengths.

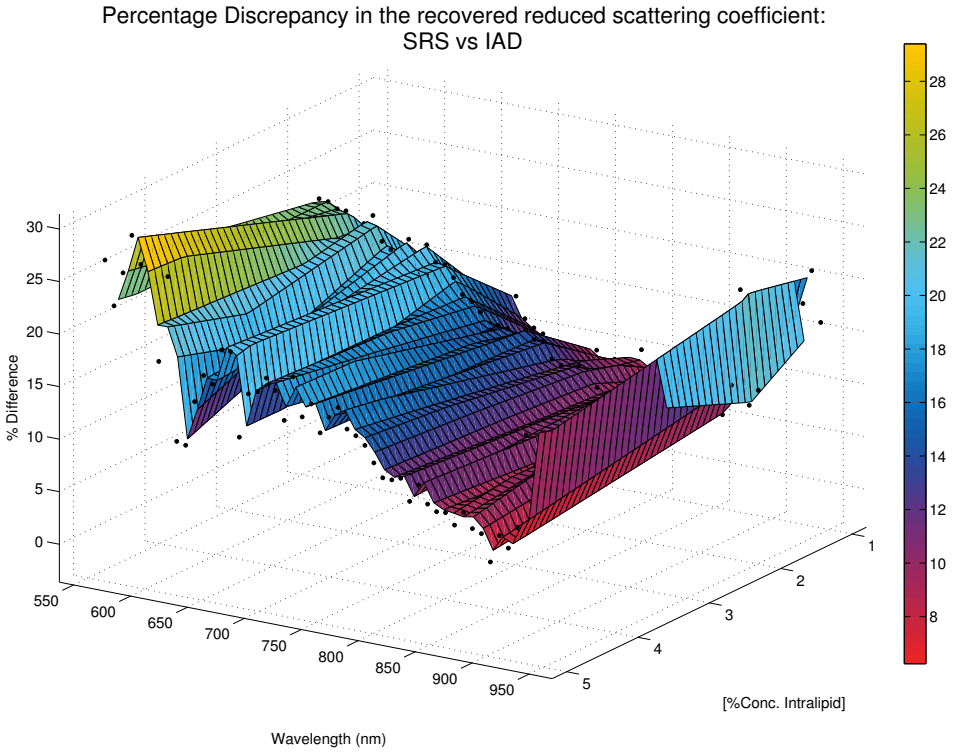

Figure 3.11: Percentage difference in the reduced scattering Coefficient of Intralipid-1% samples recovered with SRS and Integrating Spheres (IAD) measurements

3.2.3 Absorbing Phantoms

Green food coloring (TM/MD McCormick, London, ON) was chosen as an absorber material for testing the integrating sphere system's ability to recover absorption coefficients. The dye, which has a single absorption peak at around 630nm and is readily soluble in Intralipid, was characterized with a spectrometer (HR400, Ocean Optics), and an extinction coefficient calculated. From the extinction coefficient, absorption spectra – such as the one shown in figure 3.12 – were obtained for different concentrations of food dye. Another (broadband) absorber, India Ink (Reeves & Poole, Downsview, ON), was also employed and characterized for comparison.

Different concentrations of green food coloring and India Ink were added to Intralipid-1% samples to simulate differing absorption conditions. The phantoms were measured with the SRS and Integrating Sphere systems. To establish a baseline, the absorption coefficient of purely scattering Intralipid was measured with the two systems. Since pure Intralipid is an emulsion composed mostly of water, the absorption spectrum of this phantom was compared to that of pure water (Kou et al. 1993).

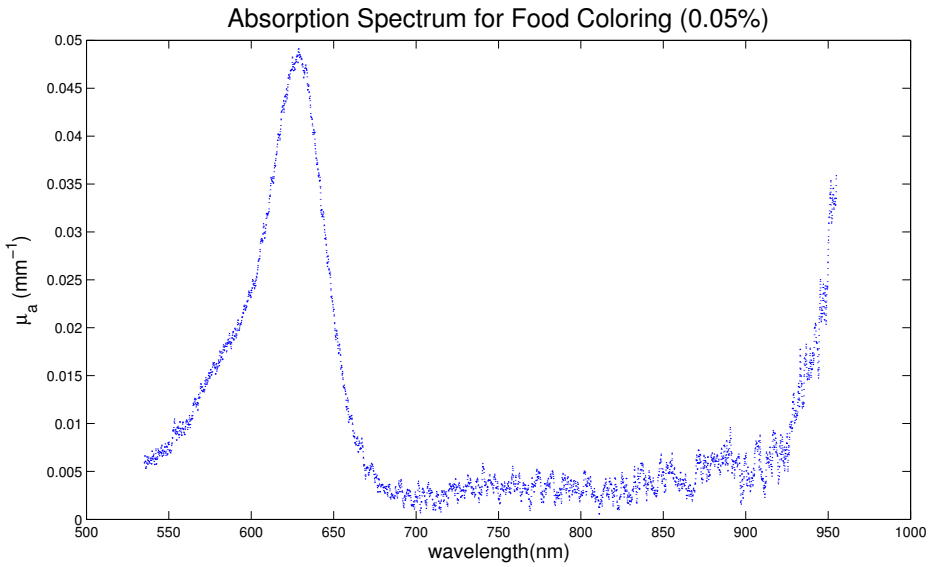

Figure 3.12: Absorption Coefficient spectrum of 0.05% Food Dye.

The absorption coefficients of purely scattering Intralipid-1% recovered by SRS and Integrating sphere measurements are plotted in figure 3.13. Overlaid onto the figure is the absorption spectrum of water. As seen in figure 3.13, SRS measurements agreed fairly well with literature data over the majority of wavelength ranges, with divergences gradually manifesting at very high wavelength ranges. Both Integrating Sphere retrieval algorithms, on the other hand, grossly overestimate the absorption coefficient of this purely scattering phantom, with greater exaggerations observed for IAD-retrieved absorption coefficients.

		Expected	SRS	IAD	IMC
Sample	[%conc.]	μ_a (mm^{-1})	μ_a (mm^{-1})	μ_a (mm^{-1})	μ_a (mm^{-1})
Food Colouring	0.005	0.00466	0.0056 ± 0.001	0.0398 ± 0.0003	0.0229 ± 0.0005
	0.05	0.04659	0.0486 ± 0.001	0.1048 ± 0.0003	0.0734 ± 0.0004
India Ink	0.01	0.0367	0.0397 ± 0.005	0.0895 ± 0.0002	0.0517 ± 0.0006
	0.05	0.1570	0.1575 ± 0.002	0.3229 ± 0.0025	0.2803 ± 0.0009

Table 3.2: Expected and retrieved absorption coefficients for Intralipid-1% phantoms with different absorbers. Food dye absorption was measured at 628nm, and India Ink at 750nm

Table 3.2 shows the absorption coefficients for Intralipid-1% doped with different concentrations of food coloring and India Ink. Both Integrating Sphere algorithms substantially overestimate absorption coefficients, even by a whole order of magnitude for very low absorbing samples. The degree of overestimation of the absorption coefficient lessened with increasing absorber concentration, though it was still unacceptably

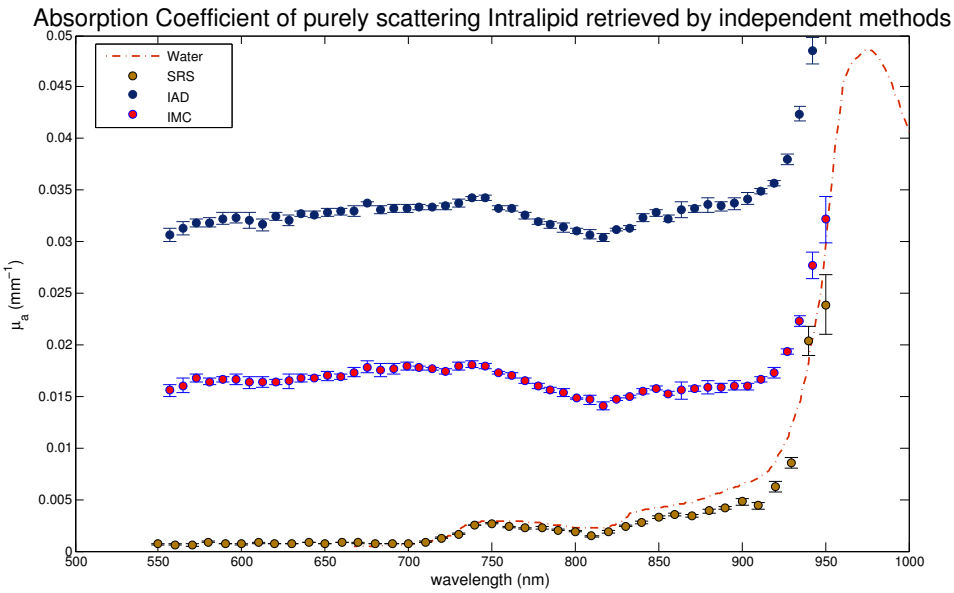

Figure 3.13: Absorption Coefficient spectra of Intralipid-1% samples recovered with SRS and Integrating Spheres (IAD/IMC) measurements.

high. Despite overestimating absorption coefficients, both IAD and IMC were shown to respond proportionally to increasing absorber concentrations. As a test, further absorption measurements were conducted on increasing concentrations of green food dye in Intralipid (figure 3.14).

Both algorithms exhibit a proportional linear response to increasing dye concentration up to concentrations of 0.1% food dye in lipid, corresponding to roughly $\mu_a = 0.1$ mm^{-1}. Regression analysis of the graphs yielded slopes equal to 1.468 ± 0.0005 and 1.132 ± 0.0005 for IAD and IMC respectively.

The effect of added absorbers on the reduced scattering coefficient was also examined (table 3.3). Ideally, added concentrations of either absorber should have a negligible effect on the scattering coefficient of Intralipid. With the addition of ink, SRS-recovered reduced scattering coefficients at 750nm showed a sustained increase with increasing ink concentration. Integrating sphere coefficients, on the other hand, follow a dissimilar trend, initially increasing at low absorber concentrations then decreasing at very high absorber concentrations for IAD. Food coloring seems to have the opposite effect on the reduced scattering coefficient measured at 628nm. SRS retrieved scattering coefficients experience a slight dip before eventually rising, while Integrating Sphere measurements experience a steady decline with increasing absorber concentration as illustrated in figure 3.15.

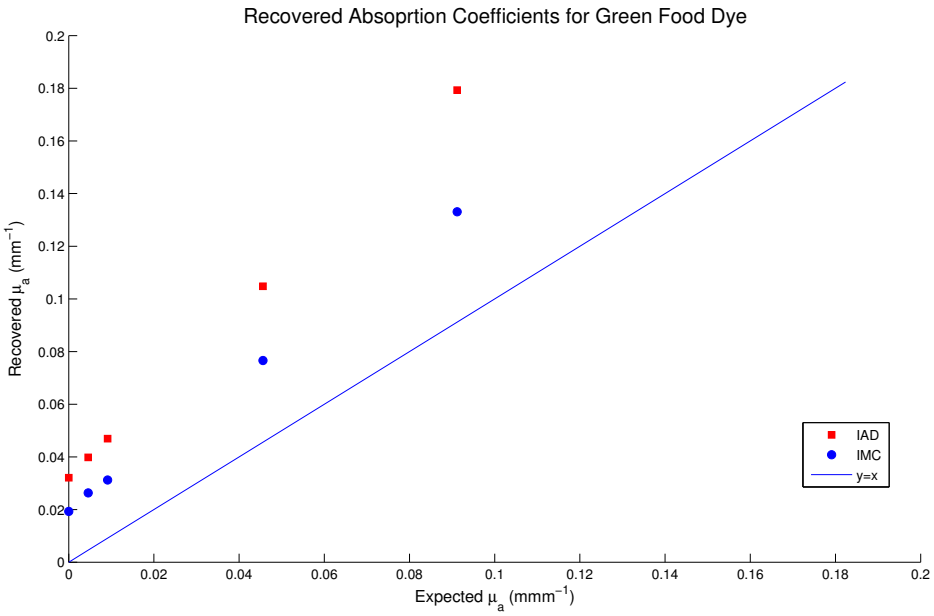

Figure 3.14: Recovered and expected absorption coefficients for green food coloring measured at 628nm for increasing concentrations of food dye. Data are shown for 0, 0.005, 0.01, 0.05 and 0.1% food dye in Intralipid

		Expected	SRS	IAD	IMC
Sample	[%conc.]	μ'_s (mm^{-1})	μ'_s (mm^{-1})	μ'_s (mm^{-1})	μ'_s (mm^{-1})
Food Coloring	0.005	1.29	1.208 ± 0.011	1.075 ± 0.005	1.171 ± 0.004
	0.05	1.29	1.243± 0.006	1.018 ± 0.006	1.133 ± 0.005
India Ink	0.01	1.06/1.01	1.008 ± 0.005	0.992 ± 0.007	1.164 ± 0.009
	0.05	1.06/1.01	1.224 ± 0.01	0.861 ± 0.004	0.965 ± 0.003

Table 3.3: Expected and retrieved scattering coefficients for Intralipid-1% phantoms with different absorbers. Food dye absorption was measured at 628nm, and India Ink at 750nm. The expected values were obtained from (Van Staveren et al. 1991) and (Michels et al. 2008).

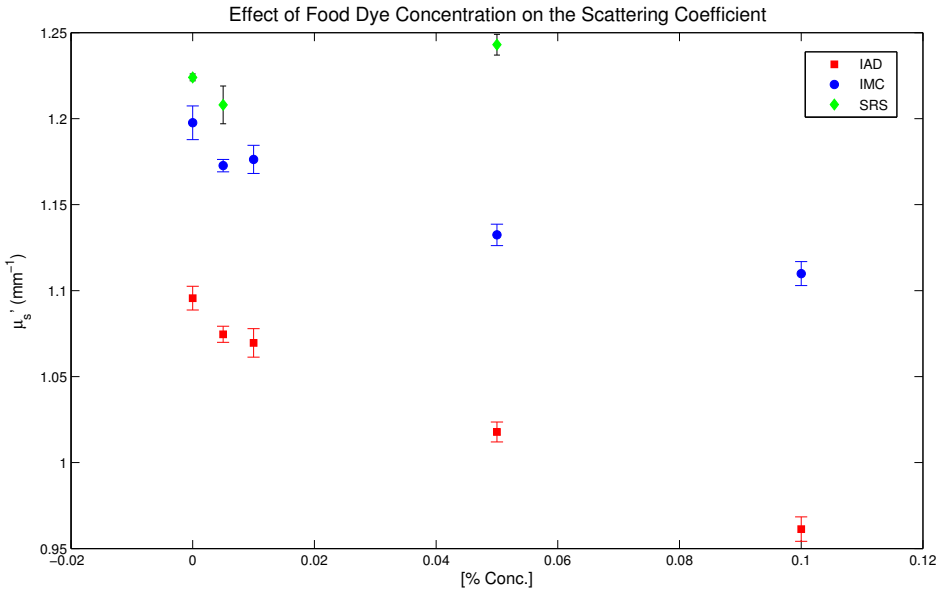

Figure 3.15: Scattering Coefficients of Intralipid phantoms with differing concentrations of food dye absorber. The error bars are the standard deviation of five measurements

3.3 IAD Sensitivities

In addition to providing the ability to set custom sphere parameters such as diameter, sphere wall reflectivity, etc, IAD lets the user set sample parameters such as the sample refractive indices and thickness, as well as setup conditions such as the beam diameter, thickness and refractive indices of glass slides (if present). Of all these parameters, only the sample thickness and beam diameter can be said to be truly variable. The former varies from sample to sample, and the latter may vary slightly from day to day, or after the apparatus had been taken apart and reassembled. To quantify the dependence of the scattering coefficient on these parameters, a random sample had its measured beam diameter of 4.77 mm changed in IAD by 0.1 mm increments in both directions up to 1.0mm, i.e. 4.77 ± 1.00 mm. No dependence of the reduced scattering coefficient on the beam diameter was observed for all wavelengths.

The same sample, measuring at 1.63 mm had its thickness adjusted by 0.1 mm increments up to 1.0 mm in both directions. The relationship in figure 3.16a was observed. A more meaningful relationship (fig. 3.16b) is obtained by observing the percentage differences of the changes in thickness and scattering coefficient (a similar result can be obtained by taking the logarithms of the axes in 3.16a). Figure 3.16b shows that an increase in the sample thickness results in an underestimation of the reduced scattering coefficient and vice versa. It is therefore crucial to measure each individual sample's thickness and to include that as a unique parameter in IAD. An exception is made for liquid samples, which are all analyzed using the same cuvette.

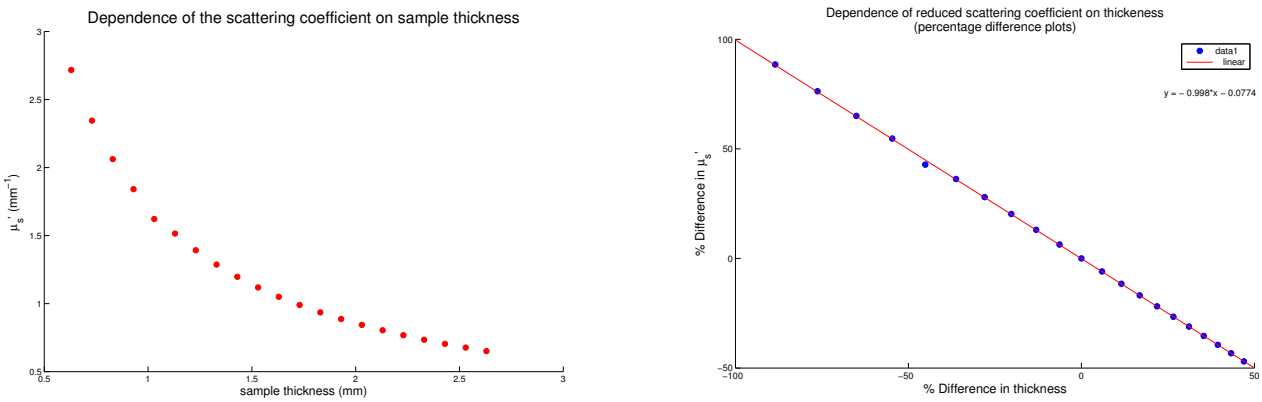

(a) (b)

Figure 3.16: Dependence of the reduced scattering coefficient on the sample thickness at 750nm.

3.4 Summary

An Integrating Sphere system was set up, and its ability to retrieve optical properties of liquid phantoms was investigated. Proper calibration of the sphere wall reflectance had a moderate effect on the measured reflectance and transmittance signal, hence by extension on the reduced scattering and absorption coefficients. Corrobrating the findings of Cruzado et al. (2013), integrating sphere corrections were observed to have an appreciable impact on the optical properties recovered by IAD and IMC. These corrections result in an inflation of the reduced scattering coefficients fed into Adding-Doubling. The increase is especially prononounced for low scattering, weakly absorbing samples. Nonetheless, even with these apparent inflations, reduced scattering coefficients recovered by IAD and IMC underestimate various sets of similar properties reported in literature. The discrepancy, however, could be attributed to using different batches of Intralipid stock solution, as has been observed in previous studies (Flock et al. 1992; Van Staveren et al. 1991). This suspicion is further heightened by the fact that IAD-retrieved reduced scattering coefficients for purely scattering Intralipid-1% were in rather good agreement with another set of optical properties obtained from previous JCC phantom studies.

There was some nonconformity between IAD and IMC-retrieved scattering coefficients, which was especially pronounced at the lower extremities. That IAD should underestimate IMC values is probably due to the sphere wall correction applied to IAD data. It is suspected that had this same correction been applied to IMC, the latter's reduced scattering coefficient slope would be lessened in a manner not dissimilar to that shown in figure 3.2. Despite the slight dissimilarity in reduced scattering coefficients, the two algorithms retrieved fairly similar anisotropy factors, decreasing with both increasing concentration and wavelength, for all lipid concentrations. The retrieved

anisotropy factors, however, were not the linear functions predicted by Mie theory and reported by Van Staveren et al. (1991).

Green food coloring and India Ink measurements demonstrated both Integrating Sphere system algorithms' deficiences at retrieving correct absorption coefficients. Even though the system demonstrates a linear response to increasing absorber concentration (see fig. **??**), the initial estimation of the absorption coefficient for non-absorbing phantoms was an order of magnitude higher than the value determined via the SRS. Though IMC is only marginally better, both algorithms gave unrealistically high absorption coefficients for all absorber concentrations. It is not quite clear whether the problem lies with the nature and amount of light collected by the system itself, or whether the algorithms' handling of absorption is inherently flawed. As it stands, the Integrating Sphere system cannot be reliably used to retrieve absorption coefficients.

Previously, Counter (2010) compared SRS recovered coefficients to those recovered from integrating sphere measurements by a custom-built Monte Carlo recovery algorithm. Integrating sphere recovered scattering coefficients overestimated those reported by the SRS, while the absorption coefficients were underestimates. These results are diametrically opposed to what was observed in this study. Investigations revealed that integrating sphere size played a crucial role optical property recovery: the author's spheres were much smaller than the ones currently deployed. To determine how the sphere size influenced results, a set of optical properties resembling those of Intralipid-1% *as reported by the SRS* , were used to generate reflectance and transmittance measurements in Adding-Doubling. The reflectance and transmittance values were then entered into two different IAD files, one with parameters adjusted to simulate the old set of spheres, and the other the current set. Retrieved optical properties were compared with SRS measurements. Calculations made with the smaller sphere parameters were indeed found to overestimate the reduced scattering coefficient and underestimate the absorption coefficient. Counter observed that the overestimation of the reduced scattering coefficient was linked to the measured reflectance being higher than predicted by the Monte Carlo algorithm, and the measured transmittance being lower. The converse was observed with this set of spheres and recovery algorithms: both algorithms (IAD and IMC) predicted higher reflectances than measured, and lower transmittances. The net result is an underestimation of the reduced scattering coefficient and an overestimation of the absorption coefficient. It should be noted, however, that in reality the amount of light collected by the two sets of spheres - hence their reported reflectance and transmittance - would be different, making this explanation inadequate at best. The only true way to investigate the phenomenon, which was unfortunately overlooked, would be to conduct measurements with both sets of spheres on identical phantoms.

Characterization of PVA Cryogels

Reflectance and Transmittance measurements of PVA-C were made with the double integrating sphere system, and the reduced scattering coefficients and scattering anisotropies recovered using IAD. Characteristics unique to each sample, such as sample thickness were also taken into account and included as input parameters in IAD. The Data are presented for JCC-manufactured samples and those obtained from the Industrial Materials Institute at the National Research Council of Canada (NRC-IMI) courtesy of Dr. Gordon Campbell.

4.1 Effect of Repeated Freeze-Thaw Cycling

The effects of repeated freeze-thaw cycling on the reduced scattering coefficient were discussed in section 1.2. Repeated freeze-thaw cycling increases the turbidity of the cryogel, which in turn results in increased optical scattering at all wavelengths. To study the effects of repeated cycling on optical properties, samples subject to the cycling protocol described in section 2.8 were removed from their moulds after each cycle, measured and then returned to their moulds for additional cycling.

4.1.1 Reduced Scattering Coefficient

Figure 4.1 shows reduced scattering coefficient spectra for a sample of 5 wt% PVA-C for 1 through 7 freeze-thaw cycles. The error bars are the standard error of the mean μ_s' of measurements made at five different regions of the slab sample. For low PVA concentrations, there appears to be no sensible trend in the reduced scattering coefficient with respect to cycling. The scattering spectrum after seven cycles sits not at the top of the graph as expected. Uniform behaviour is observed up to four cycles, after which abnormal behaviour manifests, and the scattering coefficients seem to follow no logic or pattern. Figure 4.2 shows the reduced scattering coefficients of 10 wt% PVA-C. At this concentration and above (15% and 20%), sample properties become more stable, and coherent patterns between scattering coefficients and the number of freeze-thaw cycles can be observed.

Of note in figure 4.2 is the separation of the spectral lines. Initially, the spectral lines between cycles are more or less uniformly spaced, but as the number of cycles increases,

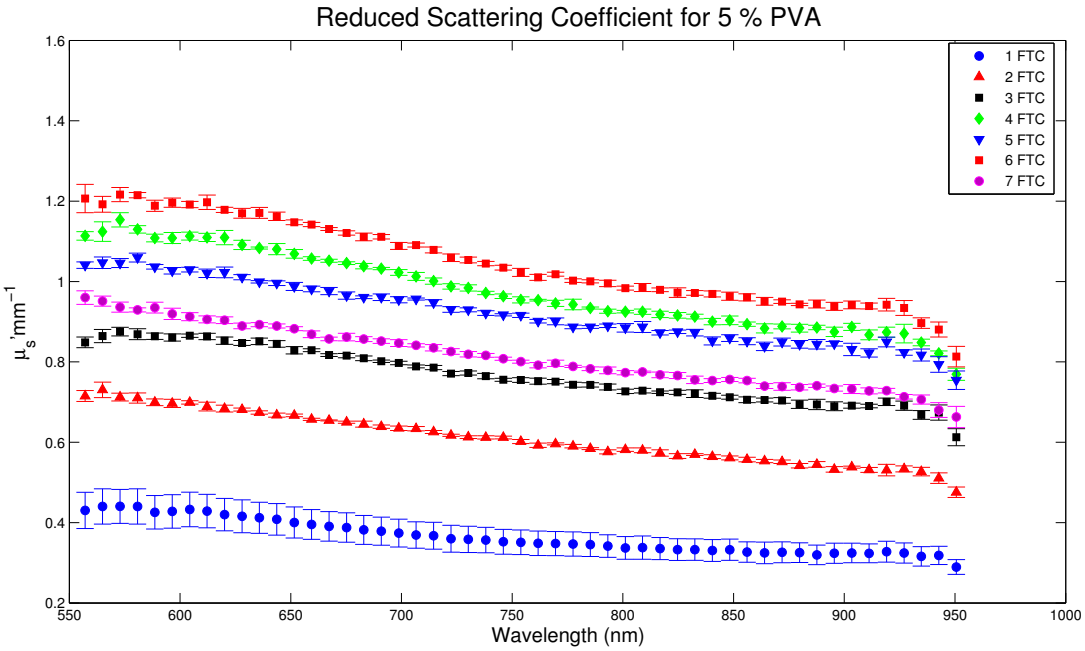

Figure 4.1: Reduced scattering coefficient spectra for 5 wt% PVA-C at 1 – 7 Freeze-Thaw cycles. Error bars are the standard error of the mean of five sets of measurements.

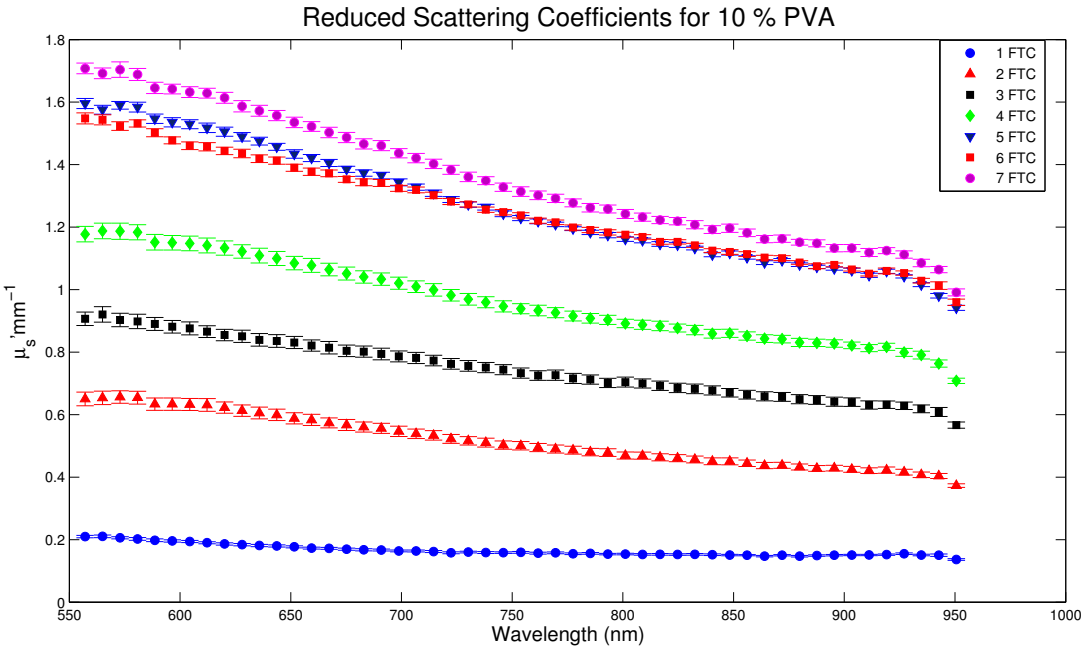

Figure 4.2: Reduced scattering coefficient spectra for 10 wt% PVA-C at 1 – 7 Freeze-Thaw cycles. Error bars are the standard error of the mean of five sets of measurements.

the spectral lines begin to cluster, which suggests an upper limit to the cycling is being reached. This behaviour is best illustrated in figure 4.3, in which scattering coefficients at 628, 750, and 900 nm are isolated for closer scrutiny. For all wavelengths, the reduced scattering coefficient increases regularly and linearly with increasing number of cycles up to five cycles, at which point the graph plateaus. Beyond this point increases in the reduced scattering coefficient are only slight and rather irregular. The same behaviour was observed for all PVA concentrations, with the lowest concentration samples exhibiting the greatest irregularity beyond five freeze-thaw cycles.

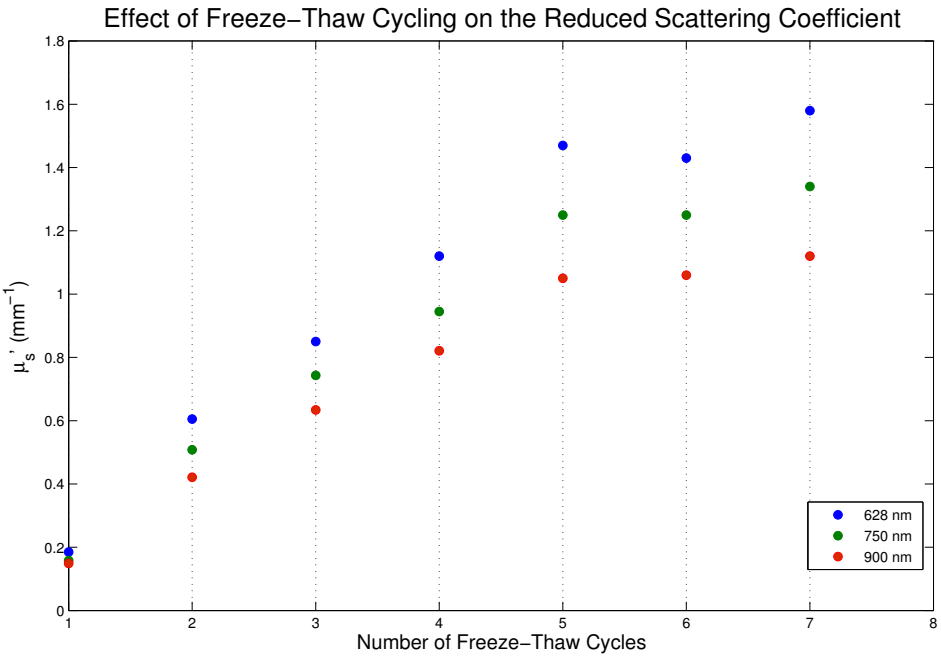

Figure 4.3: Reduced scattering coefficients as a function of repeated freeze thaw cycling for 10% PVA-C. Error bars omitted.

4.1.2 Effect of Concentration

In addition to freeze-thaw cycling, the dependence of optical properties on the concentration of PVA was investigated.

Figure 4.4 shows the effects of concentration on the reduced scattering coefficient. For an equal number of freeze-thaw cycles, cryogel samples with higher concentrations of PVA were found to be physically stiffer and more turbid upon inspection. It was assumed that the scattering coefficient would increase with increasing concentration, as the number of scattering sites increased due to potentially higher crystallization. This hypothesis held true as the concentration of the PVA increased from 5 to 15 wt%, but soon fell apart for samples with 20 wt% PVA. For all freeze-thaw cycles, the

reduced scattering coefficients of 20 wt% PVA were observed to be actually lower than those of both 10 wt% and 15 wt% for all but one cycle (3-FTC).

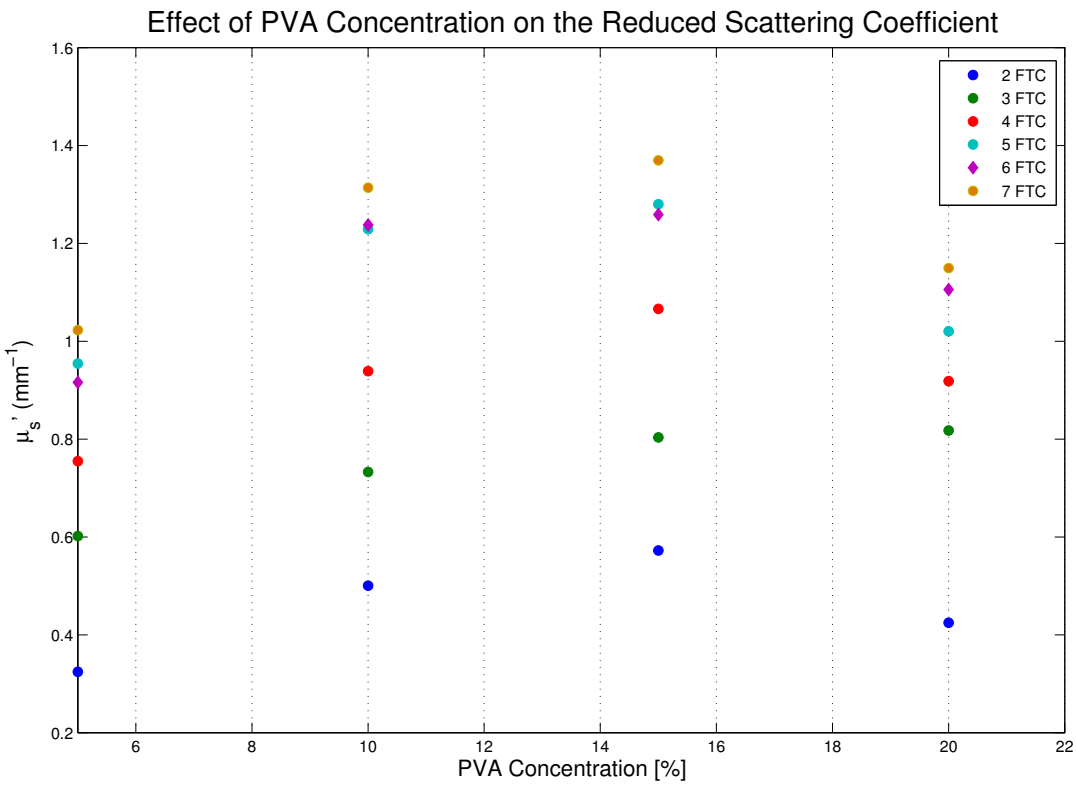

Figure 4.4: Reduced scattering coefficients measured at 750 nm for different PVA-C concentrations. Data selected for 2 – 7 freeze thaw cycles. Error bars omitted.

4.1.3 Scattering Anisotropy

The scattering anisotropy was recovered by measuring unscattered transmittance (section 2.6.2) through the PVA-C slab. This measurement was included, together with reflectance and transmittance measurements, as a parameter in IAD. The anisotropy coefficients presented in figure 4.5 were recovered from 10 wt% and 20 wt% PVA concentrations. Other concentration samples produced trends similar to that recovered in 4.5b. (Again the unstable 5 wt% PVA sample displayed peculiar behaviour in which the hepta-cycled sample returned a higher anisotropy than the same lower-cycled samples). Contrary to published literature (Devi et al. 2005), the scattering anisotropy was not constant, rather, it decreased with increasing freeze thaw cycles for all concentrations of PVA.

Table 4.1 is a summary of the recovered anisotropy at 635nm. The anisotropy coefficient decreased with increasing polymer concentration up to 15 wt% PVA. The

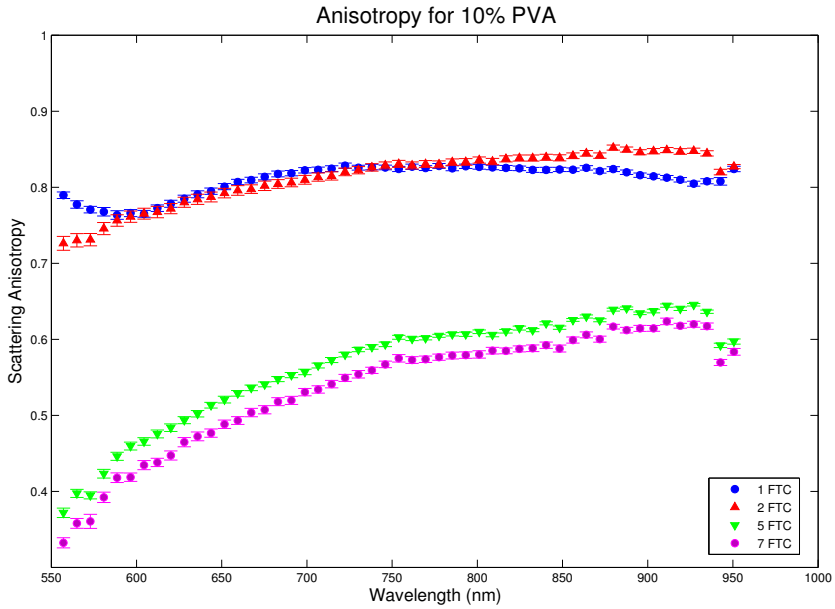

(a) Scattering anisotropy spectra for 10 wt% PVA-C.

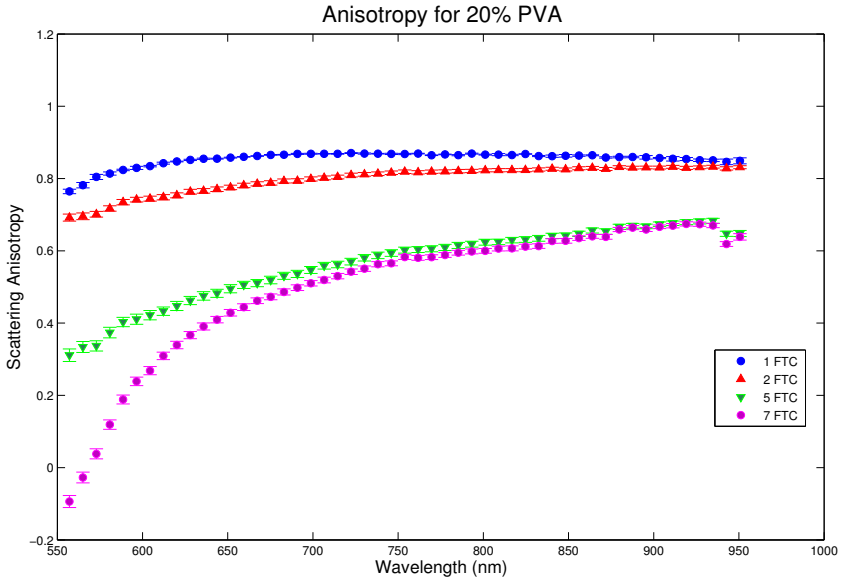

(b) Scattering anisotropy spectra for 20 wt% PVA-C.

Figure 4.5: Recovered Anisotropy factors for different concentrations of PVA-C for all wavelengths at varied freeze-thaw cycles. The error bars are the standard error of the mean for five sample sets.

20 wt% PVA sample stood out as an anomaly in that the anisotropy coefficient was consistently higher than at 15 wt% PVA. Repeated freeze-thaw cycling resulted in a reduction of the anisotropy factor for all concentrations at all wavelengths.

	wt %Conc. PVA			
FTC	5	10	15	20
1	0.890 ± 0.010	0.791 ± 0.005	0.765 ± 0.006	0.855 ± 0.002
2	0.804 ± 0.001	0.784 ± 0.007	0.728 ± 0.004	0.766 ± 0.006
5	0.719 ± 0.002	0.502 ± 0.004	0.394 ± 0.008	0.480 ± 0.010
7	0.705 ± 0.002	0.472 ± 0.006	0.342 ± 0.007	0.390 ± 0.010

Table 4.1: Recovered anisotropy at 635nm for different concentrations of PVA and different freeze-thaw cycles. 20 wt% PVA-C samples break the general pattern of falling anisotropy factor with rising PVA concentration.

4.2 NRC-IMI Gels

Samples received from the NRC-IMI were manufactured at 1, 3 and 6 freeze-thaw cycles. These samples were subjected to the same integrating sphere measurements as the in-house manufactured samples. Because characteristic reduced scattering spectra and freeze-thaw cycle trends from this batch of samples mostly resemble those of the in-house samples, they have largely been omitted save for some unique specimens that were not replicated in-house. These include samples that were (a) prepared in varying concentrations of a dimethyl sulfoxide (DMSO)-water mixture, and (b) prepared in pure water under a nitrogen-purged atmosphere. The effects of the hypoxic nitrogen environment as well as that of DMSO are explored.

4.2.1 Effect of DMSO

Translucent and transparent cryogels were prepared by mixing 10, 20 and 30% DMSO with water in the manner described by Hyon et al. (1989). According to the same authors, samples prepared in 30% had higher than 95% transmittance, making them virtually transparent.

Samples prepared in either 10 or 20% DMSO produced the now familiar reduced coefficient spectra (fig.4.6). For the 10 wt% PVA, there is hardly a discernible difference between the 10/90 (dmso/water) and 20/80 samples after the first cycle. The transparent-looking slabs (30/70), on the other hand, yielded relatively flat reduced scattering coefficients. Because of their very low scattering, IAD had trouble converging to a meaningful solution at the highest wavelengths. This effect was most pronounced for samples which had undergone only one freeze-thaw cycle. While the other two dmso formulations reacted predictably, with the reduced scattering coefficients increasing with the number of freeze-thaw cycles, the transparent slabs

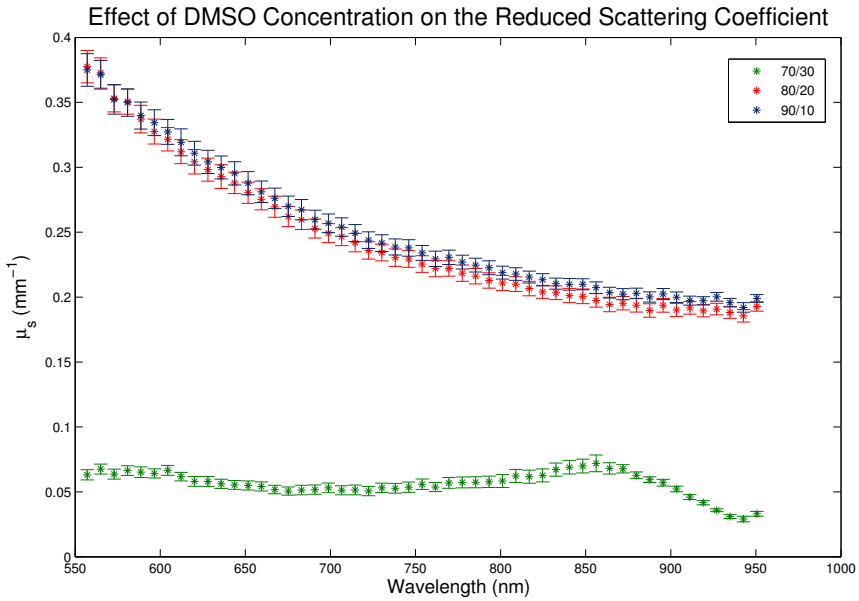

(a) Reduced scattering coefficients after one freeze-thaw cycle.

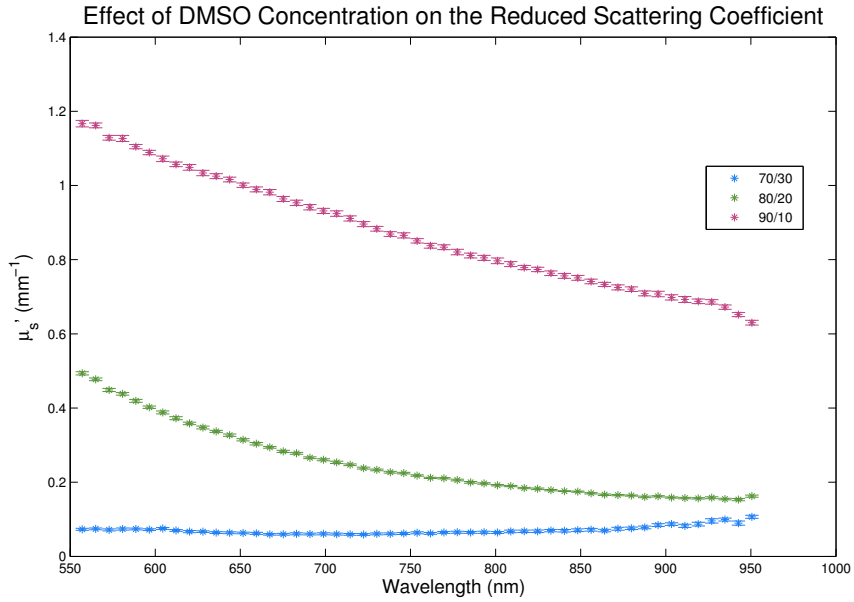

(b) Reduced scattering coefficients of after three freeze-thaw cycles.

Figure 4.6: Reduced scattering coefficients of 10% PVA-C prepared in varying concentrations of DMSO after one and three freeze-thaw cycle. The sample with the highest concentration of DMSO remains relatively flat

seemed scarcely affected by the number of freeze-thaw cycles, staying mostly flat throughout six cycles. Figure 4.7 shows the reduced scattering coefficients of the transparent gels at one, three, and six freeze-thaw cycles. Interestingly, IAD recovered reasonable absorption coefficients in the order $\mu_a \sim 10^{-3}$ mm^{-1}. As was the case with the reduced scattering coefficients, the number of freeze-thaw cycles seems to have a very minimal influence on the absorption coefficients (fig. 4.8).

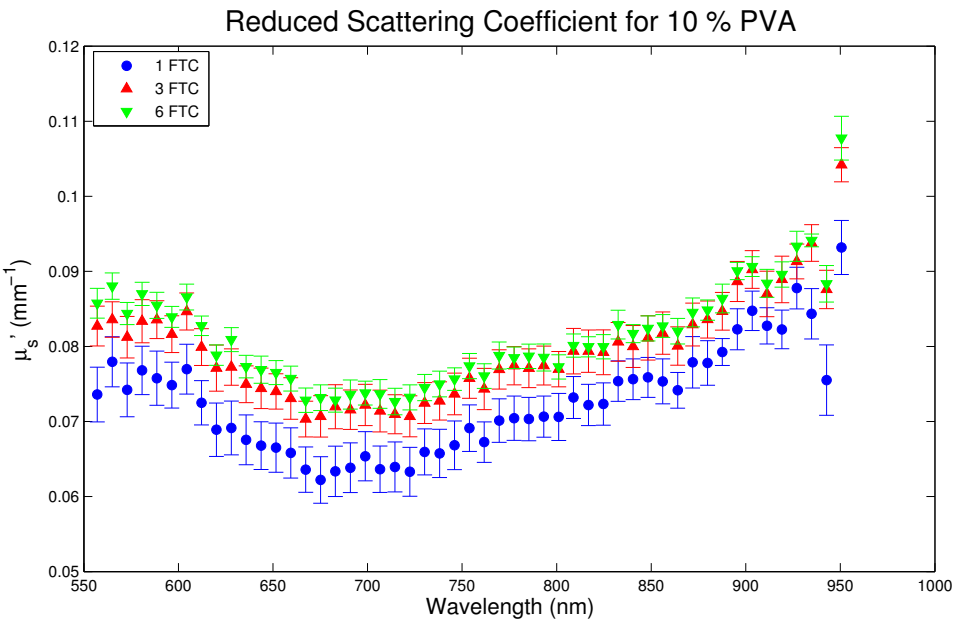

Figure 4.7: Reduced scattering coefficients for a sample of 10 wt% PVA prepared in 30 wv% DMSO at 1, 3 and 6 freeze-thaw cycles.

Table 4.2 is a summary of the effect of DMSO concentration on the reduced scattering coefficient of a 10 wt% PVA-C at different freeze thaw cycles. The table shows that for an equal number of freeze-thaw cycles, the reduced scattering coefficient diminishes with increasing DMSO concentration, but still rises with the number of cycles the sample is subjected to. The rate of increase in the reduced scattering coefficient with increasing cycles slows down as the concentration of DMSO is increased. The 10/90 slab showed a drastic increase in scattering going from one cycle to six, while the 30/70 sample saw only modest gains over the same number of cycles.

The anisotropy factors recovered for 10 wt% PVA-C with different varying DMSO concentrations are shown in table 4.3. Here, rather interesting patterns emerge. For the translucent formulations, the anisotropy factor diminishes with increasing number of freeze-thaw cycles as was observed with PVA cryogels prepared in pure water (c.f table 4.1). The transparent sample, however reverses this trend. The recovered anisotropy rises with increasing freeze-thaw cycling.

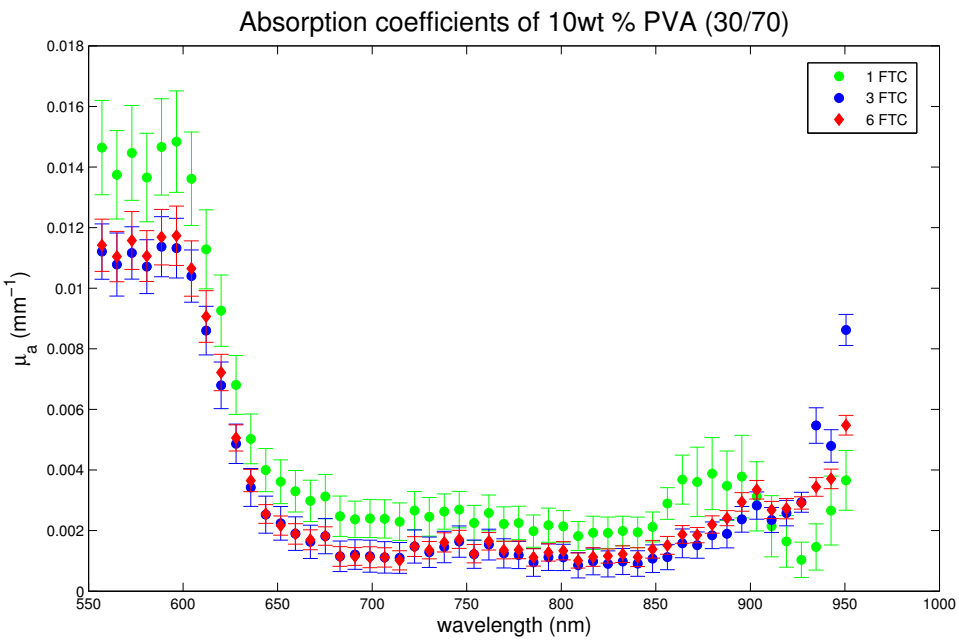

Figure 4.8: Absorption coefficients for a sample of 10 wt% PVA prepared in 30 wv% DMSO at 1, 3 and 6 freeze-thaw cycles.

	$\mu_s'(mm^{-1})$ at 750nm %[DMSO/Water]		
FTC	10/90	20/80	30/70
1	0.266 ± 0.005	0.225 ± 0.006	0.069 ± 0.003
3	0.824 ± 0.006	0.214 ± 0.002	0.075 ± 0.003
6	1.000 ± 0.020	0.594 ± 0.007	0.077 ± 0.002

Table 4.2: Effect of DMSO concentration on the Reduced Scattering Coefficient of 10 wt% PVA-C at 750nm

	g at 750nm %[DMSO/Water]		
FTC	10/90	20/80	30/70
1	0.693 ± 0.016	0.891 ± 0.006	0.402 ± 0.086
3	0.617 ± 0.006	0.779 ± 0.005	0.461 ± 0.044
6	0.540 ± 0.014	0.697 ± 0.007	0.769 ± 0.011

Table 4.3: Effect of DMSO concentration on the scattering anisotropy of 10 wt% PVA-C at 750nm

4.2.2 Stability over time

Counter (2010) looked briefly into the optical stability of PVA-C phantoms, and noted that cryogels displayed increased scattering over time even without external stimuli. Although all slabs showed increased scattering, those samples that had undergone only one freeze-thaw cycle exhibited the most drastic increase. To investigate this phenomenon, measurements of the optical properties of select gels were made on some of the NRC-IMI samples, with additional measurements performed two months after initial measurements. The samples were all stored in ziplock bags at room temperature. A bit of distilled water was added to the bag in order to curtail inhibit desiccation. All samples displayed increased scattering over time, with the effect tapering off as the number of freeze-thaw cycles increased.

FTC	Initial $\mu_s'(mm^{-1})$	Final $\mu_s'(mm^{-1})$	$\Delta\%$
1	0.69 ± 0.03	0.84 ± 0.05	22 ± 2
3	1.75 ± 0.04	1.84 ± 0.09	4.9 ± 0.3
6	2.53 ± 0.05	2.61 ± 0.04	3.38 ± 0.08

Table 4.4: Changes in Reduced Scattering Coefficient for measurements taken two months apart (10 wt% PVA).

Besides optical stability, physical integrity was also studied. In-house samples showed mold growth only a few weeks after production, while NRC-IMI samples were more resilient. The latter samples were treated with a biocide during production, and hence managed to outlast some of the in-house samples, despite being older. Of the NRC-IMI samples, those prepared under a nitrogen-purged atmosphere showed a greater propensity to desiccate, especially at the corners, despite care being taken to store them in a moist environment. For this reason, a lot of the nitrogen-purged samples were lost before being thouroughly analyzed. Only the samples with 10% PVA-C survived until experimentation. The transparent samples prepared in a dmso/water solvent showed the greatest resilience, having the least propensity to desiccate, and maintaining greater structural integrated after prolonged handling.

4.2.3 Effect of Nitrogen Atmosphere

Figure 4.9 shows a contrast in the reduced scattering coefficient for 10 wt% PVA cryogels prepared in water under normoxic and hypoxic (nitrogen) environments. The latter tended to be physically stiffer, as well as more susceptible to dessication. It was initially suspected that an increase in stiffness would be expected to correlate with a increase in scattering. However, reviewing the three samples, no definite pattern was observed. For the singly- and hexa-cycled samples, the reduced scattering coefficient for normoxic samples is actually higher than that of their hypoxic counterparts. Only in the thrice-cycled (fig.4.9b) sample were the reduced scattering coefficients of hypoxic samples greater than that of normoxic ones.

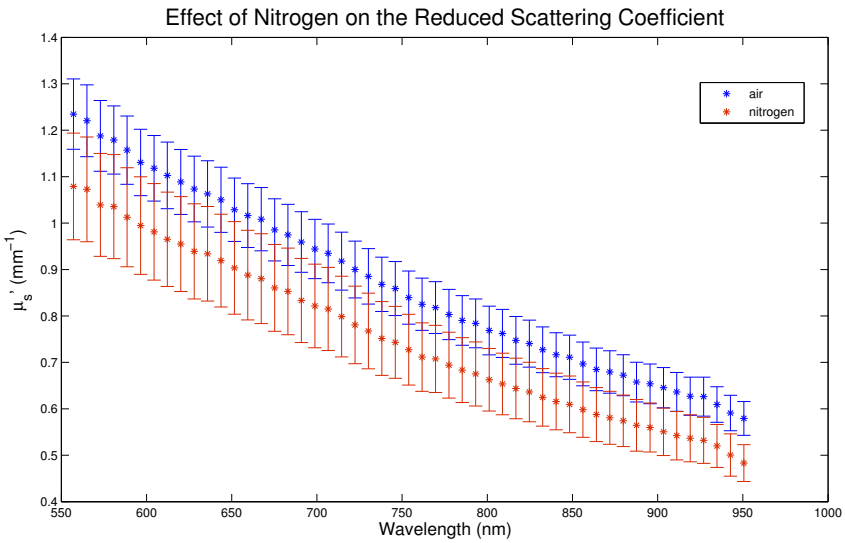

(a) Reduced scattering coefficients of cryogel sample after 1 freeze-thaw cycle.

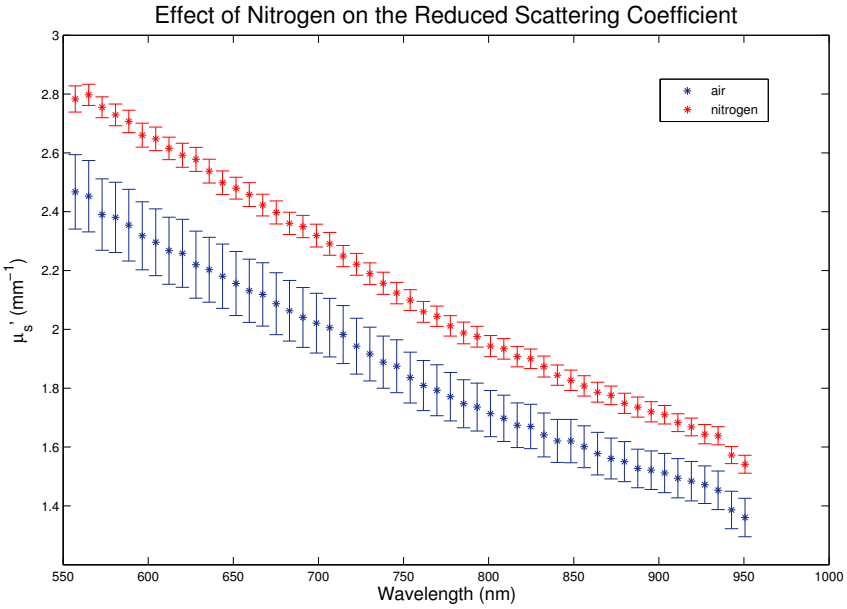

(b) Reduced scattering coefficients of cryogel sample ater 3 freeze-thaw cycles .

Figure 4.9: Reduced scattering coefficients of 10 wt% PVA-C under air and nitrogen-purged conditions compared.

4.3 Homogeneity

All samples subjected to one freeze-thaw cycle, regardless of polymer concentration had noticeable inhomogeneities, and were generally frail. The samples had regions of differing turbidity characterized by the presence of easily visible streaks of different turbidity. Subsequent cycling resulted not only in more rigid the samples, but also increased and uniform turbidity. NRC-IMI samples prepared using 5 wt% PVA were too flimsy and generally unwieldy. Most of these samples broke apart during handling. To mitigate this, 5 wt% PVA-C samples prepared in-house had their thickness more than doubled from 2mm to 5mm, after which they could be properly handled. Even in this case, the samples were still too cumbersome to work with after one freeze-thaw cycle, but quickly became tractable with subsequent cycling.

4.4 Discussion

All reviewed phantoms, whether received from NRC-IMI or prepared in-house were purely scattering PVA cryogel slabs with no added absorbers. As was the case with purely scattering Intralipid phantoms, IAD reported unrealistically high (~0.01 mm^{-1}) absorption coefficients. Due to the retrieval algorithm's inability to reproduce satisfactory data, experimental recovery of absorption coefficients was not possible. In a previous study on PVA-C (Counter, 2010), the monte carlo algorithm used had trouble recovering the very low absorption coefficients of slab phantoms. However, SRS measurements on a large PVA-C block phantom obtained from NRC-IMI showed the absorption coefficient to resemble that of water. Since the PVA-C synthesis followed in-house is directly derived from NRC-IMI protocols, it is reasonable to assume that the batch of samples examined had absorption characteristics identical to water.

Characteristic reduced scattering coefficient spectra for PVA-C at different freeze-thaw cycles are shown in figures 4.1 and 4.2. The former illustrates the unpredictable behaviour encountered in dealing with very low PVA concentrations. These samples were generally very flimsy and too cumbersome to handle. Due to their poor structural integrity, the samples tended to tear during handling. Because of the difficulties encountered in handling such samples, a specially designed appartus was machined to hold the samples in place at the sample ports. Even with this device in place, the samples would not stay taut enough to provide a flat reflecting surface. A workaround was to synthesize all 5 wt% phantoms at more than double the thickness. Thus, more tractable samples were obtained. However, the thicker samples were still very fragile after the first cycle, becoming only properly manageable after the second.

For the rest of the samples, typified by figure 4.2, behaviour expected of PVA-C after repeated cycling is observed. As the number of cycles increases, so does the reduced scattering coefficient at all wavelengths. The increase appears to be rather uniform and steady up until five cycles, at which point different behaviour manifests. The influence of freeze-thaw cycling on the reduced scattering is perhaps better illustrated

in figure 4.3, in which the reduced scattering coefficients at three selected wavelengths are sketched against the number of cycles. For all wavelengths, the increase in reduced scattering coefficient is very linear (a fit of the data suggests about 0.262 mm^{-1}/ftc at 750nm), and hits a plateau at five cycles. This behaviour was observed for the 15 wt% PVA sample (0.279 mm^{-1}/ftc at 750nm) as well. The 20 wt% PVA sample breaks the trend in that the plateau seems to set in earlier at four freeze-thaw cycles, with a linear trend of 0.282 mm^{-1}/ftc at 750nm. The plateau effect is not unexpected, as it was observed in earlier studies. Kharine et al. (2003) report a 'six to seven' cycle limit, while Devi et al. (2005) report a four cycle limit for 20 wt% PVA (99% hydrolysis). It makes intuitive sense that scattering cannot be expected to increase infinitely as the gel crystallization levels approach saturation.

The differences between these results and those discussed by Devi and Kharine are immediately obvious. For a 20 wt% (99% hydrolized) PVA cryogel, the former reports a maximum reduced scattering coefficient of 0.48 mm^{-1} at 632.8nm, and the latter 0.62 mm^{-1} at 1064nm. Since Kharine's results are not as comprehensive, and at wavelengths outside the scope of this study's measuring capabilities, attention will be paid only to Devi's. A linear regression of the reduced scattering coefficients – up to four freeze-thaw cycles – reported by Devi shows a steady increase of around 0.12mm^{-1}/ftc. Similar treatment applied to the in-house samples yielded 0.288 mm^{-1}/ftc at 632.8 nm, marginally higher from that observed at 750nm. Thus, at every point in the freeze-thaw cycle, in-house samples exhibit a higher degree of scattering. Earlier studies (Stauffer and Peppas 1991, 1992) reported that the amount of light transmitted by PVA cryogels was a function of the freezing and thawing time in addition to concentration. Devi's group employed a 12 hour freezing cycle at -20°C followed by a 12 –14 hour thaw cycle at room temperature. No information is provided about the rate of freezing and thawing, so it is assumed they were uncontrolled. Counter (2010) demonstrated that crudely controlling the thawing rate using an ice bath resulted in moderate but appreciable gains in the reduced scattering coefficient. In this study, both the freezing and thaw rates were strictly controlled over fixed periods as described in section 2.8.2. These slower rates of freezing and thawing result in gels with higher degrees of crosslinking and homogeneity as astutely observed by Counter, and may contribute to the higher overall scattering properties of in-house samples.

Another important facet in tuning the optical scattering of PVA-C was the effect of the concentration of polymer. Although Stauffer and Peppas (1992) characterized 10 wt% and 15 wt% PVA cryogels, they did not study the effects of polymer concentration on the optical properties. Intuition dictates that as the concentration of raw polymer increases, the number of available crystallization sites would increase, therefore resulting in an overall increase in scattering. From figure 4.4, it is observed that for equal freeze-thaw cycles, the reduced scattering coefficient increases with polymer concentration, with the highest concentration (20%) being a glaring exception. Samples obtained from the NRC-IMI exhibit an even weirder trend, with the reduction in scattering first observed at 15 wt% polymer concentration, and falls further for the highest

concentration. The net result for both sets of samples is that 20 wt% slabs have *lower* scattering coefficients than those with 10 wt% PVA. Because of the conflicts between JCC and NRC-IMI data, it is not possible to form a coherent picture of what exactly is the relationship between polymer concentration and scattering. The samples with higher polymer concentration certainly exhibit superior structural integrity, thus it would be expected that their increased rigidity would be concomitant with a higher degree of scattering. The *decrease* in optical scattering is certainly most puzzling, as at best a plateauing effect might have made more sense, attributable to a saturation in the number of scattering sites.

Crude attempts at measuring the anisotropy coefficient using unscattered transmitted light were also made. These attempts proved fairly successful during lipid characterization studies, and are here compared with values obtained by (Devi et al. 2005). Unlike the very high and scattering-independent values reported in literature, the anisotropy coefficients obtained consistently decreased with increasing scattering for all PVA concentrations. At first it was suspected that in order to converge to a meaningful solution, IAD might have been compensating for the increased scattering by chipping away at the anisotropy coefficients. However, setting the anisotropy coefficient in IAD to 0.90 showed only a small discrepancy (1.5% at 750nm) between the scattering coefficients calculated in tandem with anisotropy and those calculated at fixed anisotropies. Also, the fact that similar reductions in anisotropy were observed with Magic Light exonerated IAD of suspicions of slipshod calculations. At this juncture, without independent anisotropy measurements - e.g. goniometric - it is impossible to verify the reduction in anisotropy factors observed with increasing scattering as reported by both integrating sphere retrieval algorithms.

Samples received from the NRC-IMI were measured with the same double integrating sphere setup, and displayed trends similar to those observed for in-house samples, with the difference being their much higher reduced scattering coefficients. Looking back at table 4.4, and at Counter(2010)'s data, an increase in scattering in NRC-IMI samples is observed with the samples left unperturbed. This increase is less pronounced at higher freeze-thaw cycles. By the time comprehensive measurements were made on both sets of samples, the in-house samples were relatively fresh while the NRC-IMI samples were almost one year old. Thus, for comparable 10 wt% PVA-C slabs, the differences in the reduced scattering coefficients at 750 nm were as large as 136% after one freeze-thaw cycle, and 70% after six cycles. By comparison, 15 wt% PVA samples sat at 123% and 21% for similar cycles. Two observations are worth noting: (a) PVA-C scattering spontaneously increases with age, and (b) increasing the polymer concentrations and/or number of freeze-thaw cycles moderately retards this effect. Analysis of the 20 wt% PVA-C, however, once agains shatters this convenient trend. For these batches of samples, peculiar trends are observed. After the first freeze-thaw cycle, the NRC-IMI sample exhibits 18% higher scattering than its in-house counterpart. However, after six cycles the trends are reversed, with the in-house samples showing a 14% scattering coefficient at 750nm. Once again it is not clear why

the 20 wt% PVA cryogel behaves this way. What is apparent, though, is that the 20 wt% PVA-C from NRC-IMI is the most impervious to the effects of ageing observed in other samples. This perceived stability may be due to the difference in gelation of PVA at different concentrations. Stauffer and Peppas (1991) mentioned crystallization as one of the mechanisms responsible for the gelation of hydrogels. A higher polymer concentration translates into a greater number of interaction sites, i.e. crystallization sites per given volume, which would in turn allow the most rapid gelation. For this reason, compared with lower polymer concentration samples, 20 wt% PVA samples display the best homogeneity and structural integrity after the least number of cycles, but soon reach a saturation point. This theory may explain why these samples plateau sooner than the rest, and why they're relatively sturdier than the rest, but doesn't adequately explain why the reduced scattering coefficients were observed to be lower than those of lower concentration samples.

A cursory investigation into the effects of a nitrogen-purged atmosphere on the reduced scattering coefficients was also conducted. Unpublished measurements by Dr. Campbell suggested that for every number of freeze-thaw cycles, PVA-C prepared under a nitrogen atmosphere should have higher scattering coefficients than those prepared in air. Unfortunately most of the samples prepared under hypoxic conditions were lost to desiccation, and only one lot remained semi-intact. The analysis of that batch yielded inconclusive results with no discernible trend. Although all samples were stored in sealed plastic bags with water, continued handling and exposure during preliminary investigations eventually ruined the nitrogen-purged samples. The rest of the samples from NRC-IMI were amazingly very stable, even after a period of nearly one year of storage and intermittent handling. These samples were doped with biocide to prevent mold growth while in-house samples were not so equipped. Although considerably older, they outlasted the in-house samples, which soon grew moldy after a few weeks. The shelf-life of PVA-C was not determined, but judging from the structural stability of the NRC-IMI samples, it would not be unreasonable to assume a life time of a least a few years with proper handling and storage. The only real problem with such cryogels is their optical instability: scattering increases over time. It is still not clear if this effect is due to auto-crystallization, where an increased number of crystallites form without freezing and thawing, or whether the density of scattering centres increases as a result of desiccation. It has been proposed that because this phenomenon is observed in lower cycled cryogels, such gels might still have a greater proportion of the water phase and are therefore more sensitive to changes as a result of water loss (Counter 2010).

To evaluate the efficacy of PVA-C as an optical phantom, reference must be made to the list of ideal phantom characteristics previously discussed in section 1.1. As seen, PVA-C can be tuned without the addition of extrinsic scattering agents to produce a wide range of scattering properties via a number of means including freeze-thaw cycle, DMSO-doping, and adjustment of polymer concentration. The samples studied produced reduced scattering coefficients encompassing a variety of human

tissue samples, from the very high scattering of diseased breast tissue ($\mu_s' = 2.62\text{mm}^{-1}$) reported by Devi et al. (2005) to the very low reduced scattering coefficient of white brain matter ($\mu_s' = 0.204\text{mm}^{-1}$) reported by Cheong et al. (1990). This variety of tuning methods affords a researcher the flexibility to experiment with different sets of combinations to achieve desired levels of optical scattering. The absorption properties of pristine PVA-C are similar to water, but can be easily changed by the addition of extrinsic absorbers. As PVA-C phantoms are biocompatible, biological absorbers such as whole blood may also be added to hydrogel mixtures to mimic real tissue. The downside to such absorbers, though, is the degradation of the shelf life of a phantom. With proper care and handling, PVA cryogels have potentially long shelf-life. Properly stored gels retained their structural integrity over a long period, however they proved to be optically unstable. This effect is most pronounced for low-cycle samples and may be mitigated through the use of higher polymer concentrations and higher freeze-thaw cycles at the outset. To counteract the increase in scattering concomitant with higher cycling, samples may be doped with varying concentrations of DMSO. Although not confirmed within the scope of this study, the refractive index of PVA-C has been found to be similar to that of water and most soft tissues (Devi et al. 2005). The incorporation of regions with different optical properties, e.g. to simulate tumours, may be a tricky feat to accomplish. Potentially, regions of meant to mimic tumours could be cycled separately, producing cryogels, and then reincorporated into a larger hydrogel mixture and re-cycled as one phantom. The result would then be a new phantom with varied scattering along different regions. Achieving the opposite, i.e. embedding regions of lower scattering inside a higher scattering matrix could perhaps be achieved via different combinations of doping the lower scattering with scattering suppressants such as DMSO, or experimenting with different concentrations of polymer. However, there is always the potential for undesired leaching of material from one medium to the other, e.g. via diffusion should there be a concentration differential. Construction of complex phantom geometries require specialized tools such as an environmental chamber. However, slabs of PVA-C like the ones studied herein are very easy to construct even with the most basic of tools in any adequately equipped laboratory; and the production protocols can be easily followed by an operator with minimal chemistry training. PVA is non-toxic, thus making it user-friendly, and commercially available PVA is relatively inexpensive ($218/kg).

Conclusions and Future Work

This thesis described the fabrication of polyviny alcohol cryogel phantoms and the characterization of their optical properties using a double integrating sphere system. The work is part of a drive to establish the integrating sphere system as a viable, cost-effective method for characterizing thin slab optical samples at the Juravinski Cancer Centre, and was undertaken to built upon the foundations laid by Counter (2010), to address the shortcomings encountered, and to improve upon in that seminal study.

5.1 Addressing Previous Short-comings

In order to construct a more permanent setup, substantial investment was made into obtaining commercial grade integrating spheres. These spheres were larger and coated with a highly reflective inner surface. Their larger sample ports were meant to address the issue of lateral light losses identified in earlier double integrating sphere studies (Zhu et al. 2007), while the highly reflective surface was to provide more uniform, better quality reflectances. The spheres, however were not as stellar performers as had been anticipated. First, the sample port is surrounded by a massive black ring 8mm tall. It is presumed that most, if not all the light hitting this surface is absorbed. However, there was no viable method to satisfactorily account for these losses: incorporating these black rings' surface areas into the sample ports' would unrealistically inflate parasite port fractions. The absence of a port reducer on the entrance port to the reflectance sphere meant a lot of light was being lost. At least these losses, unlike the former, could be accounted for in IAD. Another pitfall was the unconventional sphere wall reflectance spectrum (compared to manufacturer-reported values), not to mention less than impressive wall reflectance. The odd profile's potentially negative effects were mitigated by matching measured reflectance and transmittance values to specific sphere wall reflectances in IAD, however, no adequate explanation was found for the spheres' poor reflectance. For future work, it would be worth looking into acquiring alternative light source and detector systems to replace the rather complex CCD detector array used for this study. A further improvement to Counter's setup was the use of two integrating spheres for the simultaneous measurement of reflectance and transmittance in place of a single channel spectrometer setup. Although not fully

exploited to its potential, this improvement will become crucial in the near future should measurement of samples with dynamic properties be called for. The setup was also designed to flexibly move around in order to accommodate different sample sizes and measuring conditions (e.g. sliding the transmittance sphere out of place on a railing system instead of having to dismantle it in order to make unscattered transmitted measurements), while computerized acquisition was updated to a more user-friendly Windows XP-based GUI system. To standardize and refine cryogel fabrication, greater collaboration with the NRC-IMI was put into place. An environmental chamber was acquired, and NRC-IMI standard operating protocols were followed whenever possible in order to fine-tune sample preparation. This improved cooperation allowed for better control of freeze-thaw cycling and temperature control.

5.2 Summary of Findings

The integrating sphere system was used to characterize thin PVA-C cryogel slabs. Scattering anisotropies and reduced scattering coefficients were recovered for gels subjected to repeated freeze-thaw cycles. Attempts at recovering absorption coefficients were fruitless at this time. To test the efficacy of the system, efforts were made at recovering the optical properties of known concentrations of lipid phantoms. The integrating sphere setup was used in conjunction with the well established Inverse Adding Doubling algorithm cross-checked with the Magic Light inverse Monte-Carlo *cum* small-angle approximation technique. IAD was chosen for its simplicity and speed. It combines the Adding Doubling algorithm with Double Integrating Sphere theory, iteratively executing them to deduce optical properties that minimize the difference between measured and expected values. It also includes Moffat's corrections to account for integrating sphere effects. The integrating sphere system-IAD combo was found to underestimate the reduced scattering coefficients of purely scattering Intralipid, with the degree of discrepancy growing as the lipid concentration increased (ranging from 6.9% for Intralipid-1% to 17.5% for Intralipid-5%). Measurements made on absorbing ink and dye phantoms exposed the setup's inability to recover absorption coefficients. Systematic overestimations of the absorption coefficients by a whole order of magnitude were observed for the lowest absorbing dye phantoms. The degree of overestimation diminished as the amount of absorption increased, but nonetheless stayed above 60% for all ink and dye samples. Such differences were deemed too egregious, and recovery of the absorption coefficients was abandoned. Despite the sample thicknesses (1.9mm), attempts were made at recovering the scattering anisotropy. Surprisingly, calculated anisotropy factors were well within those reported in previously reported studies (Michels et al. 2008; Van Staveren et al. 1991) over a wide range of wavelengths above 700nm.

For all concentrations of PVA-C, the reduced scattering coefficient was observed to increase linearly with the number of freeze-thaw cycles, reaching a plateau after which only moderate gains in scattering were observed. Save for the 5 wt% PVA samples,

scattering trends were all regular. Samples prepared with this low concentration of PVA were generally cumbersome to handle, and displayed ill-defined trends. The scattering anisotropy was confirmed to decrease with increasing number of freeze-thaw cycles for *all* PVA concentrations. An examination into the relationship between polymer concentration and optical properties revealed the reduced scattering coefficient to increase with concentration at each cycle. The samples with the highest PVA concentration were an anomaly, displaying scattering coefficients lower than all concentrations save for the 5 wt% PVA samples. For each freeze-thaw cycle, the scattering anisotropy was observed to decrease with increasing polymer concentration. Again the 20 wt% PVA samples broke this trend, displaying scattering anisotropies that sat between those of the 10 wt% and 15 wt% PVA samples.

Samples prepared in a dmso-water mixture displayed interesting results. Increases in the concentration of dmso resulted in a diminution of the reduced scattering coefficient for all freeze-thaw cycles. Scattering anisotropy trends were not as clear-cut, with translucent samples prepared in 10% dmso showing a decrease in anisotropy with successive cycling, and the transparent samples exhibiting the opposite. Other PVA-C concentrations displayed trends in which the anisotropy would either decrease or increase after the third cycle only to go in the opposite direction after the sixth. As such, the data relating the anisotropy coefficients to polymer concentration at varying dmso levels are to be treated as inconclusive. Studies involving the fabrication of PVA-C formulations under a nitrogen environment were not extensive enough to extract any meaningful trends at this juncture.

5.3 Future Studies

Because the Monte Carlo algorithm used by (Counter 2010) was not well documented, it was abandoned for the well-established IAD method. While IAD has proved to be fairly capable at retrieving reduced scattering and anisotropy coefficients, its dismal performance at calculating absorption was a bit disquieting. Magic Light did not fare any better given the same sets of measurements. Though significantly faster than pure Monte Carlo methods, it is still *much* slower than IAD and a lot more cumbersome to work with for large numbers of files. Future work on optical property recovery – if it is to be satisfactorily comprehensive – will have to begin with finding a viable recovery algorithm for the double integrating sphere set up, either through somehow revamping the old JCC Monte Carlo code, or seeking alternative recovery algorithms like the one prosed by Cruzado et al. (2013).

It would also be opportune to manufacture sets of solid phantoms with known optical properties for use in periodic calibrations. While the liquid phantoms sufficed, there can be unwieldy, and restrict the flexibility of the setup.

5.3.1 Further work with PVA

PVA-C holds massive potential as a future optical phantom material. The use of purely physical means to control optical scattering avoids the infusion of extraneous, potentially hazardous chemical scatters, further improving the phantoms' biocompatibility. In the near future, more work will be done to control the optical properties of slab phantoms with more finesse. A detailed, deliberate study into the relationship between freezing and thawing rates and the scattering coefficient is yet to be conducted. It has already been observed that slower, more methodical ramping of the freeze-thaw cycles produced phantoms with higher degrees of scattering for the same number of cycles. This relationship needs to be properly quantified and exploited.

Of all the formulations examined, the transparent slabs hold the most promise for their potential versatility. Because of their very low intrinsic scattering, these samples could potentially be doped with extrinsic scatterers - should the need arise - to achieve even greater control over scattering that physical cycling cannot attain. It would be worth investigating how optically stable these phantoms remain over time compared to other PVA formulations. There are plans to incorporate a variety of absorbers, including whole blood or a hemoglobin-like synthetic dye to accurately reproduce tissue absorption, and to examine the response of said absorbers to repeated freeze-thaw cycling. Experiments to add radiosensitive chromophores into clear PVA-C are already being undertaken at the JCC. Supplementary to these studies, incorporation of hydrophilic and/or hydrophobic photosensitizers into clear gels will present an opportunity to study the photochemistry of said samples. Steady-state or time resolved fluorescence measurements of these gels using interstitial isotropic source and detection fibres may also be taken in the distant future. Also in the future, it would behoove the researcher to look into Pd/Pt-porphyrin oxygen detection studies.

These steps are designed to lead to a gradual, better understanding of the practical considerations of using PVA cryogel phantoms. At present, only thin slab phantoms have been investigated. However, novel mould shapes designed to resemble specific tissue morphologies will be obtained. These moulds already exist and can be loaned from the NRC-IMI, where research into the mechanical properties of PVA-C is currently underway. Continued collaboration between the JCC and NRC-IMI will open new avenues into the research of cryogels.

Bibliography

Bray, James C. and Edward W. Merrill (1973). "Poly(vinyl alcohol) hydrogels. Formation by electron beam irradiation of aqueous solutions and subsequent crystallization". In: *Journal of Applied Polymer Science* 17.12, pp. 3779–3794. ISSN: 1097-4628. DOI: 10.1002/app.1973.070171219.

Chatigny, Stéphane et al. (1999). "Hybrid Monte Carlo for photon transport through optically thick scattering media". In: *Applied optics* 38.28, pp. 6075–6086.

Cheong, Wai-Fung, Scott A Prahl, and Ashley J Welch (1990). "A review of the optical properties of biological tissues". In: *Quantum Electronics, IEEE Journal of* 26.12, pp. 2166–2185.

Counter, G. M. (2010). "Optical Characterization of Poly(vinyl alcohol) Cryogels". MSc Thesis. Hamilton, Ontario, Canada: McMaster University.

Cruzado, Beatriz Morales, Sergio Vázquez y Montiel, and José Alberto Delgado Atencio (2013). "Genetic algorithms and MCML program for recovery of optical properties of homogeneous turbid media". In: *Biomed. Opt. Express* 4.3, pp. 433–446.

Darwis, Darmawan et al. (2002). "Characterization of poly (vinyl alcohol) hydrogel for prosthetic intervertebral disc nucleus". In: *Radiation Physics and Chemistry* 63.3, pp. 539–542.

de Vries, G. et al. (1999). "The effect of light losses in double integrating spheres on optical properties estimation". In: *Selected Topics in Quantum Electronics, IEEE Journal of* 5.4, pp. 944–947. ISSN: 1077-260X. DOI: 10.1109/2944.796315.

Devi, C Usha, RM Vasu, and AK Sood (2005). "Design, fabrication, and characterization of a tissue-equivalent phantom for optical elastography". In: *Journal of biomedical optics* 10.4, pp. 044020–044020.

Farrell, Thomas J, Michael S Patterson, and Brian Wilson (1992). "A diffusion theory model of spatially resolved, steady-state diffuse reflectance for the noninvasive

determination of tissue optical properties invivo". In: *Medical physics* 19.4, pp. 879–888.

Firbank, Michael (1994). "The design, calibration and usage of a solid scattering and absorbing phantom for near infra red spectroscopy". PhD thesis. University College London.

Flock, Stephen T., Brian C. Wilson, and Michael S. Patterson (1988). "Hybrid Monte Carlo - Diffusion Theory Modelling Of Light Distributions In Tissue." In: *Proc. SPIE* 908, pp. 20–28. DOI: 10.1117/12.945337.

Flock, Stephen T et al. (1992). "Optical properties of Intralipid: a phantom medium for light propagation studies". In: *Lasers in Surgery and Medicine* 12.5, pp. 510–519.

Gebhart, SC, WC Lin, and A Mahadevan-Jansen (2006). "In vitro determination of normal and neoplastic human brain tissue optical properties using inverse adding-doubling". In: *Physics in medicine and biology* 51.8, pp. 2011–2027.

Glennie, D. (2009). "Use of Integrating Spheres for Improved Skin PDT Treament". MSc Thesis. Hamilton, Ontario, Canada: McMaster University.

Goebel, David G. (1967). "Generalized Integrating-Sphere Theory". In: *Appl. Opt.* 6.1, pp. 125–128. DOI: 10.1364/AO.6.000125.

Hallensleben, Manfred L. (2000). "Polyvinyl Compounds, Others". In: *Ullmann's Encyclopedia of Industrial Chemistry*. Wiley-VCH Verlag GmbH & Co. KGaA. Chap. 1. ISBN: 9783527306732.

Hassan, Christie M and Nikolaos A Peppas (2000). "Structure and applications of poly (vinyl alcohol) hydrogels produced by conventional crosslinking or by freezing/thawing methods". In: *Biopolymers · PVA Hydrogels, Anionic Polymerisation Nanocomposites*. Springer, pp. 37–65.

Hollis, Veronica S. (2002). "Non-Invasive Monitoring of Brain Tissue Temperature by Near-Infrared Spectroscopy". PhD thesis. University College London.

Hyde, Derek E et al. (2001). "A diffusion theory model of spatially resolved fluorescence from depth-dependent fluorophore concentrations". In: *Physics in medicine and biology* 46.2, p. 369.

Hyon, S-H, W-I Cha, and Y Ikada (1989). "Preparation of transparent poly (vinyl alcohol) hydrogel". In: *Polymer Bulletin* 22.2, pp. 119–122.

Jacques, Steven L (2013). "Optical properties of biological tissues: a review". In: *Physics in Medicine and Biology* 58.11, R37–R61.

Kharine, Alexei et al. (2003). "Poly (vinyl alcohol) gels for use as tissue phantoms in photoacoustic mammography". In: *Physics in medicine and biology* 48.3, pp. 357–370.

Kita, Mihori et al. (1990). "Evaluation of polyvinyl alcohol hydrogel as a soft contact lens material". In: *Graefe's archive for clinical and experimental ophthalmology* 228.6, pp. 533–537.

Kou, Linhong, Daniel Labrie, and Petr Chylek (1993). "Refractive indices of water and ice in the 0.65- to 2.5-μm spectral range". In: *Appl. Opt.* 32.19, pp. 3531–3540. DOI: 10.1364/AO.32.003531.

Labsphere (1999). *Integrating Sphere Theory and Applications*. 1. Labsphere. North Sutton, NH 03260, USA: Labsphere. URL: http://www.labsphere.com/uploads/technical-guides/a-guide-to-integrating-sphere-theory-and-applications.pdf.

Linford, J. et al. (1986). "Development of a tissue-equivalent phantom for diaphanography". In: *Medical Physics* 13.6, pp. 869–875.

Madsen, S J, M S Patterson, and B C Wilson (1992). "The use of India ink as an optical absorber in tissue-simulating phantoms". In: *Physics in Medicine and Biology* 37.4, pp. 985–993.

Metropolis, Nicholas (1987). "The beginning of the Monte Carlo method". In: *Los Alamos Science* 15.584, pp. 125–130.

Michels, Rene, Florian Foschum, and Alwin Kienle (2008). "Optical properties of fat emulsions". In: *Opt. Express* 16.8, pp. 5907–5925. DOI: 10.1364/OE.16.005907.

Morales Cruzado, B. et al. (2011, poster). "Validation of GA-MCML algorithm against IAD program". In: *International Commission for Optics 22 General Congress*.

Moscu, Diana F (2009). "Quantifying Chromophore Concentration in Tissue Simulating Phantoms Using an Optical Detection System Based on an Integrating Sphere". PhD thesis. Hamilton, Ontario, Canada: McMaster University.

Mourant, Judith R et al. (1998). "Mechanisms of light scattering from biological cells relevant to noninvasive optical-tissue diagnostics". In: *Applied Optics* 37.16, pp. 3586–3593.

Pickering, John W. et al. (1992). "Two integrating spheres with an intervening scattering sample". In: *J. Opt. Soc. Am. A* 9.4, pp. 621–631. DOI: 10.1364/JOSAA.9.000621.

Pickering, John W et al. (1993). "Double-integrating-sphere system for measuring the optical properties of tissue". In: *Applied optics* 32.4, pp. 399–410.

Plass, Gilbert N, George W Kattawar, and Frances E Catchings (1973). "Matrix operator theory of radiative transfer. 1: Rayleigh scattering". In: *Applied Optics* 12.2, pp. 314–329.

Pogue, Brian W. and Michael S. Patterson (2006). "Review of tissue simulating phantoms for optical spectroscopy, imaging and dosimetry". In: *Journal of Biomedical Optics* 11.4, pp. 041102–041102–16.

Prahl, S.A. (1988). "Light Transport In Tissue". PhD thesis. Austin, Texas, USA: University of Texas at Austin.

— (1995). "The Adding-Doubling Method". In: *Optical-Thermal Response of Laser-Irradiated Tissue*. Ed. by A.J. Welch and van Gemert M.J.C. Plenum Press, New York. Chap. 5, pp. 101–129.

— (2011). *Everything I think you should know about Inverse Adding-Doubling*. Oregon Medical Laser Center. 9205 S.W. Barnes Road, Portland, OR 97225.

Prahl, SA et al. (1989). "A Monte Carlo model of light propagation in tissue". In: *Dosimetry of laser radiation in medicine and biology* 5, pp. 102–111.

Prahl, Scott A., Martin J. C. van Gemert, and Ashley J. Welch (1993). "Determining the optical properties of turbid mediaby using the adding–doubling method". In: *Appl. Opt.* 32.4, pp. 559–568.

Royston, David D, Regan S Poston, and Scott A Prahl (1996). "Optical properties of scattering and absorbing materials used in the development of optical phantoms at 1064 nm". In: *Journal of biomedical optics* 1.1, pp. 110–116.

Stauffer, Shauna R and Nikolaos A Peppas (1991). "Reinforced uncrosslinked poly (vinyl alcohol) gels produced by cyclic freezing-thawing processes: a short review". In: *Journal of Controlled Release* 16.3, pp. 305–310.

— (1992). "Poly (vinyl alcohol) hydrogels prepared by freezing-thawing cyclic processing". In: *Polymer* 33.18, pp. 3932–3936.

Surry, K J M et al. (2004). "Poly(vinyl alcohol) cryogel phantoms for use in ultrasound and MR imaging". In: *Physics in Medicine and Biology* 49.24, pp. 5529–5546.

Tuchin, Valerii V (1997). "Light scattering study of tissues". In: *Physics-Uspekhi* 40.5, pp. 495–515.

Van Staveren, Hugo J et al. (1991). "Light scattering in Intralipid-10% in the wavelength range of 400-1100 nm". In: *Appl. Opt* 30.31, pp. 4507–4514.

Wang, Lihong and Steven L Jacques (1993). "Hybrid model of Monte Carlo simulation and diffusion theory for light reflectance by turbid media". In: *JOSA A* 10.8, pp. 1746–1752.

Wang, Lihong, Steven L. Jacques, and Liqiong Zheng (1995). "MCML—Monte Carlo modeling of light transport in multi-layered tissues". In: *Computer Methods and Programs in Biomedicine* 47.2, pp. 131 –146. ISSN: 0169-2607.

Weissleder, R. et al. (2010). *Molecular Imaging: Principles and Practice*. Molecular Imaging: Principles and Practice. People's Medical Publishing House. ISBN: 9781607950059.

Welch, Ashley J. and Martin JC Van Gemert, eds. (2011). *Optical-Thermal Response of Laser-Irradiated Tissue*. 2nd Edition. Springer Science+Business Media B.V. 2011.

Wilson, B. C., M. S. Patterson, and S. T. Flock (1987). "Indirect versus Direct Techniques for the measurement of the optical properties of tissues". In: *Photochemistry and Photobiology* 46.5, pp. 601–608. ISSN: 1751-1097. DOI: 10.1111/j.1751-1097.1987.tb04820.x.

Wilson, BC and G Adam (1983). "A Monte Carlo model for the absorption and flux distributions of light in tissue". In: *Medical Physics* 10.6, pp. 824–830.

Yaroslavsky, I. V. et al. (1996). "Inverse hybrid technique for determining the optical properties of turbid media from integrating-sphere measurements". In: *Appl. Opt.* 35.34, pp. 6797–6809. DOI: 10.1364/AO.35.006797.

Yokoyama, F et al. (1986). "Morphology and structure of highly elastic poly (vinyl alcohol) hydrogel prepared by repeated freezing-and-melting". In: *Colloid and Polymer Science* 264.7, pp. 595–601.

Zee, Peter Van der (1992). "Measurement and Modelling of the Optical Properties of Human Tissue in the Near Infrared". PhD thesis. University College London.

Zhu, Dan et al. (2007). "Effect of light losses of sample between two integrating spheres on optical properties estimation." In: *Journal of biomedical optics* 12.6, pp. 0640041–060048. ISSN: 1083-3668. DOI: 10.1117/1.2815691.